STEADY-STATE AND CYCLO-STATIONARY RTS NOISE IN MOSFETS

Samenstelling promotiecommissie:

Voorzitter:	prof.dr.ir. A.J. Mouthaan	
Secretaris:	prof.dr.ir. A.J. Mouthaan	Univ. Twente, EWI
Promotor:	prof.dr. H. Wallinga	Univ. Twente, EWI
Ass. Promotor:	dr.ir. C. Salm	Univ. Twente, EWI
Referent:	dr. R. Woltjer	Philips Research Eindhoven
Leden:	prof.dr. J. Schmitz	Univ. Twente, EWI
	prof.dr.ir. B. Nauta	Univ. Twente, EWI
	prof.dr. G. Bosman	Univ. of Florida
	dr.ir. L.K.J. Vandamme	TU Eindhoven

STEADY-STATE AND CYCLO-STATIONARY RTS NOISE IN MOSFETS
by
J.S. Kolhatkar
Proefschrift: University of Twente, Enschede, The Netherlands. 2005.
ISBN: 90-365-2127-0

©J.S. Kolhatkar 2005. All rights reserved.
Reproduction in whole or in part is prohibited
without the written consent of the copyright owner.
Printing: Print Partners Ipskamp, Enschede, The Netherlands.

This research has been funded by STW (Dutch Technology Foundation).

STEADY-STATE AND CYCLO-STATIONARY RTS NOISE IN MOSFETS

PROEFSCHRIFT

ter verkrijging van
de graad van doctor aan de Universiteit Twente,
op gezag van de rector magnificus,
prof. dr. W.H.M. Zijm,
volgens besluit van het College voor Promoties
in het openbaar te verdedigen
op donderdag 27 januari 2005 om 15.00 uur

door

Jay Sudhir Kolhatkar

geboren op 6 november 1973
te Jamshedpur, India

Dit proefschrift is goedgekeurd door:
de promotor: prof.dr.ir. H. Wallinga
de assistent promotor: dr.ir. C. Salm

Contents

Summary v

Samenvatting vii

List of Figures ix

1 Introduction 1
- 1.1 Noise in Semiconductors . . . 1
  - 1.1.1 Shot Noise . . . 2
  - 1.1.2 Thermal Noise . . . 2
  - 1.1.3 Flicker or $1/f$ Noise . . . 2
  - 1.1.4 Generation Recombination Noise (RTS Noise) . . . 3
  - 1.1.5 Other Noise Sources . . . 3
- 1.2 MOSFET $1/f$ Noise Models . . . 4
  - 1.2.1 ΔN . . . 4
  - 1.2.2 $\Delta\mu$ . . . 5
  - 1.2.3 Unified (ΔN and $\Delta\mu$) . . . 6
- 1.3 Low-Frequency Noise Reduction . . . 6
  - 1.3.1 Cycling from Inversion to Accumulation . . . 7
  - 1.3.2 Periodic Large-Signal Excitation . . . 8
- 1.4 Scope . . . 9
- 1.5 Outline . . . 9

2 Low-Frequency Noise - Spectral Analysis 13
- 2.1 LF noise PSD . . . 14
- 2.2 LF noise measurements . . . 16
  - 2.2.1 Measurement Setup . . . 16
  - 2.2.2 Measurement Conditions . . . 17
- 2.3 Measurement Results . . . 18
- 2.4 Discussion . . . 23
- 2.5 Conclusions . . . 25

3 RTS - Time Domain Analysis 27
3.1 Statistical Analysis . . . 28
3.1.1 Random Processes . . . 28
3.1.2 Probability Distribution of RTS . . . 32
3.1.3 Power Spectral Density (PSD) of RTS . . . 33
3.1.4 Cyclo-stationary RTS . . . 36
3.2 RTS Measurements in Time Domain . . . 39
3.2.1 Experimental Details . . . 39
3.2.2 RTS Parameter Extraction . . . 40
3.2.3 Separation of RTS and Background noise . . . 40
3.3 RTS measurement results . . . 42
3.3.1 RTS in Steady-state . . . 44
3.3.2 Separating RTS and 1/f . . . 44
3.3.3 RTS under Large-signal Excitation . . . 45
3.4 Discussions . . . 47
3.5 Conclusions . . . 49

4 Modeling of Random Telegraph Signals 51
4.1 Traps and origin of RTS . . . 53
4.2 RTS in steady-state . . . 55
4.2.1 S-R-H statistics . . . 55
4.2.2 Effect of V_{GS} on $\overline{\tau_c}$ . . . 57
4.2.3 Effect of V_{GS} on $\overline{\tau_e}$ . . . 59
4.2.4 Capture Cross Section (σ) . . . 61
4.2.5 Occupancy . . . 62
4.2.6 RTS Amplitude . . . 62
4.2.7 Model Results (steady-state) . . . 63
4.3 RTS under Transient Biasing . . . 65
4.3.1 Measuring Trap-Occupancy under Transient biasing . . . 67
4.4 RTS Under Periodic Large-Signal Excitation . . . 70
4.4.1 Model Results (Periodic Large-Signal Excitation) . . . 71
4.5 RTS Noise PSD . . . 75
4.6 Discussions . . . 77
4.7 Conclusion . . . 78

5 Hot-Carrier Degradation and LF Noise in MOSFETs 79
5.1 Experimental . . . 80
5.1.1 LF Noise measurements . . . 80
5.1.2 Hot Carrier Stressing . . . 81
5.2 Results . . . 82
5.3 Discussion . . . 85
5.4 Conclusion . . . 86

6 Conclusions 87

Abbreviations **89**

List of symbols **91**

Bibliography **93**

Acknowledgments **101**

Summary

The study of low-frequency noise in MOSFETs is gaining importance with reducing device dimensions. The effect of low-frequency noise is not just confined at low frequencies but it is also up-converted to Radio Frequencies (RF) in electronic circuits like oscillators and mixers. Hence the modeling of this low-frequency noise and techniques to reduce its effect are important. It has been reported in literature that the low-frequency noise in MOSFETs decreases significantly under changing gate bias. Unfortunately, the circuit simulators available do not model this behavior. In this thesis the low-frequency noise in MOSFETs under steady-state and dynamic biasing conditions was investigated. The low-frequency noise in MOSFETs dominated by RTS noise is the most sensitive to biasing changes. While periodic large-signal excitation is successfully used to reduce the LF noise dominated by RTS, it also occurs in some samples that the low-frequency noise increases because the normally 'dormant' traps under steady-state conditions get 'active' as a result of the dynamic biasing. The RTS noise is the dominant noise source in both n-type as well as p-type sub-micron MOSFETs. Time-domain RTS measurements lead to a better understanding of the RTS noise. The time-domain analysis was used to extract the RTS parameters under periodic large-signal excitation, which would otherwise (in the frequency-domain) have not been possible, thus providing more insights into the cyclo-stationary RTS behavior. The RTS parameters under periodic large-signal excitation conditions (cyclo-stationary RTS) differ from the parameters under steady-state. The analytical expression for the noise PSD of an RTS holds good for cyclo-stationary RTS, in the low-frequency range below the switching frequency of the RTS.

Trap behavior under transient biasing conditions that is not observable in steady-state was investigated, thus providing more insight in trapping and de-trapping mechanisms. The RTS measurements in the time-domain for the transient bias case showed that the instantaneous trap-occupancy does not follow the instantaneous step-voltage but instead it changes exponentially to reach the steady-state value. Existing circuit simulators implicitly assume an instantaneous change in the trap-occupancy with changing gate-bias, thus giving erroneous noise predictions under periodic bias excitation. When the large-signal excitation frequency is higher than the RTS corner frequency, the trap-occupancy does not follow the applied input signal, but is somewhere in between the 'off' and the 'on' state trap-occupancy. This cyclo-stationary RTS trap-occupancy is a constant and can be determined by the cyclo-stationary RTS time-constants in a similar way as the steady-state trap-occupancy. The significant change in the RTS noise due to the periodic large-signal excitation is primarily because of the sharp decrease in the cyclo-stationary $\overline{\tau_e}$. This implies that the change (increase or decrease) in the RTS noise under periodic large-signal

excitation is the highest for traps located deeper in the oxide because deeper the trap in the oxide, the more sensitive $\overline{\tau}_e$ is to changes in the applied gate bias. An analytical model is presented which accurately predicts the RTS parameters and noise spectra, in steady-state as well as under large signal excitation. All the model parameters have a physical significance and the model shows excellent agreement with measured data on a single RTS. Given a distribution of traps in energy and location, the model can be extended to accurately predict the trap-related low-frequency noise in MOSFETs, under varying bias conditions, leading to better optimization of analog and RF designs.

Finally, the low-frequency noise in hot-carrier degraded devices with H_2/N_2 and D_2/N_2 ambient during the post metal anneal under steady-state and under periodic large-signal excitation, is investigated. The low-frequency noise under periodic large-signal excitation increases more rapidly due to hot-carrier degradation as compared to the low-frequency noise measured under steady-state. The useful noise reduction, due to periodic large-signal excitation under non-stressed conditions, diminishes, as the devices are subjected to hot-carrier stress. Devices with D_2/N_2 ambient during post metal anneal show better resistance against hot-carrier injection than those with H_2/N_2 ambient during post metal anneal. This analysis illustrates the diagnostic capabilities of the presented noise model and measurement technique.

Samenvatting

De studie van laagfrequente ruis in MOSFETs wordt belangrijker naarmate de device afmetingen kleiner worden. Laag-frequente ruis beperkt niet alleen het dynamisch bereik bij lage frequenties maar ze wordt ook getransformeerd naar radio-frequenties (RF) in elektronische schakelingen zoals oscillatoren en mixers. Daarom zijn de modellering van de laag-frequente ruis en de technieken om zijn invloed te verminderen, van groot belang. In de literatuur is gerapporteerd dat de laag-frequente ruis in MOSFETs significant vermindert wanneer de gate bias-spanning periodiek wordt geschakeld. Echter, de beschikbare circuit-simulatoren hebben dit fenomeen niet in hun modellen opgenomen. In dit proefschrift wordt de laag-frequente ruis van MOSFETs onderzocht, zowel in stationaire toestand als onder schakelende bias-condities. Als de laag-frequente ruis in MOSFETs wordt gedomineerd door de zogenaamde Random Telegraph Signaal (RTS) ruis, is deze het meest gevoelig voor veranderingen in de bias-spanning. Terwijl het periodiek aan-/uitschakelen met succes wordt gebruikt om de laag-frequente RTS ruis te verminderen, zijn er ook voorbeelden van devices waarbij de laag-frequente ruis juist toeneemt bij periodiek veranderende bias. Dit kan verklaard worden doordat normaal in de stationaire toestand 'slapende' traps tengevolge van de wisselende bias 'geactiveerd' worden. De RTS ruis is de dominante ruisbron in zowel n-type evenals p-type submicron MOSFETs. RTS metingen in het tijd-domein leiden tot een beter inzicht in de RTS ruis. In tegenstelling tot de analyse in het frequentie-domein, maakt ruis-analyse in het tijd-domein het mogelijk om de RTS parameters onder periodieke groot-signaal aansturing volledig te bepalen. De analyse in het tijd-domein biedt meer inzicht in het cyclo-stationaire RTS gedrag. De RTS parameters in de periodiek schakelende toestand (cyclo-stationaire RTS) verschillen van de parameters in stationaire toestand. De analytische uitdrukking voor de spectrale ruis dichtheid (PSD) van een RTS geldt voor periodiek geschakelde MOSFETs in het frequentie gebied beneden de periode-frequentie van de RTS.

De eigenschappen van een trap onder veranderende bias-spanning, die niet waarneembaar zijn in stationaire toestand, zijn onderzocht. Daarbij is meer inzicht verkregen in de vangst- en emissie-mechanismen van de trap. De RTS metingen in het tijddomein voor veranderende bias-spanning tonen aan dat de momentane trap bezetting niet onmiddellijk de stap-spanning volgt. De trap bezettingsgraad verandert exponentieel naar de uiteindelijke waarde behorende bij de evenwichtstoestand. De bestaande circuit-simulatoren veronderstellen impliciet een onmiddellijk evenwicht van de trap-bezettingsgraad, passend bij de veranderende gate-spanning. Zij geven dientengevolge onjuiste voorspellingen van het ruisgedrag onder periodieke schakelende bias. Wanneer de frequentie van het groot-signaal schakelende bias signaal hoger is dan de RTS kantelfrequentie, volgt de trap

bezettingsgraad niet onmiddellijk het toegepaste inputsignaal maar zal zich ergens tussen de waardes voor de 'uit' en de 'aan' toestand bevinden. Deze cyclo-stationaire RTS trap bezettingsgraad is vrijwel constant en kan door middel van de cyclo-stationaire RTS tijdconstantes op een soortgelijke manier als bij de stationaire trapbezettingsgraad worden bepaald. De significante verandering in de RTS ruis tengevolge van de periodiek schakelende bias is hoofdzakelijk het gevolg van de scherpe daling van cyclo-stationaire emissietijd $\overline{\tau_e}$. Dit impliceert dat de verandering (verhoging of daling) in de RTS ruis onder periodieke groot-signaal aansturing het hoogst is voor dieper gelegen traps in het oxide, want hoe dieper de trap in het oxide ligt, des te gevoeliger is de emissietijd $\overline{\tau_e}$ voor veranderingen in de aangelegde gatespanning. In het proefschrift wordt een analytisch model voorgesteld dat de RTS parameters en de ruisspectra, in zowel de stationaire toestand als onder geschakelde condities, nauwkeurig voorspelt. Alle modelparameters hebben een fysische betekenis en het modelresultaat toont uitstekende overeenkomst met gemeten waarden voor één enkele RTS. Bij gegeven trapverdeling in energie en plaats, kan het model worden benut om nauwkeurig de trap-gerelateerde laag-frequente ruis in MOSFETs onder variërende bias, te voorspellen. Dit kan leiden tot betere optimalisering van analoge- en RF circuit ontwerpen.

Tenslotte werd de laag-frequente ruis onderzocht in devices met respectievelijk een H_2/N_2 en een D_2/N_2 post-metaal nabehandeling en die door hot-carrier injectie werden gedegradeerd. Ruismetingen werden uitgevoerd aan devices in stationaire toestand en aan devices met periodiek schakelende aansturing. De laag-frequente ruis tegen tengevolge van de hot-carrier degradatie neemt in de geschakelde MOSFET sneller toe dan in de MOSFET met constante bias. De nuttige ruis-reductie tengevolge van periodiek schakelende bias-spanning is vóór de hot-carrier degradatie groter dan nadat de devices aan hot-carrier injectie zijn onderworpen. De devices die een postmetaal nabehandeling ondergingen in een D_2/N_2 omgeving, blijken beter bestand tegen hot-carrier injectie dan devices die hun postmetaal nabehandeling in een H_2/N_2 omgeving ondergingen. Deze analyse illustreert de diagnostische mogelijkheden van het gepresenteerde ruismodel en de meettechniek.

List of Figures

1.1 Cycling V_{GS} between strong inversion (V_{GS-on}) and accumulation (V_{GS-off}) (Periodic large-signal excitation). 8

1.2 Comparing steady-state and periodic large-signal excitation. 10

2.1 Mathematical analysis of the PSD of a noise signal under periodic large-signal excitation (square wave modulated). 14

2.2 The expected noise reduction (in dB) in the LF noise PSD of a MOSFET under periodic large-signal excitation as a function of the duty-cycle of the excitation signal. [$20\log_{10}(100/\text{duty-cycle}(\%))$] 15

2.3 Setup for measuring noise under steady-state and under periodic large-signal excitation. 16

2.4 LF noise PSD of a p-MOSFET (W:L=10:1) with t_{ox}=10 nm, measured using our setup under steady-state and periodic large-signal excitation. α_H=3.5×10^{-4} for the steady-state spectrum. Also shown is the expected 6 dB noise reduction for a 50% duty-cycle of the excitation large-signal. The LF noise PSD under periodic large-signal excitation is lower than the expected 6 dB noise reduction. 18

2.5 LF noise PSD of a p-MOSFET with smaller gate area (W:L=10:0.3) under steady-state and periodic large-signal excitation. The steady-state LF noise PSD is not $1/f$ in nature. 19

2.6 Noise PSD (dB) in a p-MOSFET by changing the 'off' voltage of the periodic large-signal with a 50% duty-cycle. α_H=6×10^{-4} for the steady-state spectrum. Also shown is the noise reduction (dB) (calculated at f=100 Hz) as a function of the 'off' voltage of the periodic large-signal and the expected 6 dB noise reduction for a 50% duty-cycle of the excitation signal. 20

2.7 Steady-state LF noise PSD of p-MOSFETs (W:L=10:1) with varying t_{ox}. A fixed drain-current of 17 μA is forced through all the devices. LF noise PSD reduces as the gate-oxide are reduced. 21

2.8 LF noise measured under steady-state on p-MOSFETs (W:L=10:1) with varying t_{ox} at f=100 Hz and f=5 kHz. 22

2.9 Noise reduction (dB) obtained by periodic large-signal excitation plotted as a function of the corresponding steady-state LF noise, for different p-MOSFETs with different t_{ox} (W:L=10:0.3). 23

2.10 Noise reduction (dB) obtained by periodic large-signal excitation versus the gate oxide thickness for different p-MOSFETs (W:L=10:0.3). 24

3.1 Noise (random) waveforms from an ensemble $v(t)$, as a function of time. . 29
3.2 RTS Noise Spectra for different values of $\overline{\tau}_1/\overline{\tau}_0$ using Eqn.3.28 ($\overline{\tau}_0 = 1s$). The nature of the RTS spectrum is a Lorentzian, comprising of a flat part and a 20 dB/decade roll off. 35
3.3 RTS Noise power for different values of $\overline{\tau}_1/\overline{\tau}_0$ using Eqn.3.29 ($\overline{\tau}_0 = 1s$). It can be clearly seen that the noise power reaches its maximum when the ratio is 1. 36
3.4 Noise which is modulated by large-signal excitation (f_o). The noise is replicated and translated by each harmonic of the excitation frequency, resulting in correlations at frequencies separated by kf_0. 37
3.5 RTS in steady-state and periodic large-signal excitation. Sampling during the 'on' states and joining them together gives a cyclo-stationary RTS. The 'on' state is indicated by the shaded part and the white part indicates the device 'off' state. RTS is visible only in the shaded part ('on' state). . 38
3.6 Useful transitions in the noisy RTS data can be detected by calculating the time derivative of the RTS, and comparing it to a noise threshold level. The clean RTS is then constructed from these transitions. 41
3.7 Procedure for separating the background noise from the RTS. The RTS amplitude is subtracted from the 'high' state to give the background noise. 41
3.8 An RTS observed on a p-MOSFET, V_{GS} =-1.1 V, V_{DS} =0.2 V (Arbitrary units along the X and Y axis). Note the distinction in the RTS level and the device background noise. 42
3.9 Steady-state RTS parameter extraction of time-constants. The statistical distribution of the times in the 'high' and 'low' states. The markers indicate the times in the RTS state and the lines are the best fit. 43
3.10 RTS Noise PSD measured (spectrum analyzer) and calculated (analytical expression and parameter extraction) under steady-state conditions. V_{GS} = -1.15 V, V_{DS} = 2.0 V; $V_T \approx$ -1.0 V. 43
3.11 Signal-level histogram of an RTS observed in a MOSFET in the steady-state. The data points are grouped into two distinct levels corresponding to the RTS level. 44
3.12 The PSD of an RTS in steady-state measured on a p-MOSFET with W:L=10:0.3, $V_T \approx$ -0.9 V, V_{GS} = -1.1 V, using a spectrum analyzer. Also shown is the computed PSD of the device background noise and the $1/f$ slope (α_H = 6.8×10^{-6}). 45
3.13 Cyclo-stationary RTS parameter extraction of time-constants. The histogram of the times in the 'high' and 'low' states. The distribution is exponential and the mean and the standard-deviation are equal. 46

3.14 The measured PSD of an RTS under periodic large-signal excitation for a p-MOSFET with W:L=10:0.3, $V_T \approx$ -0.9 V. V_{GS} is switched between -1.1 V and 0 V, f_{sw} = 10 kHz, Duty-cycle=50%. Also shown are the calculated PSD of the cyclo-stationary RTS (6 dB above the measured PSD) and the device background noise. 47
3.15 Measured noise PSD (spectrum analyzer), and calculated noise PSD (Machlup's analytical PSD expression and parameter extraction) for an RTS in steady-state and under periodic large-signal excitation (cyclo-stationary RTS). . . 48

4.1 Steady-state LF noise spectrum and LF noise spectra under periodic large-signal excitation for two 'off' voltages ($V_{GS-off1}$ and $V_{GS-off2}$), measurement and simulated using our model. Also shown is the LF noise predicted by circuit simulator 'Spectre-RF' in steady-state and periodic excitation with a 50% duty-cycle. 52
4.2 Different types of charges associated with the Si-SiO_2 interface. 53
4.3 The basic processes involved in recombination by trapping: (a) denotes electron capture, (b) electron emission, (c) hole capture and (d) denotes hole emission. 56
4.4 The band bending in an n-MOSFET. The dotted lines show the change corresponding to an increase in the gate voltage (ΔV_G). $\Delta\psi_s$ is the change in the surface potential. ϕ_B denotes the potential of the bulk Fermi-level F_p with respect to the intrinsic level E_i. 57
4.5 A p-substrate two-terminal MOS structure under gate bias. The graph on the right indicates the potential distribution along the MOS structure from gate to bulk. 58
4.6 'Tunneling and Capture' (dotted arrows), and 'Capture and Tunneling' (solid arrows) mechanisms for the capture and emission process for a trap located in the oxide at a distance X_T from the interface for an n-MOSFET. The arrows indicate electron transitions. Also shown is the trap energy E_T in the oxide as function of the applied gate voltage. 60
4.7 The surface potential ψ_s at the drain-side as a function of the gate-to-source voltage V_{GS} for different values of drain-to-source voltage V_{DS}. V_{FB}=-1.6 V. 63
4.8 RTS time constants $\bar{\tau}_e$ and $\bar{\tau}_c$ as a function of V_{GS} variation for V_{DS} = 50 mV, measurements and simulation, for a trap located at the interface. . . . 64
4.9 RTS time constants $\bar{\tau}_e$ and $\bar{\tau}_c$ as a function of V_{GS} variation for V_{DS} = 40 mV, measurements and simulation, for a trap located in the oxide. 64
4.10 Technique for measuring the instantaneous occupancy. The instantaneous trap occupancy is calculated by averaging the state of the RTS over many RTS frames, during the 'on' period. 68
4.11 Measured and simulated instantaneous occupancies during the 'on' transients for three different RTS on three different devices. 68
4.12 Measured and simulated instantaneous occupancies during the 'off' transients for two different RTS. 69

4.13 Instantaneous occupancy under periodic large-signal excitation simulated using the model. The excitation frequency (f_{sw}) is higher than the corner frequency of RTS. Also shown is the averaged occupancy which lies between the steady-state occupancies in the 'on' and 'off' states. 70
4.14 Model for determining the cyclo-stationary RTS time parameters under periodic large-signal excitation (square-wave at the gate corresponding to two states 'on' and 'off'). 72
4.15 Cyclo-stationary RTS time constants $\overline{\tau_c}$ and $\overline{\tau_e}$ as a function of varying duty-cycle for two different RTS. RTS1410: $V_{\mathrm{GS-on}}$ = 0.6 V, $V_{\mathrm{GS-off}}$ = -0.2 V, V_{DS} = 40 mV, f_{sw} = 10 kHz. RTS0611: $V_{\mathrm{GS-on}}$ = 0.22 V, $V_{\mathrm{GS-off}}$ = 0.0 V, V_{DS} = 40 mV, f_{sw} = 16.7 kHz. 73
4.16 Cyclo-stationary RTS time constants $\overline{\tau_c}$ and $\overline{\tau_e}$ as a function of the excitation frequency (f_{sw}) for $V_{\mathrm{GS-on}}$ = 0.6 V, $V_{\mathrm{GS-off}}$ = -0.2 V, V_{DS} = 40 mV, duty-cycle = 50%. 73
4.17 Cyclo-stationary RTS time constants $\overline{\tau_c}$ and $\overline{\tau_e}$ as a function of $V_{\mathrm{GS-off}}$ for $V_{\mathrm{GS-on}}$ = 0.6 V, V_{DS} = 50 mV, duty-cycle = 50%, f_{sw} = 31.6 kHz. 74
4.18 LF RTS noise spectra under steady-state and large-signal periodic excitation (cyclo-stationary RTS). f_{sw} = 31.6 kHz, $V_{\mathrm{GS-on}}$ = 0.6 V, $V_{\mathrm{GS-off}}$ = -0.5 V, duty-cycle = 50%. 76

5.1 The LF noise PSD of a fresh and hot-carrier stressed DUT (stressing time 1000s) measured under steady-state and under periodic large-signal excitation. The LF noise after stressing is measured in the reverse mode. . . . 81
5.2 The LF noise of fresh and hot-carrier stressed DUT measured under steady-state and under periodic large-signal excitation for different stressing times. Also shown is the shift in the threshold voltage of the DUT before and after stress. 82
5.3 The distribution of the LF noise measured at 10 Hz on devices spread over the wafer under similar biasing conditions. LF noise measurements were done under steady-state and under periodic large-signal excitation for different hot-carrier stress times. 83
5.4 Comparison of LF noise measured under steady-state and periodic large-signal excitation on devices with D_2/N_2 and H_2/N_2 gas during post-metal anneal, before and after hot-carrier stressing. 84
5.5 The change in the LF noise measured under steady-state and under periodic large-signal excitation versus the corresponding shift in the threshold voltage for DUTs (H_2 and D_2 passivated) under hot-carrier stress. 85

1 Introduction

BROADLY speaking, sound waves with amplitudes above a certain bearable threshold are termed as noise. Those who find that too much noise makes them ill will not be surprised that the word noise can possibly be traced back to the Latin word *nausea*, 'seasickness', feeling of sickness. The meaning 'seasickness' gradually changed to a more general sense of discomfort or something unwanted and undesired.

Scientifically though, noise is an intriguing phenomenon which finds a place in all branches of study. In astrophysics, cosmic noise is the random noise that originates outside the Earth's atmosphere. Random fluctuation in any physical parameter is termed as noise. Mathematically noise is a random process. In electrical and communication engineering noise is a disturbance, especially a random and persistent disturbance, that obscures or reduces the clarity of a signal.

1.1 Noise in Semiconductors

Although, noise is a universal phenomenon, the noise considered in this thesis is the noise in electronic circuits caused by the small current and voltage fluctuations that are generated within the semiconductor devices themselves. The study of noise is important because it provides information on the lower limits of the signal being processed by a circuit without significant deterioration in the signal quality. In electronics and communication, the signal-to-noise ratio, often written S/N or SNR, is a measure of signal strength relative to background noise. The ratio is usually measured in decibels (dB). The goal is always to maximize the S/N ratio within certain power constraints. With decreasing device dimensions in modern electronic circuits, the signal levels being processed are also

very low, decreasing the SNR. This has led to a growing importance in the study of noise in semiconductor devices and to efforts towards reducing the noise so as to maximize the SNR. The various sources of noise in semiconductor devices are as follows [1]:

1.1.1 Shot Noise

Shot noise is the noise associated with the direct-current flow and is present in diodes and bipolar transistors. Shot noise refers to the random fluctuations of the electric current, which are caused by the fact that the current is carried by discrete charges (electrons). The strength of this noise increases with growing magnitude of the average current flowing through the diode. It can be shown that if a current I is composed of a series of random independent pulses with average value I_D, the resulting (shot) noise current has a mean-square value

$$\overline{i^2} = 2qI_D\Delta f \tag{1.1}$$

where q is the electronic charge, Δf is the bandwidth in Hertz. The shot noise spectral density is independent of the frequency. Noise sources which are independent of the frequency are categorized as *white noise*. The name white noise is because all different frequency components are present with the same strength. Shot noise is to be distinguished from current fluctuations in equilibrium, which happen without any applied voltage or without any average current flowing.

1.1.2 Thermal Noise

Thermal noise as the name suggests is the noise associated with the thermal random motion of the charge carriers. Thermal noise is unaffected by the presence or absence of direct current, since the electron drift velocity is much less than the electron thermal velocity. Thermal noise is directly proportional to the the absolute temperature (T) and as T approaches zero, the thermal noise also approaches zero. The thermal noise in a resistor R is represented by a voltage generator ($\overline{v^2}$) in series with R or a current generator ($\overline{i^2}$) parallel to R given by

$$\begin{aligned} \overline{v^2} &= 4kTR\Delta f \\ \overline{i^2} &= 4kT\frac{1}{R}\Delta f \end{aligned} \tag{1.2}$$

where k is Boltzmann's constant. Eqn.1.2 shows that the thermal noise spectral density is independent of the frequency and thus thermal noise can also classified as white noise. Thermal noise is a fundamental physical phenomenon and is present in any passive resistor. Both shot noise and thermal noise are classified as white noise having gaussian amplitude distributions and are indistinguishable once they are introduced in a circuit.

1.1.3 Flicker or $1/f$ Noise

Flicker noise is found in all active devices as well as passive elements. The origins of flicker noise are varied and are discussed in the following section. Flicker noise is always

associated with the flow of direct current and displays the spectral density of the form

$$\overline{i^2} = K\frac{I^a}{f^b}\Delta f \tag{1.3}$$

where Δf is small bandwidth at frequency f, I is the direct current, K is a parameter associated with the device, a is a parameter in the range 0.5 to 2, and b is a parameter with a value of about unity. In Eqn.1.3 if $b = 1$, the noise spectral density has a $1/f$ frequency dependence and hence the name '$1/f$' noise. In general, for $0.9 < b < 1.1$ the term $1/f$ is used and outside the range we have $1/f$-like noise. It is quite apparent that this noise source is most significant at low-frequencies, although in devices exhibiting high flicker noise, this noise may dominate the device noise at high frequencies well into the megahertz range. Flicker noise is often called 'pink noise' because of the frequency dependence of the power spectral density. (Any noise source which shows a frequency dependence is called 'colored noise'). The adjective 'ubiquitous' is often used in terms of $1/f$ noise as it manifests itself in widely different systems apart from electronic devices, such as radioactive decay, chemical systems, biology, fluid dynamics, astronomy, optical systems, network traffic and economics.

1.1.4 Generation Recombination Noise (RTS Noise)

In a semiconductor, free carriers are necessary for the drift and diffusion conduction mechanisms. The generation process involves the creation of free carriers, and the recombination process involves the trapping of these free carriers in defects. The trapped carrier will be freed again after only a short time because of the thermal energy of the crystal lattice. This process is a series of independent discrete events. Each event causes fluctuation in the number of free carriers leading to a fluctuation in the material conductance. This fluctuation in the conductance leads to the generation-recombination noise when there is a current flow. The generation-recombination noise is a low-frequency noise. A single trapping-detrapping event leads to a Random Telegraph Signal (RTS). The power spectral density of an RTS is a Lorentzian [2]. The charge fluctuation results in the fluctuation of the surface potential, which in turn modulates the channel carrier density.

1.1.5 Other Noise Sources

In addition to the above mentioned noise sources, there is another type of low-frequency noise found in integrated circuits and discrete transistors called 'burst noise'. The source of this noise source is not fully understood and it has been shown to be related to the presence of heavy-metal ion contamination in the devices. Another form of noise produced by zener or avalanche breakdown in p-n junctions is called 'avalanche noise'. In avalanche breakdown, holes and electrons in the depletion region of a reverse biased p-n junction acquire sufficient energy to create hole-electron pairs by colliding with silicon atoms. This process is cumulative, resulting in large random noise spikes.

In this thesis our focus is primarily on the low-frequency noise in MOSFETs. Our interest in the low-frequency noise in MOSFETs stems from the fact that with down-

scaling the low-frequency noise in MOSFETs is increasing. This is a cause for concern as it limits the optimization of circuit design. Moreover, the effect of noise is not limited to low frequencies but is sometimes up-converted to high frequencies [3], e.g., in active mixers, voltage controlled oscillators (VCO) [4], and frequency dividers [5]. This is one of the important difficulties in implementing analog CMOS circuits with similar noise performance as their bipolar counterparts.

1.2 MOSFET $1/f$ Noise Models

MOSFET noise measurements at low-frequencies generally show a noise spectral density which is roughly inversely proportional to frequency ($1/f$ or $1/f$-like noise). The $1/f$ noise in MOSFETs has been extensively studied for more than four decades [6]. In spite of extensive efforts to identify the physical origins of the current fluctuations, a universally accepted model for simulating $1/f$ noise is still lacking. Two theories have been proposed to explain the physical origins of the flicker noise. It is generally accepted that fluctuations in the conductivity of the MOSFET channel are responsible for the $1/f$ noise. The conductivity is given by

$$\sigma = \mu\, n\, q \tag{1.4}$$

where μ is the mobility of the carriers, n is the concentration of mobile charge carriers, and q is the electron charge. From Eqn.1.4 a fluctuation in the conductivity can be due to either a change in the number of carriers (ΔN) or a change in the channel mobility ($\Delta\mu$).

1.2.1 ΔN

In the carrier number fluctuation theory [7–12], originally proposed by McWhorter [13], the flicker noise is attributed to the random trapping and detrapping of charge carriers in oxide traps with different relaxation times near the Si-SiO_2 interface. A single trapping-detrapping event leads to a RTS. The trapping-detrapping process is made possible by the tunneling of charge carriers from the channel into the oxide into traps or defect locations. The RTS spectrum [2] corresponds to transitions between the conduction band and a trap with relaxation time τ

$$S(\tau) = (\overline{\Delta N})^2 \frac{4\tau}{1+\omega^2\tau^2} \tag{1.5}$$

If the different kinds of traps have statistical weights

$$g(\tau)d\tau = \frac{c}{\tau}d\tau \tag{1.6}$$

Then the summation of the RTS spectra gives an $1/f$ spectrum.

$$S = \int_0^\infty g(\tau)S(\tau)d\tau = \int_0^\infty \frac{c}{\tau}(\overline{\Delta N})^2 \frac{4\tau}{1+\omega^2\tau^2}d\tau = 4c(\overline{\Delta N})^2 \frac{1}{f} \tag{1.7}$$

Thus, according to the number fluctuation model for $1/f$ noise in MOSFETs, the power spectral density is obtained by a superposition of relaxation processes with Lorentzian

spectra and a distribution of time constants. An appropriate distribution of time constants is required to give the $1/f$ law over an extensive range of frequency. In order to extend this to ten decades, the spread in time constants must cover many orders of magnitude. In MOSFETs, it is possible to invoke a physical mechanism (tunneling in the oxide) which could account for relaxation times distributed between, say, 10^{-5} and 10^{+8}s. McWhorter showed that a uniform spatial distribution of oxide traps near the interface will give rise to a distribution of time constants which add up to yield the $1/f$ noise spectrum. Therefore, τ depends exponentially on x, the distance from the interface into the oxide.

$$\tau = \tau_0 e^{x/\lambda} \tag{1.8}$$

where λ is the effective penetration depth. If the number of traps is T, we get

$$\frac{dT}{d\tau} = \frac{dT}{dx}\frac{dx}{d\tau} = \frac{dT}{dx}\frac{\lambda}{\tau} \tag{1.9}$$

which gives the needed $1/\tau$ distribution needed to explain the $1/f$ noise spectrum. The number fluctuation model is supported by the widely observed correlation between the flicker noise and the interface trap density [8, 10, 14–17].

1.2.2 $\Delta\mu$

The $1/f$ noise is a fluctuation in the conductivity of metals and semiconductors. The power spectral density is proportional to $1/f$ over a wide range of frequencies. The noise can be measured with simple equipment between 10^{-2} Hz and 10^{5} Hz. The noise of homogeneous layers can be expressed by Hooge's empirical relation [18–21]:

$$\frac{S_I}{I^2} = \frac{\alpha_H}{fN} \tag{1.10}$$

where I is the total current flowing through the sample, S_I is the spectral density of the noise in the current, N is the total number of carriers, and α_H is the Hooge's parameter an empirical constant with a value between 10^{-6} and 10^{-4} [22, 23]. To determine whether the conductivity fluctuations are due to ΔN or $\Delta\mu$ one needs to determine effects where N and μ do not appear as a product. Examples of such effects are the Hall effect, thermo e.m.f., hot-electron effects, etc. The Hall effect in GaAs [24] is an example which demonstrates that the noise measured across the Hall contacts follows the mobility fluctuations ($\Delta\mu$).

The mobility is determined by scattering of free electrons. Lattice scattering by acoustic lattice vibrations is always present. Other scattering mechanisms include: impurity scattering and electron scattering. The contribution of the two mechanisms resulting in the mobility μ is given by Matthiessen's rule

$$\frac{1}{\mu} = \frac{1}{\mu_{latt}} + \frac{1}{\mu_{imp}} \tag{1.11}$$

The observed noise is plotted as $\log\alpha_H$ versus $\log\mu$ [25]. The $\alpha_H - \mu$ dependence experimentally found can only be explained by assuming lattice scattering alone [25]. Thus we get

$$\frac{\Delta\mu}{\mu} = \frac{\Delta\mu_{latt}}{\mu_{latt}} \tag{1.12}$$

$$\alpha_H = (\frac{\mu}{\mu_{latt}})^2 \alpha_{latt} \tag{1.13}$$

Measuring the noise in the intensity of scattered light provides an independent way of proving that the intensity of acoustic lattice modes varies with a $1/f$ spectrum [22].

1.2.3 Unified (ΔN and $\Delta\mu$)

The number fluctuation model for the $1/f$ noise in MOSFETs seems more appropriate as the charge transport is at the interface. An additional evidence to support the number fluctuation theory is the increased $1/f$ noise in MOSFETs after degradation by hot electrons [26–28] or by ionizing radiations. Measurements on devices from many different CMOS processes with oxide thickness between 10 and 80 nm suggest that $1/f$ noise in n-MOSFETs behave as predicted by the number fluctuation model [29]. However, in the same study, the p-MOSFETs exhibit a lower $1/f$ noise, which is bias dependent, and is well explained by the mobility fluctuations model. Thus, in general, the $1/f$ noise in n-MOSFETs is best described by the number fluctuation model and the $1/f$ noise in p-MOSFETs by the mobility fluctuation model with the values of α_H lying between 3×10^{-7} and 10^{-3} [30].

Extensive $1/f$ noise measurements on MOSFETs give an indication of a more complicated dependence on the gate bias and oxide thickness which is not predicted by the number or mobility fluctuation models. A unified $1/f$ noise model incorporating both the number fluctuations and correlated surface mobility fluctuations mechanisms was proposed by Hung [31, 32]. The surface mobility fluctuations are attributed to the scattering effect of the oxide charge. As these fluctuations have the same source of origin they are correlated. The correlated mobility fluctuations in the unified model are different from the mobility fluctuations discussed earlier in the $\Delta\mu$ model whose origins are due to phonon scattering. The unified model is able to explain most noise data reported in literature and is widely used among circuit designers. In some cases, the unified model uses non-physical fitting parameters to predict the $1/f$ noise observed in p-MOSFETs [33]. The unified model has a functional form resembling the number fluctuation model at low bias and the mobility fluctuation model at high bias. This model is often used as the basis for circuit simulations.

1.3 Low-Frequency Noise Reduction

Reducing the LF noise in MOSFETs would benefit circuit design greatly. In this section, known circuit techniques for noise reduction are reviewed briefly [34].

- *Operating in the ohmic region*: $1/f$ noise is directly related to the conductance variations. Thus, the noise reduces for a MOSFET operating in the triode region. But almost all transistor circuits require voltage amplification, and a MOSFET in the triode region has a maximum 'intrinsic voltage gain' of 1. In majority of applications, the MOSFETs are operating in the saturation region.

- *DC Offset and Drift Reduction Techniques*: DC offset and drift are basic problems in analog circuits, and several techniques have been developed to reduce the resulting low frequency errors. Examples of such techniques are chopper stabilization [35], auto-zeroing techniques (correlated double sampling [35]), dynamic element matching [36], dynamic current mirrors [37] and current copiers [38]. The reduction factor is typically limited by device mismatch, timing errors and charge injection. All these techniques are limited to use at low frequencies. They do not help to reduce up-converted $1/f$ noise.

- *Reduce the Up-conversion of Noise*: A theory was proposed to quantify the up-conversion effect of noise in oscillators [3]. The oscillator is modelled as a linear time variant system, and an impulse sensitivity function is defined that characterizes the sensitivity to up-conversion. Based on this theory, it can be shown that symmetry in the oscillator waveform helps to minimize the up-conversion [39]. However, the achievable symmetry is limited especially in cases where complementary devices are used. Furthermore, noise on the control input of a controlled oscillator remains a problem.

- *Phase-Locked Loops (PLL)*: In a PLL the phase of a VCO is locked to the phase of a reference signal by means of a phase detector with feedback loop. If the reference is clean, the PLL suppresses the phase noise of the VCO by an amount determined by the loop gain [1]. Although this is a very useful commonly used technique, it has its limitations. For frequencies larger than the loop bandwidth, the phase noise of the (effectively free running) VCO still determines the phase noise of PLL. Thus $1/f$ noise is still a problem.

1.3.1 Cycling from Inversion to Accumulation

The above mentioned circuit techniques are unable to reduce the intrinsic $1/f$ noise in MOSFETs.

A key factor in an effort to reduce low-frequency noise is to interfere with the self correlation of the physical noisy process and thereby reduce the noise by a rapid switching between two states: one state that is characterized by a significant generation of low-frequency noise and another state that is characterized by a negligible amount of low-frequency noise. Such an experiment was performed with a MOSFET biased in inversion with considerable low-frequency noise and an 'off' state biased in accumulation exhibiting negligible low-frequency noise [40]. The MOSFET was switched between the two states and sampled in the 'on' state for low-frequency noise measurements. The 'off'

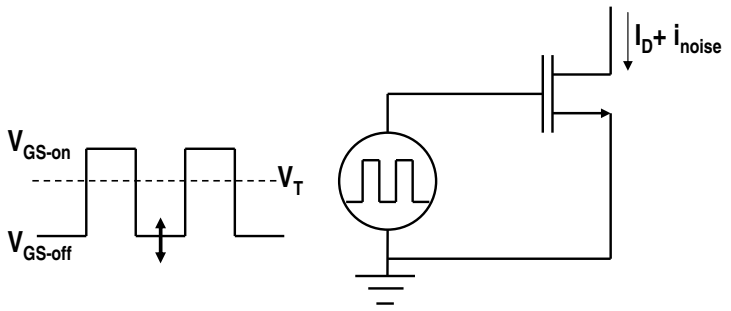

Figure 1.1 Cycling V_{GS} between strong inversion (V_{GS-on}) and accumulation (V_{GS-off}) (Periodic large-signal excitation).

states introduced between the noisy 'on' states reduce the low-frequency noise by interfering with the long time constants associated with trapping and detrapping processes, and hence with the long time memory that characterizes low-frequency noise.

A similar study was conducted on the RTS noise in MOSFETs by cycling between inversion and accumulation [41]. The RTS noise in the devices was observed to disappear when the transistors were cycled into accumulation.

1.3.2 Periodic Large-Signal Excitation

Bloom and Nemirovsky [40] were the first to report that cycling a MOSFET between strong inversion and accumulation reduces the low-frequency noise. Shortly after, their results were reconfirmed and related to RTSs observed on small geometry devices [41]. The effect was again observed in ring oscillator phase noise experiments [42], and seemed to be the first to use it in designing CMOS circuits.

Fig.1.1 illustrates the basic idea of cycling a transistor between a conductive state and a non-conductive state for an n-MOSFET. A voltage source with a square wave signal switches the gate-source voltage of the n-MOSFET between two bias values. The high level, V_{GS-on}, is larger than the threshold voltage, so that the transistor is biased at a constant voltage in strong inversion. This biasing corresponds to periodic large-signal excitation. In our approach, the low level, V_{GS-off}, is equal or lower than the threshold voltage and can be varied. Depending on V_{GS-off}, the low state of the square wave corresponds to biasing the MOSFET in moderate inversion, weak inversion or accumulation. The benefits of using such biasing scheme are two-fold. Firstly, using such a technique decreases the low-frequency noise, making better optimization of circuit design possible. Secondly the power consumption in the circuit is minimized as the MOSFET is not always 'on'. Biasing the MOSFET with a constant gate-to-source voltage corresponds to the steady-state. Fig.1.2 shows the comparison between a MOSFET in steady-state and under periodic large-signal excitation.

From our discussion in section 1.2, the low-frequency noise in sub-micron MOSFETs is expected to be composed of two major noise contributing mechanisms:

- *RTS noise*: This low-frequency noise has a Lorentzian power spectral density [2], and is caused by the charge trapping into defects in the oxide. These traps have a wide range of time constants. Shrinking MOSFET dimensions have made the RTS noise dominant.
- $1/f$ *noise*: Although the low-frequency noise is dominated by RTS noise in MOSFETs, other fluctuation mechanisms causing $1/f$ noise must occur as well. Especially the $1/f$ noise caused as a result of the mobility fluctuations.

The decrease in the low-frequency noise observed can be explained by the fact that the dominant RTSs, which are caused by carrier trapping into slow oxide states, no longer contribute to the noise of the system. We do not expect that setting the MOSFET in accumulation alters the lattice properties, or at least does not reset its long-term memory (this is indeed assuming that phonon-limited mobility is a lattice property, not a free-carrier property!) The technique indicates a possibility to identify and thus maybe to separate the contributions of different sources of $1/f$ noise in MOSFETs.

1.4 Scope

We have seen from the above discussions that the low-frequency noise is an important limiting factor for analog circuits. The noise is also of concern for future deep sub-micron digital circuits (bit errors). Furthermore, the effect of the low-frequency noise is not confined to low frequencies but it is also up-converted to Radio Frequencies (RF) in electronic circuits like oscillators and mixers. Hence the modeling of this low-frequency noise and techniques to reduce its effect are important, and are likely to become even more important in the future. It has been reported in literature that the low-frequency noise in MOSFETs decreases significantly under changing gate bias. Unfortunately, the circuit simulators available do not model this behavior [34]. Even circuit simulators that support time-variant noise sources (*e.g.* periodic steady-state analysis of Spectre RF), do not adequately model the observed effects.

The objective of this thesis is to characterize and model the low-frequency noise under periodic large-signal excitation. Special attention is paid to the dependence of the noise on parameters that can be manipulated in analog circuit design.

1.5 Outline

The outline of this thesis is as follows. *Chapter 2* deals with the spectral measurements of the low-frequency noise in MOSFETs under steady-state and under periodic large-signal excitation. Previous noise measurements on n-MOSFETs revealed that the low-frequency noise power spectral density decreases, when the transistor is switched 'off' periodically (periodic large-signal excitation) [34,42–44]. Similar experiments are carried

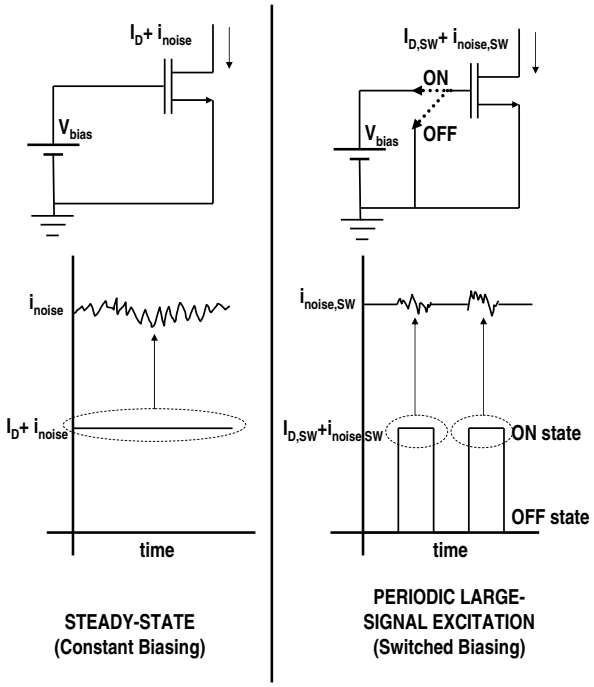

Figure 1.2 Comparing steady-state and periodic large-signal excitation.

out on p-MOSFETs with different device geometry and gate-oxide thickness (t_{ox}) [45,46]. The steady-state low-frequency noise and the noise under periodic large-signal excitation, are investigated as a function of the biasing conditions and are compared with each other. Our low-frequency noise measurements show that RTS noise emerges as a dominant noise source in sub-micron MOSFETs.

The RTS measurements on MOSFETs (both n-type and p-type) fabricated in a modern CMOS processes are discussed in detail in *chapter 3*. RTS noise under large-signal excitation is investigated and a novel RTS parameter extraction procedure in the time-domain to measure the RTS time-constants, under periodic large-signal excitation is proposed [47]. The extracted RTS parameters are verified by a comparison with the RTS noise power spectral density measured by a spectrum analyzer. The technique of determining the statistical lifetimes and amplitudes of the RTS by fitting the signal level histogram of the time-domain record to two gaussian histograms has been reported in literature [48, 49]. This procedure is used for analyzing the 'noisy' RTS along with the device background noise, which turned out to be $1/f$ noise [50]. The $1/f$ noise of the device is separated from the RTS using this procedure. The emphasis, in this chapter is on measuring RTS in the *time-domain*, under both steady-state and periodic large-signal excitation.

The primary objective of this thesis was to model the observed low-frequency noise

behavior. In *chapter 4* we present a physical RTS model, which can be used under steady-state and under large-signal excitation [51]. Our model results are verified by the time-domain RTS measurements under steady-state and periodic large-signal excitation presented in *chapter 3*. In addition, trap behavior under transient biasing conditions is investigated. This is normally not observable in steady-state. By using our time-domain RTS measurements during transient biasing and under periodic large-signal excitation we are able to predict the RTS time-constants when the device is 'off'!

The physical origins of the RTS noise are in defects in the gate-oxide and its interface. The reliability of the gate-oxide and its interface gains importance with down-scaling. In *chapter 5* we report the impact of hot-carrier stress on the low-frequency noise in MOSFETs under steady-state and under periodic large-signal excitation. The increase in the the low-frequency noise under steady-state and periodic large-signal excitation after hot-carrier stress is investigated.

The final conclusions drawn from the thesis are presented in *chapter 6*.

Noisy signals in another view,
Look completely different, if not new.
A composition of different frequencies... makes sense,
When viewing the signal with a Fourier lens.

The power spectral density,
Used extensively in our noise study,
Is measured by a spectrum analyzer,
Making the noise analysis a lot wiser!!

Increasing noise with scaling device dimension,
Is a growing problem, limiting circuit optimization.
Can this noise be reduced intrinsically ??
By turning the device 'off' periodically ??

2

Low-Frequency Noise - Spectral Analysis

THE low-frequency (LF) noise becomes a dominant factor in limiting the dynamic range of operation of the MOSFET with decreasing device sizes. The fluctuation in the drain current of a MOSFET is generally specified in terms of its mean-square variation about the average value. The noise current power spectral density (PSD), expressed as $\overline{i^2}/\Delta f$, mean-square current variation per unit bandwidth of frequency (with units A^2/Hz), is a very effective way of measuring the noise power of the fluctuation in drain current in a MOSFET under bias. As reported in the introduction chapter, cycling a MOSFET between strong inversion and accumulation reduces the low-frequency noise [40, 41]. In order to investigate this effect extensive LF noise measurements were carried out on MOSFETs. This chapter reports our spectral measurements of the LF noise in MOSFETs under steady-state and under periodic large-signal excitation. Previous noise measurements on n-MOSFETs revealed that the LF noise PSD decreases, when the transistor is switched 'off' periodically (periodic large-signal excitation) [34, 42, 43]. In this chapter, similar experiments were carried out on p-MOSFETs with different device geometry and gate-oxide thickness (t_{ox}). The steady-state (*constant bias*) LF noise and the noise under periodic large-signal excitation (*switched biased noise*), have been investigated as a function of the biasing conditions and were compared with each other. The p-MOSFETs show a similar LF noise reduction under periodic large-signal excitation as observed in n-MOSFETs, thus suggesting a common origin for the low-frequency noise in both n-type and p-type, small geometry MOSFETs.

This chapter is organized as follows: the first section deals with the mathematical analysis of the noise PSD under steady-state and under periodic large-signal excitation. In section two, the noise measurement setup is explained in detail. Also discussed are the steady-state and dynamic biasing conditions at which the noise measurements are carried

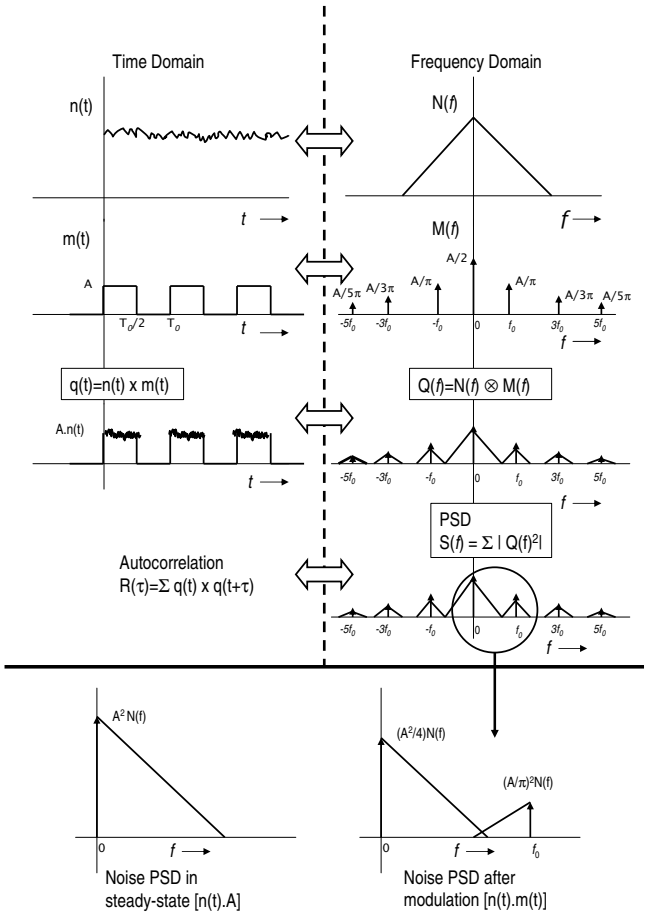

Figure 2.1 Mathematical analysis of the PSD of a noise signal under periodic large-signal excitation (square wave modulated).

out. Section 3, discusses the various results from the spectral noise measurements on the devices. Finally, the chapter concludes with discussions about the measurement results.

2.1 LF noise PSD

The PSD, describes how the noise power (or variance of a random variable) of a time series is distributed with frequency. Assume that the LF noise signal is a stationary random signal ($n(t)$). The PSD or power spectrum ($S(f)$) of such a signal is mathematically defined by the *Wiener-Khintchine theorem* as the Fourier Transform of the autocorrela-

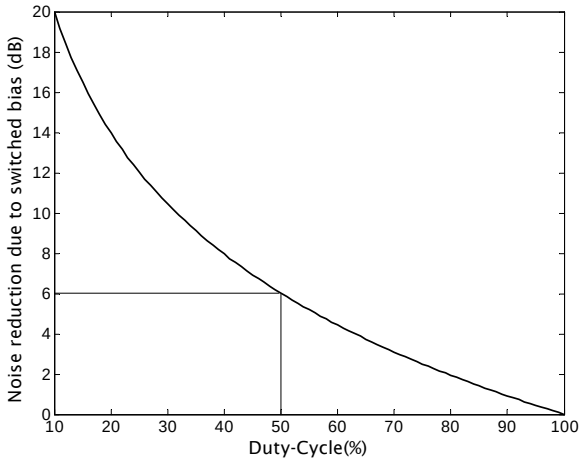

Figure 2.2 The expected noise reduction (in dB) in the LF noise PSD of a MOSFET under periodic large-signal excitation as a function of the duty-cycle of the excitation signal. [$20\log_{10}(100/\text{duty-cycle}(\%))$]

tion sequence of the random noise signal [52–54]. An equivalent definition of PSD is the squared modulus of the Fourier transform of the time series, scaled by a proper constant term.

Fig.2.1 shows the spectral analysis of a square wave modulated noise signal. $n(t)$ represents the LF noise in the MOSFET in time domain. The MOSFET is periodically switched 'off' with a duty-cycle of 50% under periodic large-signal excitation. This is equivalent to modulating $n(t)$ with a square wave $m(t)$. The fourier transform is represented by $Q(f)$. The PSD ($S(f)$) is the squared modulus of $Q(f)$. The PSD of an unmodulated noise signal (steady-state) is then compared with a noise signal which is modulated with a square wave (periodic large-signal excitation). If the PSD is expressed in dB (decibel), we can easily deduce that the PSD of a square wave modulated signal is $10log(A^2N) - 10log(A^2N/4)$ or 6.02 dB lower than the PSD of the unmodulated noise signal for frequencies below the switching frequency of the modulating square wave (f_0)(Fig.2.1). The first alias at f_0 (frequency of excitation) does not have a significant influence on the baseband signal as we are only interested in the LF noise. This can be easily verified by plotting the DC and first alias on a log-f plot.

Fig.2.2 shows the expected noise reduction in dB as a function of the duty-cycle of the switching gate signal, in the low-frequency range below the excitation frequency.

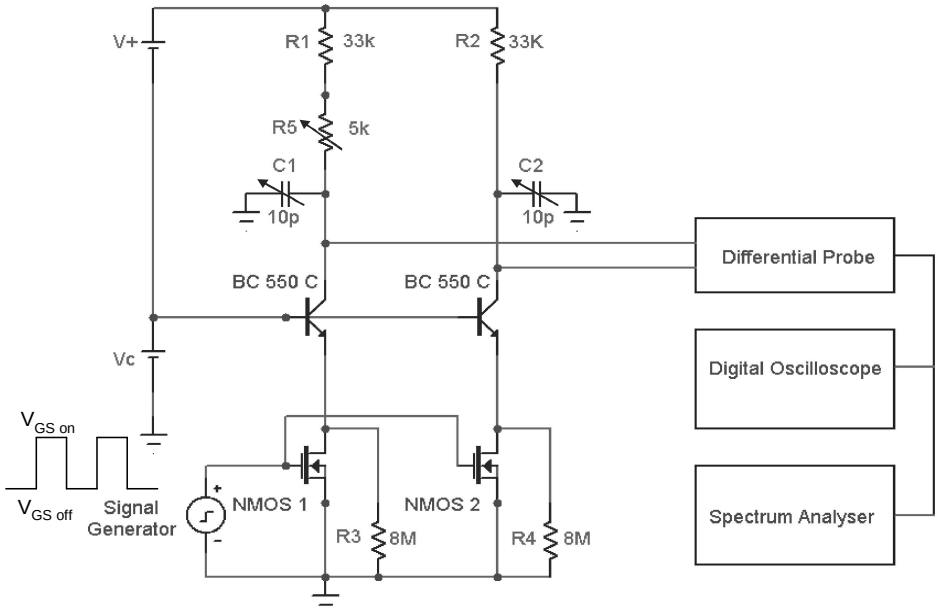

Figure 2.3 Setup for measuring noise under steady-state and under periodic large-signal excitation.

2.2 LF noise measurements

The setup shown in Fig.2.3 is used to study the noise spectra in n-MOSFETS in steady state (constant bias) as well as under periodic large-signal excitation (switched bias) [43].

2.2.1 Measurement Setup

A differential setup is used for measuring the LF noise PSD on a matched pair of MOSFETs. The differential probe (Tektronix 6046) is used to attenuate the common-mode signals which arise from the function generator or other noise sources thus providing a balanced operation of this circuit. If the MOSFETs do not match sufficiently, the differential input signal to the differential probe will be beyond the active range of the probe prohibiting a correct measurement. The setup measures the sum of the uncorrelated noise in the matched MOSFET pair. The LF noise can be associated with either of the MOSFETs by dividing the measured noise by two. With this setup, the LF noise of the MOSFETs is modulated by the repetitive switching ‘on’ and ‘off’ of the transistors. When the MOSFETs are switched ‘off’, the probe is connected to the supply voltage, and the differential noise it picks up (thermal noise from the two drain resistors) is negligible. Hence we expect, in the absence of other effects, to see a modulated LF noise spectrum.

The source and bulk of the MOSFET are connected to ground. The two cascode transistors (BC550) maintain the drain voltage of the MOSFETs at a nearly constant value of V_{BE} below the applied voltage V_C at the base of the NPN transistors. The resistors R_1 and R_2 convert the drain current of the MOSFET into an equivalent voltage which is fed to the differential probe. The resistors do not significantly contribute to the total noise that is seen by the probe as they are of very high resistance as compared to the MOSFET. The oscilloscope allows monitoring of the signal that goes to the spectrum analyzer. Since the probe has a high gain, DC balance adjustment is necessary before each measurement and is done by adjusting the drain resistor (R_5) and trimming capacitors (C_1, C_2). Batteries are used for generating the necessary voltages in the circuit to minimize the 50 Hz interference. The gate voltage of the MOSFET is controlled by a function generator (HP 8904A Multi-function synthesizer, HP 8112A pulse generator) which provides for a constant biasing (steady-state) or a periodic large-signal excitation as is required for the measurement. The spectrum analyzers used in the measurement setup (HP4195A spectrum analyzer and the E550 Phase Noise Setup) to measure the noise PSD of the devices under test. The E550 measures the noise PSD in units dBV^2/Hz while the HP4195A uses dBμV/$\sqrt{Hz}$.

This simple setup can be easily realized using standard equipment, and allows for easy measurement over a relatively large frequency range. In order to verify that the measured noise power is indeed originating from the MOSFET, and not due to something else in the measurement setup, we measure the noise floor of the setup by measuring the noise-power when the MOSFET is 'off' and the probe and probe preamplifier connected to the spectrum analyzer. The noise floor is found to be significantly lower than the noise spectra measured. The measurement setup measures the output drain-current noise PSD. The input referred noise PSD can be determined by dividing by the square of the transconductance ${g_m}^2$.

The setup for measuring noise on p-MOSFETs is functionally similar to the one used above (Fig.2.3. The cascode NPN transistors replaced by PNP transistors, in addition to the changes needed in the supply voltages for the p-MOSFETs. The functioning of the noise measurement setup for p-MOSFETs is similar to that of the n-MOSFET measurement setup [46].

2.2.2 Measurement Conditions

The LF noise measurements on n-MOSFETs under steady-state and under periodic large-signal excitation have been reported earlier [43, 44]. However, it was not known if p-MOSFETs exhibited a similar behavior and hence p-MOSFETs were used in this study. The p-MOSFETs on which the LF noise measurements are done have a geometry of W:L=10:0.3 and W:L=10:1 (W and L are the width and length of the p-MOSFET in μm). The p-MOSFETs have a substrate doping of 5×10^{17}cm^{-3}, and t_{ox} of 2.0; 3.6; 7.5; 10 and 20 nm.

The first set of p-MOSFET noise measurement involves changing the 'off' voltage of the switching gate signal. The $V_{GS} - V_T$ value was kept at around 0.4 V, ensuring that the p-MOSFETs were in the saturation region, and also in strong inversion. The 'off'

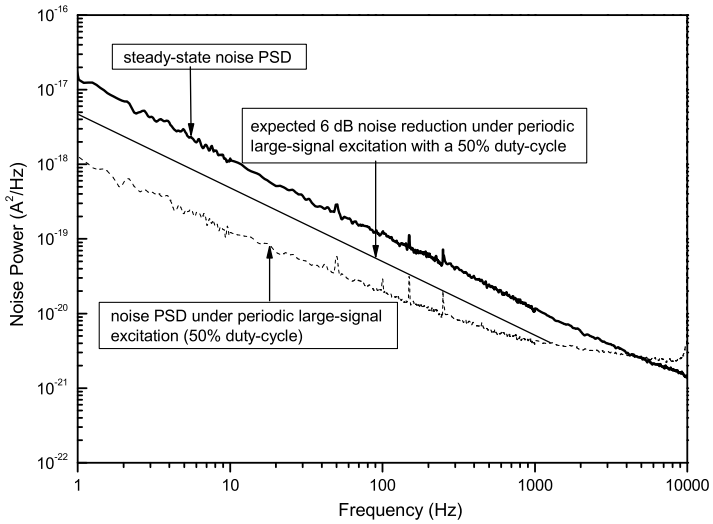

Figure 2.4 LF noise PSD of a p-MOSFET (W:L=10:1) with t_{ox}=10 nm, measured using our setup under steady-state and periodic large-signal excitation. α_H=3.5$\times 10^{-4}$ for the steady-state spectrum. Also shown is the expected 6 dB noise reduction for a 50% duty-cycle of the excitation large-signal. The LF noise PSD under periodic large-signal excitation is lower than the expected 6 dB noise reduction.

gate bias voltage was then systematically varied from, just below the threshold voltage to well below the threshold voltage, and the corresponding switched bias noise is measured. The duty-cycle of the switching gate signal was also varied during the LF noise measurements. The constant biased LF noise measurements were also done on p-MOSFETs with different t_{ox}. For all measurements a constant drain-current (I_D) has to be used for a fair comparison between the measurements. In our case a constant drain current of 17 μA was forced through the p-MOSFETs, during the constant dc bias measurements.

2.3 Measurement Results

Fig.2.4 shows the noise PSD of a p-MOSFET (W:L=10:1), under steady-state and under periodic large-signal excitation. The noise spectra between 1 Hz and 10 kHz are shown for the steady-state case (no switching) and for the periodic large-signal excita-

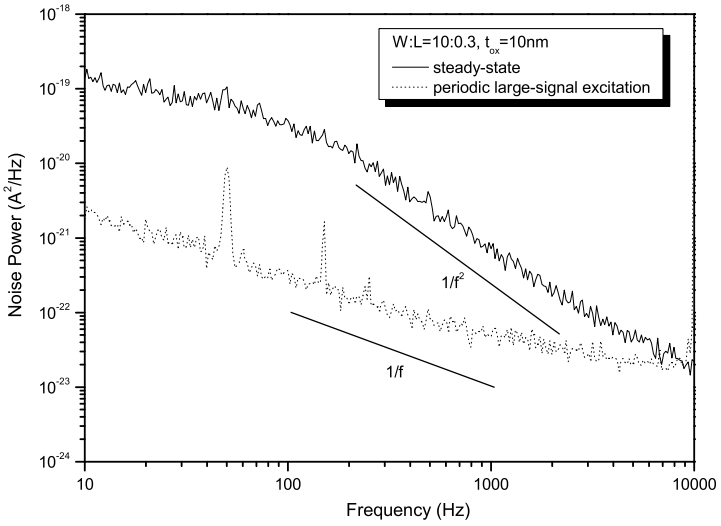

Figure 2.5 LF noise PSD of a p-MOSFET with smaller gate area (W:L=10:0.3) under steady-state and periodic large-signal excitation. The steady-state LF noise PSD is not $1/f$ in nature.

tion of frequency 10 kHz and a duty-cycle of 50%. On comparing the LF noise power under steady-state and under periodic large-signal excitation for the same measurement bandwidth, we observe a noise reduction of more than 6 dB, when the transistors are periodically switched 'off'. Also shown in the figure is the 6 dB expected noise reduction as compared to the steady-state case, for a 50% duty-cycle of the excitation large-signal. In order to make a comparison between a large number of devices, an empirical measure for the 'noisiness' of each device is needed. Integrating the measured noise PSD in a given bandwidth gives us the noise power of the device. This integration is done both for the steady-state case and for the periodic large-signal excitation. The difference between these two averages gives the noise reduction. If the LF noise PSD is $1/f$ in nature then the noise power at f=1 Hz, is simply f times the noise power at frequency f. The noise reduction (dB) (provided the slope of the LF noise PSD for both the steady-state and the periodic large-signal excitation is the same for a given bandwidth) is the difference between the LF noise power under steady-state and under periodic large-signal excitation. In our measurements the LF noise is measured in the linear portion of the noise spectrum at 100 Hz.

Fig.2.5 shows the noise PSD of a p-MOSFET (W:L=10:0.3), under steady-state and

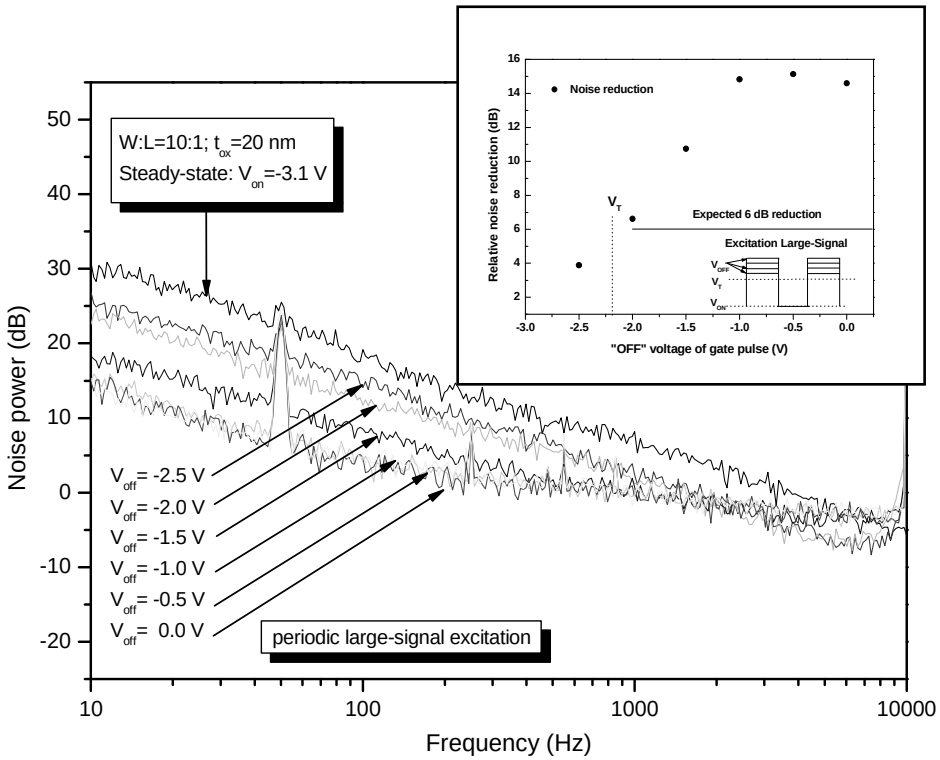

Figure 2.6 Noise PSD (dB) in a p-MOSFET by changing the 'off' voltage of the periodic large-signal with a 50% duty-cycle. α_H=6×10^{-4} for the steady-state spectrum. Also shown is the noise reduction (dB) (calculated at f=100 Hz) as a function of the 'off' voltage of the periodic large-signal and the expected 6 dB noise reduction for a 50% duty-cycle of the excitation signal.

under periodic large-signal excitation. The LF noise measurements on p-MOSFETs with smaller geometry (W:L=10:0.3), show a larger spread from device-to-device under similar biasing conditions, as compared to devices with larger geometry (W:L=10:1). Also, the LF noise PSD of the smaller devices is typically *not* $1/f$ in nature but rather a Lorentzian (Fig.2.5). Note that the slope of the LF noise PSD under periodic large-signal excitation is approximately $1/f$ rather than $1/f^2$.

Fig.2.6 shows the noise reduction obtained as a function of the 'off' value of the periodic large- signal. Also shown is the expected noise reduction, which is 6 dB below the DC biased value, because of the 50% duty cycle of the excitation signal. The noise reduction increases with increase in the 'off' value (beyond threshold) and then finally tends

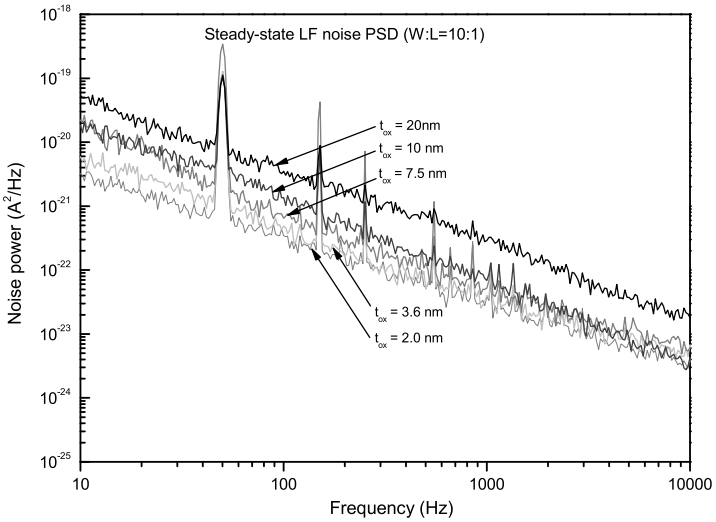

Figure 2.7 Steady-state LF noise PSD of p-MOSFETs (W:L=10:1) with varying t_{ox}. A fixed drain-current of 17 μA is forced through all the devices. LF noise PSD reduces as the gate-oxide are reduced.

to saturate, suggesting a limit to the amount of noise reduction that can be obtained as a result of periodic large-signal excitation. This is in accordance with the results presented in [40, 41], reporting increasing noise reduction closer to accumulation. However, with the differential setup we can obtain more detailed spectral information and over a wider band of frequencies. We see for instance a more or less flat plateau below the excitation frequency, which gradually changes to an noise spectrum with reduced power density at low frequencies.

Fig.2.7 shows the drain current noise spectral density of p-MOSFETs with different t_{ox} under steady-state (constant V_{GS}-V_T). A drain current of 17 μA, was forced through the transistors during the constant bias noise measurements. The LF noise PSD decreases with thinner gate-oxide thickness of the p-MOSFETs. The LF noise measured on the linear portion of the noise spectrum at 100 Hz and at 5 kHz is then plotted as a function of t_{ox} in Fig.2.8. For clean $1/f$ spectra there should be no difference in the slope of the noise power versus t_{ox} measured at 100 Hz or 5 kHz. In our case, this is not the case and the data points indicate that the noise power (S_{I_D}) has a power dependence of 0.37 and 0.9 on t_{ox} measured at 100 Hz and 5 kHz respectively.

The noise measurements under steady-state and under periodic large-signal excitation

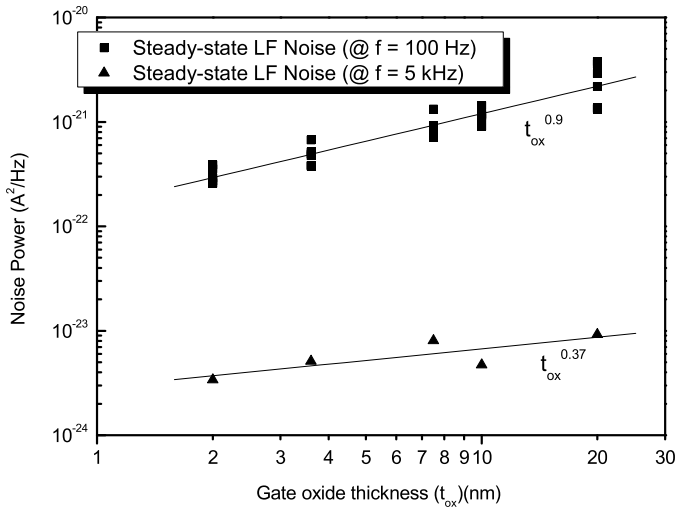

Figure 2.8 LF noise measured under steady-state on p-MOSFETs (W:L=10:1) with varying t_{ox} at f=100 Hz and f=5 kHz.

are also done on p-MOSFETs with a different geometry (W:L=10:0.3) and varying t_{ox}. During the noise measurements under periodic large-signal excitation on devices with different t_{ox}, the amplitude of the excitation signal is kept constant. The 'off' voltage of the excitation signal is kept in the region where the maximum possible noise reduction is observed. In Fig.2.9, the noise reduction obtain by periodic large-signal excitation is plotted against the LF noise under steady-state, for devices with different t_{ox}, similar to [44]. The number of points is the number of p-MOSFET devices measured. From the figure, we can identify two classes of devices. The first are the devices with a significant noise reduction (greater than 6 dB). These devices are the ones which also show a significantly high LF noise under steady-state. The second are the devices which show almost no significant noise reduction (6 dB or less). These are the devices which showed the least LF noise under steady-state. In general, we can infer that the larger the LF noise under steady-state, the larger was the noise reduction observed on that transistor under periodic large-signal excitation.

In Fig.2.10, the noise reduction obtained for each device is plotted against the t_{ox}. As seen from the figure, the noise reduction increases as the t_{ox} increases. This can also be understood from Fig.2.8, and Fig.2.9. The steady-state LF noise increases as the t_{ox} increases, and the noise reduction is larger when the steady-state LF noise is large. Thus combining these two results, we expect a larger noise reduction for devices with thicker

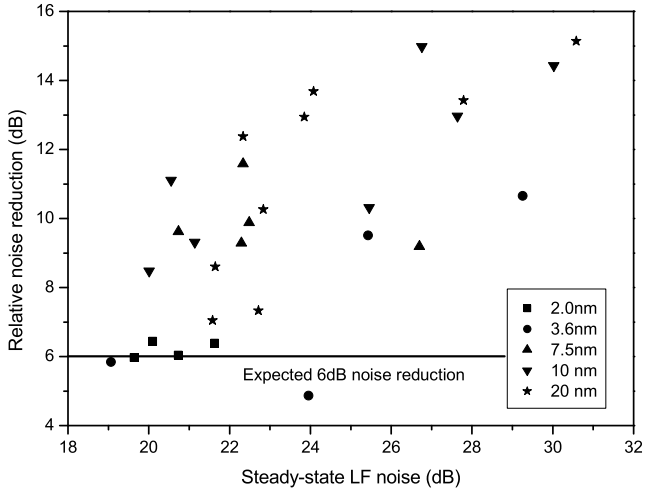

Figure 2.9 Noise reduction (dB) obtained by periodic large-signal excitation plotted as a function of the corresponding steady-state LF noise, for different p-MOSFETs with different t_{ox} (W:L=10:0.3).

t_{ox}. A similar trend is observed for transistors with geometry 10:1. Note that for most devices the noise reduction measured was greater than 6 dB, the expected noise reduction for a 50% duty cycle of excitation signal.

2.4 Discussion

The results of the LF noise measurements under steady-state and under periodic large-signal excitation on n-MOSFETs reported in [43,44] can be summarized as follows: periodic large-signal excitation, on average, results in a decrease in the noise of n-MOSFETs. In accordance with [40, 41], switching between inversion and accumulation results in a noise reduction that depends on the 'off' voltage. The noise reduction also occurs at high excitation frequencies up to 1 MHz. Different devices react differently to periodic large-signal excitation. Most devices show a decrease in LF noise, while some devices may show an increase in LF noise. The most noisy devices, those limiting circuit yield, show the largest decrease in noise under periodic large-signal excitation.

Our p-MOSFET LF noise measurements show similar behavior as the n-MOSFETs as can be seen from Figs.2.6, 2.9. The $1/f$ noise behavior in MOSFETs is explained

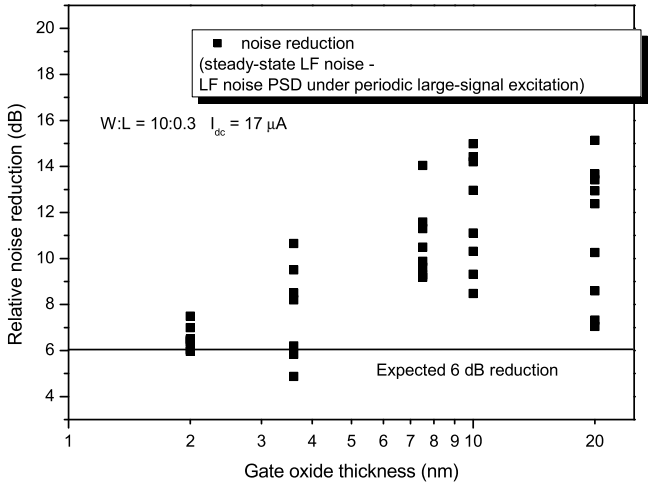

Figure 2.10 Noise reduction (dB) obtained by periodic large-signal excitation versus the gate oxide thickness for different p-MOSFETs (W:L=10:0.3).

by the mobility fluctuation model described by the Hooge parameter and the number fluctuation model based on the theory of trapping and de-trapping of charge carriers in traps located in the oxide or at the interface [13, 30]. The unified model for the flicker noise proposed by Hung *et al.* [31], incorporates both the number fluctuations and the surface mobility fluctuations. Defects at the interface or in the oxide, are trapping centers for charge carriers, which causes Random Telegraph Signals (RTS). The PSD of an RTS has a slope of $1/f^2$ [2]. With a proper distribution of the defects, it is possible to generate $1/f$ noise spectrum by the addition of the individual RTS spectra. The number of charge carriers (N) in the channel are an important parameter in determining whether RTS spectra dominates the $1/f$ noise of the MOSFET [30]. In our measurements, the large area p-MOSFETs typically had N$>1/10\alpha_H$ which is why the spectra was more $1/f$-like.

Our measurements on p-MOSFETs (Fig.2.5) with smaller gate area clearly indicate that the RTS spectra dominate the LF noise spectra as the number of carriers under the small gate area devices is low. In our measurements, the devices in which the RTS spectra dominated the LF noise spectra had N$<1/10\alpha_H$. The large spread in the LF noise of small geometry devices under similar biasing conditions is because in these devices the LF noise PSD are dominated by RTS spectra.

The decrease in the LF noise under periodic large-signal excitation can be explained

assuming that the LF noise in our devices is dominated by the noise due to the RTS (number-fluctuation model). When a transistor is periodically switched 'off', there is a high probability that the traps with energies located close to the Fermi level, are emptied, leading to a change in the occupancy of the traps. This change in the bias thus results in the change of mean capture and emission time constants of the trap, which in turn leads to a reduced noise spectrum. As the 'off' voltage goes deeper below the threshold voltage, more traps are emptied in the 'off' state. Thus, the noise reduction increases with increasing amplitude of the switching gate signal. The maximum noise reduction is reached, when all the traps involved in the trapping de-trapping process (which causes the LF noise under steady-state) are emptied during the 'off' state of the transistor. A further change in the 'off' voltage now has no effect on the noise spectrum.

Our LF noise measurements on p-MOSFETs with variable t_{ox} are consistent with that reported in [45]. S_{V_G}, the noise spectral density referred to the gate side, is given by $S_{V_G} = S_{I_D}/g_m{}^2$, where S_{I_D} is the drain current noise spectral density and g_m is the MOSFET transconductance. The empirical relation (Eqn.1.10) predicts a $t_{ox}{}^{0.5}$ dependence on S_{I_D}, in the saturation regime, for measurements done under constant current conditions. Our p-MOSFET measurement results show $t_{ox}{}^{p}$ dependence on S_{I_D} (p=0.37 @5 kHz, and p=0.9 @100 Hz) and thus $t_{ox}{}^{1+p}$ dependence on S_{V_G}. This indicates that in our noise spectrum, in the low-frequency region (100 Hz) the noise is more ΔN like, and near 5 kHz, the noise spectrum obeys the empirical relation, and thus $\Delta\mu$. This could indicate presence of ΔN related noise on top of bulk $1/f$ noise. Further, the noise measurement results under periodic large-signal excitation, gives a strong indication that the LF noise in our p-MOSFETs is dominated by the noise due to RTSs.

2.5 Conclusions

The p-MOSFET LF noise measurements under steady-state and under periodic large-signal excitation do not differ from the n-MOSFET noise measurements, thus suggesting a common source of origin for the low frequency noise in small geometry MOSFETs (n-type as well as p-type). In almost all cases, the LF noise reduction obtained for the p-MOSFETs, was more than 6 dB. The noise reduction increases with increasing 'off' value of switching gate voltage, and then tends to saturate. The larger the LF noise in a p-MOSFET, the larger was the noise reduction observed under periodic large-signal excitation. The influence of t_{ox} on p-MOSFET LF noise under steady-state indicates presence of ΔN related noise on top of bulk $1/f$ noise. Also, the fact that we get a LF noise reduction under periodic large-signal excitation, suggests that the source of origin for the low-frequency noise is due to the random trapping and de-trapping of charge carriers in the traps located in the oxide or at the interface.

Noise is a random phenomenon whose detailed study,
Needs pre-requisites of statistics and probability.
The Low-Frequency noise PSD of modern devices,
Are dominated by Lorentzians arising from RTSs..

The RTS Noise PSD as you may follow,
Doesn't completely distinguish between RTSs: fast and slow,
An RTS in the time-domain, incidentally,
Provides more information and is described completely.

Such an RTS under periodic large-signal excitation-
Exhibits noise power which is different and draws attention.
The RTS parameters under switched bias vary,
Making the RTS 'Cyclo-stationary' !!

3

RTS - Time Domain Analysis

WITH device scaling and emerging sub-micron CMOS technologies, the low frequency (LF) noise power spectral density (PSD) of MOSFETs is dominated by Lorentzians (explained later in the chapter), arising from Random Telegraph Signals (RTS). The need for accurately characterizing this RTS noise in devices fabricated in sub-micron CMOS processes is gaining importance. The physical origin of an RTS is attributed to the random trapping and de-trapping of mobile charge carriers in traps located at the Si-SiO_2 interface or in the silicon-dioxide. An RTS has two distinct levels and it switches between the two states at random moments. The RTS is observed in MOSFETs as a fluctuation in the drain current. The most common way for analyzing an RTS is measuring the averaged PSD using a spectrum analyzer. A pure two-level RTS is represented in the frequency domain by a Lorentzian spectrum [2].

RTS measurements on MOSFETs (both n-type and p-type) fabricated in modern CMOS processes are discussed in detail in this chapter. The main focus of this research is to investigate the RTS noise under large-signal excitation and we propose a RTS parameter extraction procedure in the time-domain to measure the RTS time-constants, under periodic large-signal excitation. The extracted RTS parameters were used in an analytical noise PSD expression, and compared with an RTS noise PSD measured by a spectrum analyzer. The technique of determining the statistical lifetimes and amplitudes of the RTS by fitting the signal level histogram of the time-domain record to two-gaussian histograms has been reported in literature [48]. This procedure was used for analyzing the 'noisy' RTS along with the device background noise, which turned out to be $1/f$ noise. The $1/f$ noise of the device can then be separated from the RTS using this procedure. To summarize, in this chapter, the emphasis is on measuring RTS in the *time-domain*, under both steady-state and periodic large-signal excitation.

This chapter is organized in the following manner. The first section is a review of random signals and their statistical analysis. The aim of this section is to provide the necessary background statistical information for analyzing the RTS. Next, the RTS noise PSD under steady-state and under periodic large-signal excitation is discussed. In the next section, the noise measurement setup is explained in detail. Also discussed are the steady-state and periodic large-signal excitation time-domain RTS measurements. This is followed by the various results from the spectral and time-domain noise measurements on RTSs. Finally, the chapter concludes with some discussions about the measurement results.

3.1 Statistical Analysis

Unwanted electrical signals arising from a variety of sources are classified as noise. A noise signal is unpredictable or random in nature. Any description of a noise (random) phenomenon is incomplete without a statistical analysis of the random signal. The following subsections on statistical analysis available in literature [52–55], provide the necessary framework or mathematical background to enable the detailed analysis of the MOSFET noise or RTS noise in particular. In this respect, we begin with the standard mathematical means of describing a purely random (stochastic) waveform. The reader who is familiar with the mathematics of statistical analysis can skip section 3.1.1 and continue from section 3.1.2. The next section discusses the RTS. This includes the probability distribution of the RTS and the PSD of the RTS. The final section deals with the cyclo-stationary RTS.

3.1.1 Random Processes

A random variable $X(s)$ maps the outcomes s of a chance experiment into numbers along the real line. A *random process* (also known as a *stochastic process*) maps outcomes into real *functions of time*. The collection of time functions is called an *ensemble*, and each member is called a *sample function*.

Fig.3.1 clarifies the concept of a random process. The basic premise regarding random processes is that the sample function being observed is not known. The value of the signal at time t_1 is completely random. In other words, $v(t_1,s)$ constitutes a *random variable*. Similarly the time slice at t_2 constitutes another random variable. A random process thus is a *family of random variables*.

Ensemble Averages and Correlation

A stochastic process is characterized by its average statistical properties. Consider a random variable X with possible values $x_1,x_2,x_3,....$, with probabilities of occurrence $P(x_1),P(x_2),P(x_3),....$ As the number of measurements N of X becomes very large, we observe the outcome $X = x_1$ occurring $NP(x_1)$ times, the outcome $X = x_2$ occurring $NP(x_2)$ times, etc. The *mean* or *average value* of all these measurements is the sum

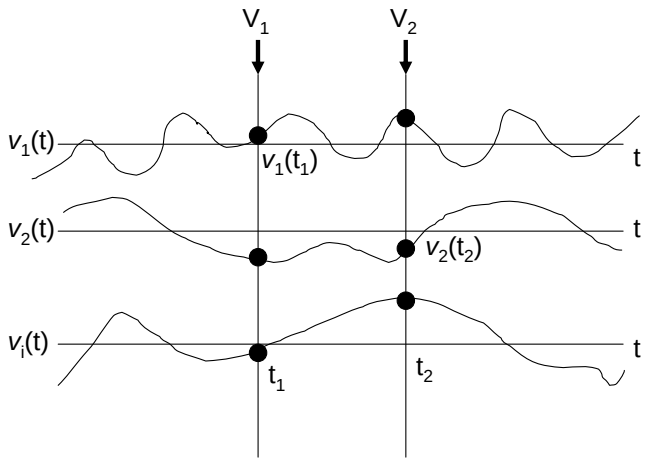

Figure 3.1 Noise (random) waveforms from an ensemble $v(t)$, as a function of time.

of these measurements divided by N. The *mean* (m) of the random variable X is called the *expectation* of X and is represented by $\bar{X}$ or $E(X)$.

$$\bar{X} \equiv E(X) = m = \sum_i x_i P(x_i) \tag{3.1}$$

For a continuous random variable the range of the variable is divided into small intervals Δx. The probability that X lies in the range x_i and $x_i + \Delta x$ is $P(x_i)$ and is equal to $f(x_i)\Delta x$. $f(x)$ represents the probability density function of the random variable. In the limit, as $\Delta x \to 0$, the summation in Eqn.3.1 is replaced by an integral.

$$m = \int_{-\infty}^{+\infty} x f(x) dx \tag{3.2}$$

The average represents the *first moment* of the random variable. In general, $E(X^n)$ is referred to as the n^{th} *moment* of the random variable X. If the random variable is a function of two random variables then the n^{th} *moment* of the random variable is given by

$$E(X^n, Y^n) = \int \int_{-\infty}^{+\infty} x^n y^n f_{XY}(x,y) dx dy \tag{3.3}$$

A useful statistical measure is the *variance* (σ^2) of the random variable. This is given by

$$\sigma^2 \equiv E[(X-m)^2] = \int_{-\infty}^{+\infty} (x-m)^2 f(x) dx \tag{3.4}$$

where, m is the mean of the random variable and $f(x)$ is the probability density function of the random variable. The *covariance* μ of two random variables X and Y is defined as

$$\mu \equiv E\{(X - m_x)(Y - m_y)\} \tag{3.5}$$

The covariance function measures the common variation of the random variables X and Y. It is the difference in $E[XY]$ and $E[X]E[Y]$. If the random variables X and Y are statistically independent then $E[XY]$ is equal to $E[X]E[Y]$ and the covariance is 0. The *autocorrelation* function of a random process $x(t)$ is defined as

$$R_X(\tau) = \lim_{T\to\infty} \frac{1}{2T} \int_{-T}^{+T} x(t)x(t+\tau)dt \tag{3.6}$$

The importance of the the above mentioned statistically parameters is evident when one relates the random variables to the electrical noise in circuits. The following are the relations between time averages and ensemble averages of a random signal:

- The mean value of the random signal m corresponds to the *DC component*.
- The mean squared value of the random variable m^2 equals the *DC power*.
- The mean square value equals the *total average power*.
- The variance (σ^2) equals the *AC power*, or the power in the time-varying component.
- The standard deviation (σ) equals the *rms value* of the time-varying component.

Gaussian density function and Central-limit theorem

The *gaussian* (also called *normal*) probability density function is of the greatest importance because many naturally occurring experiments are characterized by random variables with a gaussian density including noise in MOSFETs. A gaussian process is characterized by a gaussian probability density function. Furthermore, the importance of the the gaussian density function is evident from the *central-limit theorem*. The central-limit theorem for random variables indicates that the probability density of a sum of N independent random variables tends to approach a gaussian density as the number N increases. The mean and the variance of this gaussian density are the sum of the means and the sum of the variances of the N independent random variables. The theorem is valid even when the individual random variables are not gaussian.

In many engineering applications, the central-limit theorem (and hence gaussian density) plays an important role. The output of a linear system is a weighted sum of the input values, and if the input is a sequence of random variables, the output can be approximated by a gaussian distribution. More specifically, the total noise in the system can be modelled by a gaussian distribution.

Stationary and Ergodic Processes

A *stationary* random process is one whose characteristics remain invariant over all time. Stated in another way, any translation of the time origin along the ensemble does not in any way affect the values of the ensemble averages. For a stationary random process the joint statistics are independent of time shifts.

A random process is *ergodic* if every member of the process carries with it the complete statistics of the entire process. The ensemble averages will equal the appropriate time averages. A necessary condition for ergodicity is that the process must be stationary, but all stationary processes are not ergodic. If a random process is assumed to be an ergodic process, it leads to rather simple and intuitively meaningful relationships between statistical properties and time averages described earlier. Moreover, many of the random processes encountered in communication systems and electronics fit the ergodic model to a reasonable degree. Throughout this thesis we shall assume that the random signals (noise) come from ergodic sources.

Power and Energy of a Random Signal

Let $x(t)$ be a stationary random signal. An immediate consequence of stationarity is that $x(t)$ is a *power signal*, and the signal power

$$P_T(s) = \frac{1}{T}\int_{-T/2}^{+T/2} x^2(t)dt \tag{3.7}$$

is averaged over $-T/2 < t < T/2$. The total energy in $x(t)$ is

$$\lim_{T\to\infty} TP_T(s) = \int_{-\infty}^{+\infty} x^2(t)dt \tag{3.8}$$

If the energy is finite, $|x(t)| \to 0$ as $|t| \to \infty$, then the ensemble averages would differ for large values of t, contradicting the definition of stationarity. Hence the power (rather than the energy) of a random signal is an important parameter. Eqn.3.7 represents the power in a sample function out of an ensemble. Since the sample function is not known in advance, the *average power* defined as

$$\bar{P} = \lim_{T\to\infty} E[P_T(s)] \tag{3.9}$$

is used to express the power in a random signal. The notation $\bar{P}$ reflects the expectation operator $E[P_T(s)]$, which is performed after taking the limit $T \to \infty$ to ensure $\bar{P}$ exist. However, the order of time integration and expectation can be interchanged. Thus the average power $\bar{P}$ is the time averaging after ensemble averaging, $\langle E[x^2(t)]\rangle$ (angular brackets indicate time average).

Power Spectral Density and the Wiener-Khintchine theorem

A strictly periodic function can be expanded in a Fourier series. In the limit in which the period tends to infinity the series expansion is replaced by an integral. The Fourier transform and its inverse for a random signal $x(t)$ is given as follows:

$$X(\omega) = \int_{-\infty}^{+\infty} x(t) e^{-j\omega t} dt \tag{3.10}$$

$$x(t) = \frac{1}{2\pi} \int_{-\infty}^{+\infty} X(\omega) e^{j\omega t} d\omega \tag{3.11}$$

The Fourier transform thus acts like an operator between the time domain and the frequency domain. The Fourier transform is often useful in determining the spectral information contained in a signal. The energy in the signal can be obtained using Parseval's theorem.

$$\int_{-\infty}^{+\infty} [x_T(t)]^2 dt = \frac{1}{2\pi} \int_{-\infty}^{+\infty} |X_T(\omega)|^2 d\omega \tag{3.12}$$

The subscript T refers to the time interval in which the fluctuations are non-zero. The left-hand side of Eqn.3.12 represents the total energy in the random signal in the time-domain and the right-hand side in frequency domain. The average power is obtained by dividing Eqn.3.12 by T and taking the limit as $T \to \infty$ (See Eqn.3.9).

$$\lim_{T\to\infty} \frac{1}{T} \int_{-\infty}^{+\infty} [x_T(t)]^2 dt = \lim_{T\to\infty} \frac{1}{2\pi} \int_{0}^{\infty} \frac{2|X_T(\omega)|^2}{T} d\omega \tag{3.13}$$

Eqn.3.13 represents the average power in the random signal (both in time-domain as well as frequency domain). A closer look at the term $2|X_T(\omega)|^2/T$, shows that it has units of power per Hertz, which are the same units as that of the power spectral density (PSD). An ensemble average for this stochastic parameter is defined as the *power spectral density*.

$$S(\omega) = \lim_{T\to\infty} E[\frac{|2X_T(\omega)|^2}{T}] \tag{3.14}$$

The autocorrelation function is given by Eqn.3.6. Applying the Fourier transform to it leads us to the expression in Eqn.3.14. The Wiener-Khintchine theorem relates the autocorrelation function to the PSD of the random signal.

3.1.2 Probability Distribution of RTS

Waveforms used in data communication systems are modelled by a random sequence of pulses. A Random telegraph signal (RTS) is one such signal of interest. Our interest in RTS stems from the drain-current noise observed in the time-domain on small geometry MOSFETs. An RTS is basically a two-level signal. Assume the high-current state of the RTS to be state 1 and the low-current state to be state 0. The probability of transition from state 1 to state 0 is given by $1/\overline{\tau_1}$, and $1/\overline{\tau_0}$ is the probability of transition from 0 to 1. These set of conditions define an RTS.

Let $p_1(t)$ be the probability that the state 1 will not make a transition for time t and one transition in time interval t and $t+dt$. Also, let $P_{11}(t)$ be the probability of remaining in state 1 and not making a transition for time t. We know that the probability of making a transition from 1 to 0 at time t is $1/\overline{\tau_1}$ from definition. Thus we get

$$p_1(t) = P_{11}(t)/\bar{\tau_1} \tag{3.15}$$

In addition, $P_{11}(t+dt)$ is the probability of remaining in state 1 in time $t+dt$, which is equal to remaining in state 1 in time t ($P_{11}(t)$), and the probability of not making a transition from 1 to 0 in time dt (1-$dt/\bar{\tau_1}$).

$$P_{11}(t+dt) = P_{11}(t)(1-dt/\bar{\tau_1}) \tag{3.16}$$

Rearranging Eqn.3.16 we get

$$\frac{dP_{11}}{dt} = -\frac{P_{11}(t)}{\bar{\tau_1}} \tag{3.17}$$

Integrating and solving we get

$$P_{11}(t) = exp(-t/\bar{\tau_1}) \tag{3.18}$$

Substituting $P_{11}(0) = 1$ we get

$$p_1(t) = \frac{1}{\bar{\tau_1}} exp(-t/\bar{\tau_1}) \tag{3.19}$$

Similar expressions hold for state 0. Thus, using the probability of transition from state 1(0) to 0(1) as a single rate, we can prove the times in state 1(0) are exponentially distributed. The mean time spent in the state 1(0) is

$$m \equiv \int_0^\infty t\, p_1(t) dt = \bar{\tau_1} \tag{3.20}$$

The standard deviation is

$$\sigma \equiv [\int_0^\infty t^2 p_1(t) dt - \bar{\tau_1}^2]^{1/2} = \bar{\tau_1} \tag{3.21}$$

The standard deviation is equal to the mean time spent in either state of the RTS, which is a normal result for poisson statistics. This result is extremely important and will be used later on in this chapter for verifying our RTS time-domain measurements.

3.1.3 Power Spectral Density (PSD) of RTS

The PSD of an RTS can be derived from the amplitude (ΔI) and the mean-time spent in the high state ($\bar{\tau_1}$) and the mean-time spent in the low state ($\bar{\tau_0}$) [2]. The amplitude of the RTS (ΔI) is defined as the difference between the levels in the 'high' state and in the 'low' state.

Assume that all statistical properties are independent of the time origin and the random process is stationary. The RTS can be in one of the two states 0 or 1. From the definition of an RTS, the probability of making a transition to 0 in a short time dt given that we are

in state 1 is $dt/\bar{\tau}_1$. Similarly, the probability of making a transition to 1 in a short time dt given that we are in state 0 is $dt/\bar{\tau}_0$. Thus the mean-time spent in state 1 is $\bar{\tau}_1$ and mean-time spent in state 0 is $\bar{\tau}_0$ (Eqn.3.20). The probability of being in state 1 is thus $\bar{\tau}_1/(\bar{\tau}_1+\bar{\tau}_0)$, and for state 0 is $\bar{\tau}_0/(\bar{\tau}_1+\bar{\tau}_0)$.

Determining the autocorrelation is the first step towards calculating the PSD of an RTS. The autocorrelation of an RTS is given by (Eqn.3.6)

$$\begin{aligned} R_X(s) &= \langle x(t)x(t+s)\rangle \\ &= \sum_{ij} x_i x_j [\text{Prob. that } x(t)=x_i][\text{Prob. that } x(t+\tau)=x_j; \text{ given that } x(t)=x_i] \end{aligned} \tag{3.22}$$

Choosing one state of the RTS as '0' leads to three terms of the expression being 0. Thus we get

$$\begin{aligned} R_X(s) &= (\Delta I)^2[\text{Prob. that } x(t)=1][\text{Prob. of no transitions in time } \tau; \text{ starting in state 1}] \\ &= (\Delta I)^2 \frac{\bar{\tau}_1}{(\bar{\tau}_1+\bar{\tau}_0)} P_{11}(s) \end{aligned} \tag{3.23}$$

From the earlier section and Eqn.3.15 the probability of being in state 1 is (P_{11}). The differential equation for P_{11} is as follows. For a small increment dt we get

$$P_{11}(t+dt) = P_{10}(t)\frac{dt}{\bar{\tau}_0} + P_{11}(t)(1-\frac{dt}{\bar{\tau}_1}) \tag{3.24}$$

The probability $P_{11}(t+dt)$ of being in state 1 in time $t+dt$, is the sum of the probabilities of two mutually exclusive events:

- probability of being in the state 0 in time t, (P_{10}) and one transition (0 to 1) in dt, $(dt/\bar{\tau}_0)$,
- probability of being in the state 1 in time t, (P_{11}) and no transition in dt, $(1-dt/\bar{\tau}_1)$,

We also have,

$$P_{11}(t)+P_{10}(t) = 1 \tag{3.25}$$

In the limit that $dt \to 0$, from 3.24 and 3.25, and eliminating $P_{10}(t)$, we obtain a differential equation

$$\frac{dP_{11}}{dt} + (\frac{1}{\bar{\tau}_1}+\frac{1}{\bar{\tau}_0})P_{11}(t) = \frac{1}{\bar{\tau}_0} \tag{3.26}$$

Solving Eqn.3.26 we get

$$P_{11}(t) = \frac{\bar{\tau}_1}{\bar{\tau}_1+\bar{\tau}_0} + \frac{\bar{\tau}_0}{\bar{\tau}_1+\bar{\tau}_0} exp[-t(\frac{1}{\bar{\tau}_1}+\frac{1}{\bar{\tau}_0})] \tag{3.27}$$

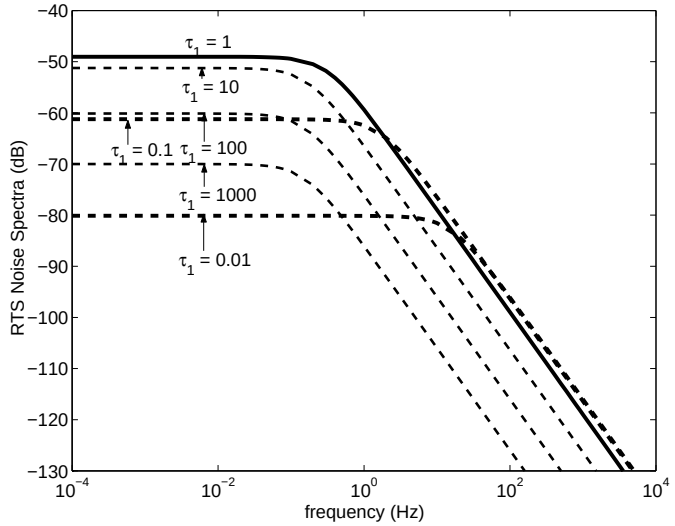

Figure 3.2 RTS Noise Spectra for different values of $\bar{\tau_1}/\bar{\tau_0}$ using Eqn.3.28 ($\bar{\tau_0} = 1s$). The nature of the RTS spectrum is a Lorentzian, comprising of a flat part and a 20 dB/decade roll off.

Substituting Eqn.3.27 in Eqn.3.23 we get the autocorrelation function of the RTS. Further, applying the fourier transform to the autocorrelation to get the PSD (Weiner-Khintchine theorem) we get

$$S(f) = \frac{4(\Delta I)^2}{(\bar{\tau_1} + \bar{\tau_0})[(1/\bar{\tau_0} + 1/\bar{\tau_1})^2 + (2\pi f)^2]} \tag{3.28}$$

The PSD of an RTS is thus a function of the RTS amplitude (ΔI), and the mean-time spent in the high and low states, ($\bar{\tau_1}, \bar{\tau_0}$). Another important result is the total average power ($\bar{P}$) in the the RTS. This is obtained by integrating Eqn.3.28 over the entire frequency range.

$$\bar{P} = \frac{\Delta I^2}{(\bar{\tau_1} + \bar{\tau_0})(1/\bar{\tau_0} + 1/\bar{\tau_1})} \tag{3.29}$$

Fig.3.2 uses Eqn.3.28 to plot the PSD of an RTS for ΔI= 5 mA, $\bar{\tau_0} = 1s$, and $\bar{\tau_1}$ varying from 0.01 s to 1000 s. The units of PSD are dB A^2/Hz. The RTS spectra is a characteristic Lorentzian spectra. This consists of a flat part for frequencies lower than the corner frequency of the RTS ($f_o = 1/2\pi(1/\bar{\tau_0} + 1/\bar{\tau_1})$), and a 20 dB/decade roll off for frequencies beyond f_o.

The power in the RTS is given by Eqn.3.29 and is plotted in Fig.3.3 as a function of the ratio of the RTS time-constants. The maximum power occurs when the ratio of the RTS time constants is unity. The noise power reduces as the ratio of $\bar{\tau_1}/\bar{\tau_0}$ changes. Fig.3.3 is

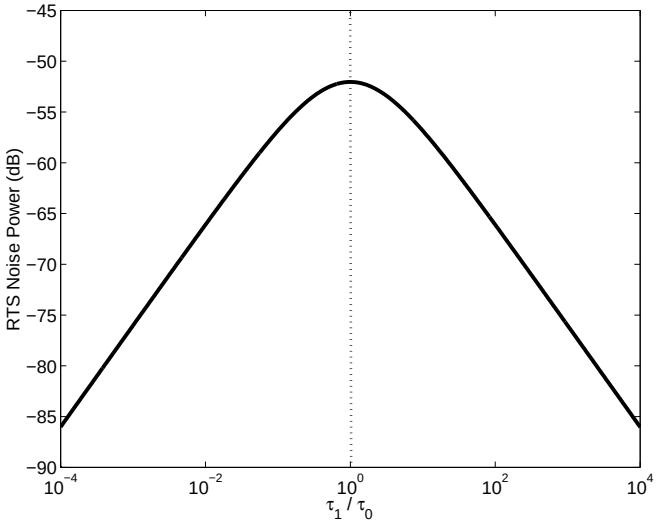

Figure 3.3 RTS Noise power for different values of $\overline{\tau_1}/\overline{\tau_0}$ using Eqn.3.29 ($\overline{\tau_0} = 1s$). It can be clearly seen that the noise power reaches its maximum when the ratio is 1.

important in the context of the study of the decrease in the RTS noise in MOSFETs under large-signal excitation, as it gives the relation between the RTS noise power as a function of changing RTS time-constants.

3.1.4 Cyclo-stationary RTS

Circuits with time-varying operating points can cause the stochastic averages that describe the noise to vary with time. If they vary in a periodic fashion, the noise is said to have cyclo-stationary properties, and the ensemble averages referred to as being cyclo-stationary [54,56]. Cyclo-stationarity occurs when the time-varying operating point modulates the noise generated by bias-dependent noise sources or when the time-varying circuit modulates the transfer function from the noise source to the output. As suggested by the name, modulated noise sources can be modelled by modulating the output of stationary noise sources. In Fig.3.4, the stationary noise with an arbitrary PSD is modulated by a periodic signal (square wave). This is representative of both ways in which cyclo-stationary noise is generated (modulated noise sources and modulated signal paths). Modulation can be interpreted as multiplication in the time domain or convolution in the frequency domain. Thus, the modulation by a periodic signal causes the noise to mix up and down in multiples of the modulation frequency in a process that is often referred to as noise folding. Noise from the source at a particular frequency f is replicated and copies appear at $f \pm k f_0$, where k is an integer and f_0 is the excitation frequency of the periodic

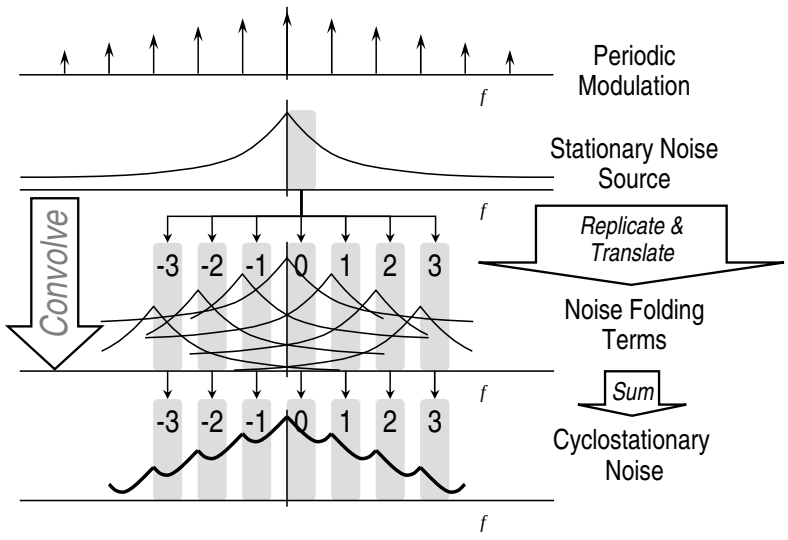

Figure 3.4 Noise which is modulated by large-signal excitation (f_o). The noise is replicated and translated by each harmonic of the excitation frequency, resulting in correlations at frequencies separated by kf_0.

signal. Conversely, noise at the output at a particular frequency f has contributions from noise from the sources at frequencies $f \pm kf_0$.

The conventional spectrum analyzer measures the time-average PSD. Since the analyzer has a very small effective input bandwidth, it ignores correlations in the noise and so ignores the cyclo-stationary nature of the noise (assuming that the frequency of the cyclo-stationarity is much higher than the bandwidth of the analyzer). Using the spectrum along with information about the correlations in the noise between sidebands gives a complete description of the cyclo-stationary noise. If a stage that generates cyclo-stationary noise is followed by a filter whose passband is constrained to a single sideband (the passband does not contain a harmonic and has a bandwidth of less than $f_0/2$, where f_0 is the fundamental frequency of the cyclo-stationarity), then the output of the filter will be stationary. This is true because noise at any frequency f_1 is uncorrelated with noise at any other frequency f_2 as long as both f_1 and f_2 are within the passband.

Consider the case when the RTS noise in a MOSFET is modulated by periodically switching 'off' the MOSFET by applying a large-signal (square wave) at the gate with an excitation frequency higher than the corner frequency of the RTS (See Fig.3.5). The 'noisy' state corresponds to the state when the gate potential is above the threshold voltage of the MOSFET, and a 'noiseless' state corresponds to the state when the MOSFET is 'off' and there is no current. The noise under such excitation is cyclo-stationary RTS

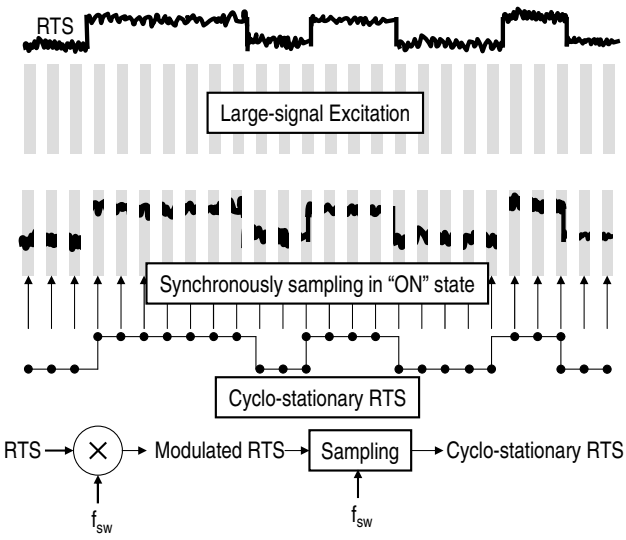

Figure 3.5 RTS in steady-state and periodic large-signal excitation. Sampling during the 'on' states and joining them together gives a cyclo-stationary RTS. The 'on' state is indicated by the shaded part and the white part indicates the device 'off' state. RTS is visible only in the shaded part ('on' state).

noise. Compare this to a case when the MOSFET is always 'on' with the 'on' level being the same as that used when the MOSFET is periodically switched 'off'. The constant gate-bias corresponds to the steady-state condition and the noise is the steady-state stationary RTS noise. The cyclo-stationary RTS noise has information about the 'off' state in addition to the 'on' state noise. Due to the narrow bandwidth and the asynchronous sampling, the spectral analyzer clearly outlines the difference in the PSD between the steady-state RTS noise and the cyclo-stationary RTS noise. For a 50% duty-cycle of the applied large-signal, the cyclo-stationary RTS PSD is 6 dB below the steady-state RTS PSD (see chapter 2). If the modulated RTS noise is then sampled synchronously during the 'on' states, in the time-domain the result is a cyclo-stationary RTS without the 'off' state information (See Fig.3.5). It would appear, that this synchronously sampled cyclo-stationary RTS is similar to the steady-state RTS, because the 'off' state information is no longer present. This would indeed be the case if the only correlation present was between the 'on' states and no correlation between the 'off' states and the 'on' states. On the other hand, if the synchronously sampled cyclo-stationary RTS is different from the steady-state RTS, then the effect of periodically switching 'off' the MOSFET changes the correlation between the 'on' states.

3.2 RTS Measurements in Time Domain

Our LF noise measurements described in *chapter 2* of this thesis have been in the frequency domain. As seen from the earlier section, the PSD does not describe the RTS completely. The spectral measurements provide only the value of the corner frequency, the frequency above which the spectral density rolls off as f^{-2} and does not give the average lifetimes in the individual states, but only the harmonic mean of these two characteristic time constants. A time domain measurement can be useful in extracting all the RTS parameters. From *chapter 2* we have seen that our LF noise measurements are dominated by RTS. Thus in order to get a complete understanding of the LF noise, our RTS measurements are characterized in the time-domain.

The standard procedure for the analysis of RTS in time domain consists of directly finding from the time record the time instances at which the signal is in the distinct state. Using a simple level-crossing algorithm one can then determine the instances of the 'high' and 'low' states of the RTS [57, 58]. In this section we discuss our procedure to extract the mean 'high' and mean 'low' ($\overline{\tau_1}, \overline{\tau_0}$) and the RTS amplitude in the time-domain, for devices under steady-state and periodic large-signal excitation conditions. The RTS parameters (extracted from the time domain) are then used in analytical RTS noise PSD expression [2] and matched with the noise PSD measured from a spectrum analyzer. This simple procedure can be used effectively for a clean RTS, where the ratio of the RTS amplitude to background noise is high. Another procedure for analyzing RTS in the time domain is based on the analysis of the signal level histogram of the measured signal and the separation of the data points into two records each corresponding to one of the RTS levels [48]. Using this procedure it is possible to separate the RTS from the background noise.

3.2.1 Experimental Details

The measurement setup used for the time-domain noise measurements is the same as that used for the spectral noise measurements (described in *chapter 2*) [47, 57]. A digital oscilloscope (TDS7404) is used for recording the time-domain RTS data. Large time frames of the RTS are obtained in an automated manner using LabVIEW and TekVISA. The spectral analyzer is used to measures the drain current noise PSD of the device under test (dB A^2/Hz). Under periodic large-signal excitation the device is periodically switched 'off', by applying a square wave with a 50 % duty cycle at the gate of the device. The excitation frequency is f_{sw}=10 kHz, which is much higher than the RTS corner frequency. The RTS under periodic large-signal excitation results in a modulated RTS which is further sampled only in the 'on' state of the MOSFET. These 'on' states are then joined together to form a cyclo-stationary RTS. Fig.3.5, shows a schematic of the cyclo-stationary RTS. The measurement setup, along with the RTS parameter extraction procedure, can be used successfully to extract the RTS parameters under steady-state and under periodic large-signal excitation. The extracted parameters are then used in Machlup's analytical PSD expression [2], and compared with the noise PSD measured using a spectrum analyzer.

RTS on both p-MOSFET and n-MOSFET were used in this study of RTS. The p-

MOSFETs have a geometry of W:L=10:0.3, with t_{ox} of 10 nm. The n-MOSFETs are from a CMOS 0.18 μm process flow, with a W:L=1:0.13, and t_{ox} of 7 nm. The devices selected for the RTS measurements are such that they exhibit a single dominant RTS. The selection of the devices, thus precludes problems of multi-level RTS and multi RTS occurring in the device. All our measurements were carried out at room temperature.

3.2.2 RTS Parameter Extraction

Large time frames (1 minute) of the RTS are obtained in an automated setup, using the digital oscilloscope (TDS7404), LabVIEW and TekVISA. For accurately extracting the RTS time parameters, the time-domain measurement should contain at least 200 transitions. In order to not miss a transition (which would lead to an error in the RTS parameters) the sampling frequency of the digital oscilloscope should be at least 100 times higher than the RTS corner frequency ($f_{sw} > f_o$) [58]. The use of an anti-alias filter before sampling precludes problems of aliasing (as the name suggests). The cut-off frequency of the low-pass anti-alias filter should be half the sampling frequency. Under certain modes of operation, anti-aliasing is done in the digital oscilloscope itself. RTS time-domain measurements done with and without using an anti-aliasing filter indicate that the effect of aliasing in the low-frequency region of our interest is not significant.

The very low-frequency drift in the measured data and the high frequency noise is filtered out using software filters (MATLAB). This is done in order to get a clear level to distinguish data points and separate them into two records, the 'high' state and the 'low' state. The passband of the filters used is selected such that the corner frequency of the RTS under study is always within the passband. A simple level-crossing algorithm then determines the times spent by the RTS data points in the high-state and in the low-state. The mean high and low times ($\overline{\tau_1}, \overline{\tau_0}$) thus can be determined.

In order to extract the RTS parameters when the RTS-to-background noise ratio is low, the method outlined in Fig.3.6 is used. A clean RTS is extracted from the noisy RTS, using the time derivative and a threshold level to detect a valid transition, (schematically shown in Fig.3.6), from which the RTS parameters are then extracted.

Verification of the extracted RTS parameters is an important step before doing further analysis. Along with the time-domain measurements, the spectrum analyzer is used to measure the RTS PSD. The extracted RTS parameters are used in the Machlup expression and compared with the measured PSD. As seen from the earlier statistical analysis, the mean and standard deviation are equal for an RTS. The distributions of the times in the 'high' and 'low' states are exponential. This implies that the histogram of the 'high' and the 'low' states is an exponential decay. Both these serve as additional verifying tools in our RTS parameter extraction.

3.2.3 Separation of RTS and Background noise

The procedure for analyzing the background noise and the RTS is based on the analysis of the signal-level histogram of the measured signal and the separation of the data

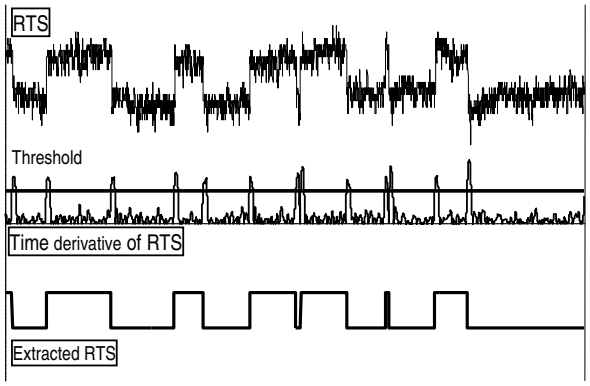

Figure 3.6 Useful transitions in the noisy RTS data can be detected by calculating the time derivative of the RTS, and comparing it to a noise threshold level. The clean RTS is then constructed from these transitions.

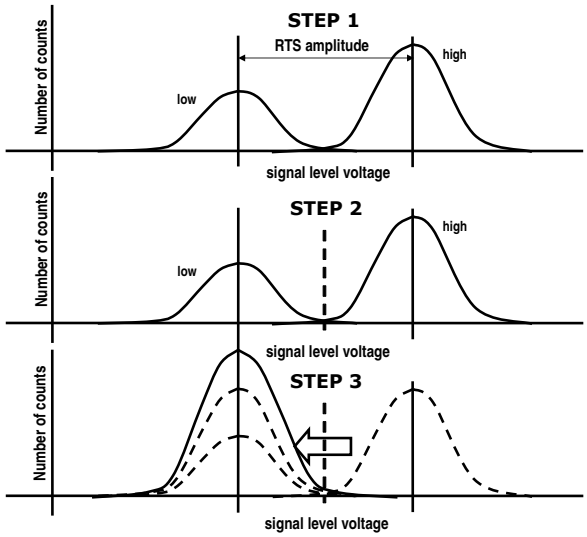

Figure 3.7 Procedure for separating the background noise from the RTS. The RTS amplitude is subtracted from the 'high' state to give the background noise.

points into two sub-records each belonging to an RTS level [48, 49]. The procedure assumes that the RTS is a two-level signal, whose amplitude distribution is characterized

Figure 3.8 An RTS observed on a p-MOSFET, V_{GS} =-1.1 V, V_{DS} =0.2 V (Arbitrary units along the X and Y axis). Note the distinction in the RTS level and the device background noise.

by two peaks each denoting the RTS level. The procedure assumes that the distributions of the experimentally measured signal amplitudes around each peak are due to Gaussian noise. The separation of the background noise from the distinct two level RTS is then a three step process. Fig.3.7, explains the procedure for separating background noise from the RTS.

The first step is to build the signal level histogram of the time domain signal. This can be fitted with two Gaussian distributions, the peak of each corresponding to the 'high' and 'low' level voltage amplitude of the RTS. The amplitude of the RTS can thus be determined.

The second step is to determine the separation level (amplitude) which separates the data points into two distinct sub-records corresponding to the two levels. In our setup this separation level was determined intuitively. A more detailed analysis of this separation procedure is available in literature [49], from which it is also possible to estimate the error made in the separation.

Finally, the third step is to subtract the RTS amplitude difference between the two RTS levels (obtained from step 1) from the data points in the 'high' state, thus obtaining a noisy signal without RTS jumps. This completes the background noise and RTS separation procedure. The power spectrum of each can then be calculated using an *Fast Fourier Transform* (FFT) to determine the noise power due to the RTS and the noise power due to the background noise, both for the constant bias and the periodic large-signal excitation conditions.

3.3 RTS measurement results

Fig.3.8 shows a sample of a time-domain RTS obtained from the drain current measurement under constant bias on a p-MOSFET, V_{GS}=-1.1 V, V_{DS}=0.2 V (Arbitrary units along the X and Y axis). Note the distinction in the RTS level and the device background noise (which is the noisy part present in the 'high' and 'low' states). The devices selected for the measurement show a clear RTS on top of background noise. The background noise is observed to be well above the noise floor of the measurement setup.

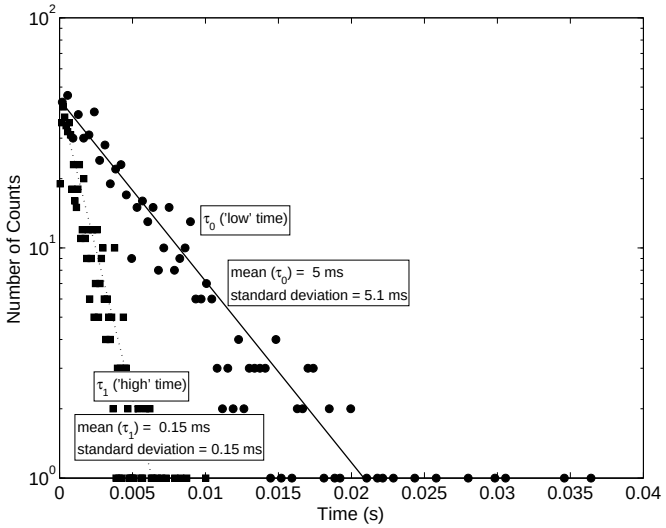

Figure 3.9 Steady-state RTS parameter extraction of time-constants. The statistical distribution of the times in the 'high' and 'low' states. The markers indicate the times in the RTS state and the lines are the best fit.

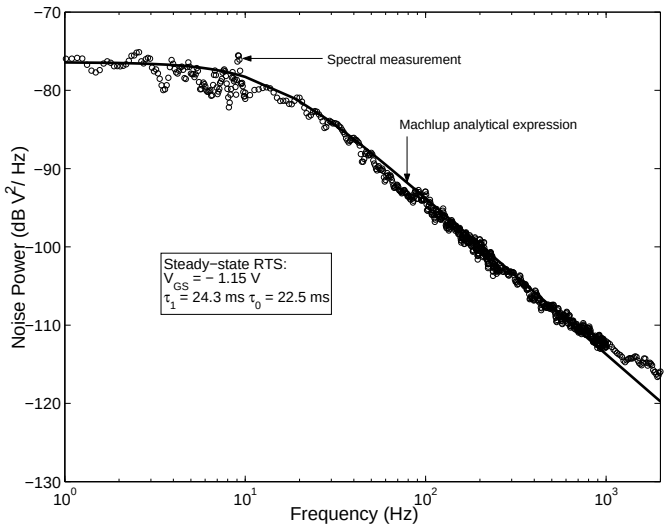

Figure 3.10 RTS Noise PSD measured (spectrum analyzer) and calculated (analytical expression and parameter extraction) under steady-state conditions. V_{GS} = -1.15 V, V_{DS} = 2.0 V; $V_T \approx$ -1.0 V.

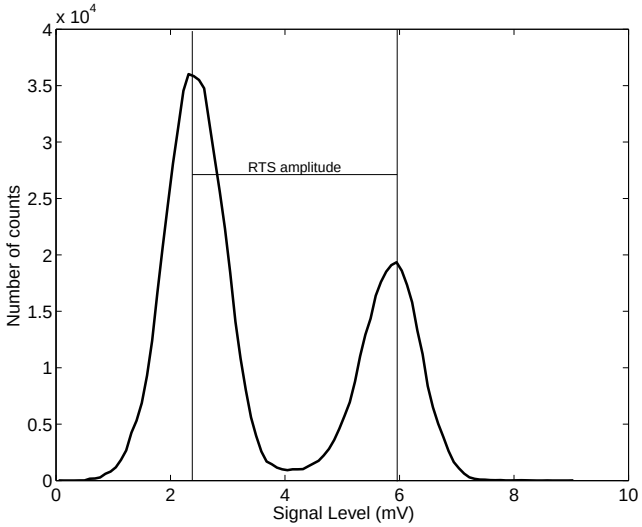

Figure 3.11 Signal-level histogram of an RTS observed in a MOSFET in the steady-state. The data points are grouped into two distinct levels corresponding to the RTS level.

3.3.1 RTS in Steady-state

Under steady-state conditions, the MOSFET is under a constant bias. Fig.3.9 shows the statistical distribution of the times in the 'high' and 'low' state of the RTS. The 'high' and the 'low' times are distributed exponentially, which is in agreement with the RTS theory described earlier in section 3.1.2. The mean and the standard-deviation are equal, thus validating our RTS parameter extraction technique.

Fig.3.10 shows the noise power spectra of an RTS under constant bias (steady-state) measured by a spectrum analyzer. Also shown is the noise PSD calculated using the analytical expression for an RTS [2]. The mean 'high' and 'low' times and the RTS amplitude are extracted from the time-domain measurements described earlier. From Fig.3.10, we see that the analytical expression matches quite well with the spectral result, thus validating our RTS parameter extraction technique even further.

3.3.2 Separating RTS and 1/f

The procedure to separate the RTS from the background noise is employed to obtain the device background noise. The PSD of this data is the device background noise power. The first step of the noise separation procedure is shown in Fig.3.11 for a device in steady-state. Fig.3.11 shows two distinct peaks each corresponding to the RTS level surrounded by the device background noise with a gaussian distribution. The data points are then

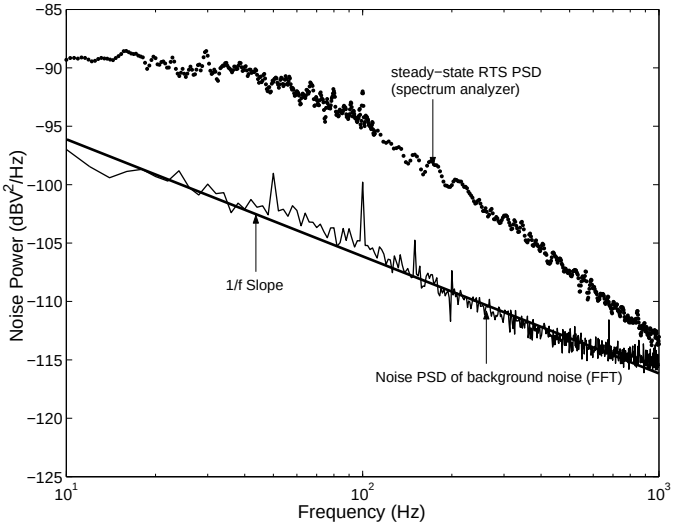

Figure 3.12 The PSD of an RTS in steady-state measured on a p-MOSFET with W:L=10:0.3, $V_T \approx$ -0.9 V, V_{GS} = -1.1 V, using a spectrum analyzer. Also shown is the computed PSD of the device background noise and the $1/f$ slope ($\alpha_H = 6.8\times 10^{-6}$).

grouped into two levels. The RTS amplitude (difference between the two gaussian peaks) is then subtracted from the 'high' level to give the device background noise data. The PSD of the device background noise is then calculated, using an FFT routine. Fig.3.12 shows the PSD of an RTS measured in steady-state using a spectrum analyzer. Also shown is the computed PSD of the device background noise extracted using the above procedure. A line with a slope of $1/f$ (10 dB/decade) is then fitted to the PSD of the device background noise. From Fig.3.12, it can be seen that the slope of the noise is $1/f$. Relating this to the $1/f$ noise in MOSFETs, the Hooge parameter for the extracted $1/f$ background noise was then calculated to be $\alpha_H = 6.8\times 10^{-6}$ which was found to be in accordance to values reported in literature [30].

3.3.3 RTS under Large-signal Excitation

The cyclo-stationary RTS is obtained after sampling the modulated RTS (see Fig.3.5). Aliasing issues were precluded by filtering the modulated RTS data in software, before sampling the 'on' periods to form the cyclo-stationary RTS. The next step was to test if this cyclo-stationary RTS obeyed the properties of an RTS in steady-state. Fig.3.13 shows the statistical distributions of the times in the 'high' and 'low' state of such a cyclo-stationary RTS. The mean-times were indeed distributed exponentially and the mean and standard deviation were found to be equal. This indicates that the cyclo-stationary RTS

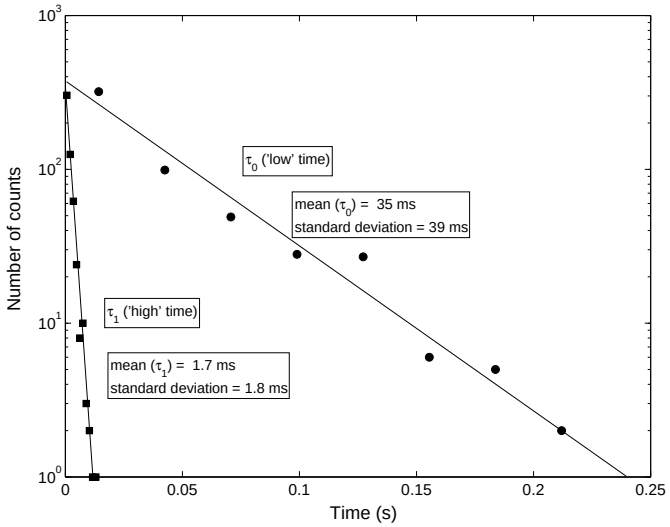

Figure 3.13 Cyclo-stationary RTS parameter extraction of time-constants. The histogram of the times in the 'high' and 'low' states. The distribution is exponential and the mean and the standard-deviation are equal.

has statistical properties similar to the steady-state RTS.

Fig.3.14 shows the measured PSD of an RTS under periodic large-signal excitation (W:L=10:0.3, V_T=-0.9 V, V_{GS} is switched between -1.1 V and 0 V). The frequency of excitation was 10 kHz with a duty-cycle of 50%. Also shown are the calculated PSD of this cyclo-stationary RTS and the device $1/f$ noise. The calculated PSD of the cyclo-stationary RTS is 6 dB higher than the measured PSD. This is because the cyclo-stationary RTS is obtained only by synchronously sampling the 'on' states of device. The measured PSD, on the other hand is got by sampling both the 'on' and 'off' states of the device with a narrow bandwidth. The PSD of the device background noise under periodic large-signal excitation is also fitted with a line of slope $1/f$ (10 dB/decade). From Fig.3.14 it can be seen that the device background noise for the periodic large-signal excitation case is also $1/f$ in nature.

Fig.3.15 shows noise PSD of an RTS in steady-state and under periodic large-signal excitation. Also shown is the noise PSD calculated using Machlup's analytical expression for an RTS [2]. The mean 'high' and 'low' times and the RTS amplitude were extracted from the time-domain measurements. From Fig.3.15 we see that the analytical expression matches the spectral result quite well, thus validating our RTS parameter extraction technique. Of particular interest is the cyclo-stationary RTS, where the analytical expression matches the spectral measurement in the low-frequency region below the switching

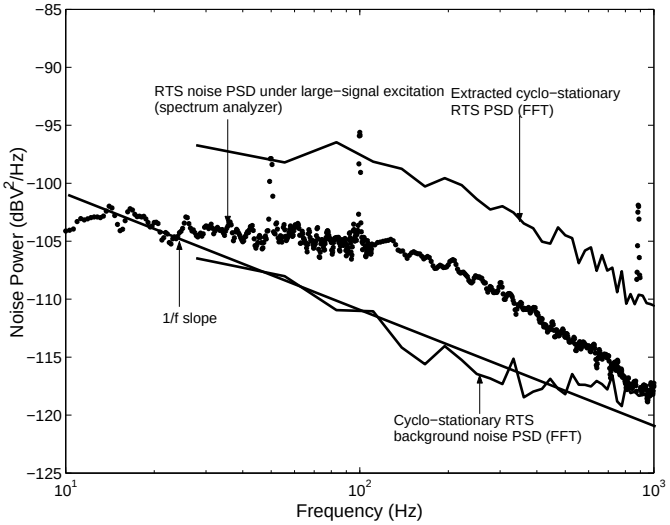

Figure 3.14 The measured PSD of an RTS under periodic large-signal excitation for a p-MOSFET with W:L=10:0.3, $V_T \approx$ -0.9 V. V_{GS} is switched between -1.1 V and 0 V, f_{sw} = 10 kHz, Duty-cycle=50%. Also shown are the calculated PSD of the cyclo-stationary RTS (6 dB above the measured PSD) and the device background noise.

frequency. It can also be seen that the time-constants of the cyclo-stationary RTS are different as compared to the time-constants for the steady-state RTS. It is this difference which leads also leads to a different noise PSD.

3.4 Discussions

Using our measurement results in the time-domain, we were able to fully characterize the cyclo-stationary RTS. Although, it can be mathematically proven that the cyclo-stationary RTS should have statistical properties similar to the steady-state RTS, we performed measurements to verify that this was indeed true. The exponential distribution of the cyclo-stationary RTS, together with Machlup's expression and the spectral measurements, drive home this point.

The cyclo-stationary RTS obtained from sampling the modulated RTS or RTS under periodic excitation, does not have information of the 'off' state (due to sub-sampling). But this information is not important in the context of analyzing the noise behavior as there is no noise in the 'off'state. The complete behavior (RTS under large-signal excitation) can be modelled by determining the PSD of the cyclo-stationary RTS and supplementing it by the noise in the 'off' state (In our case this was a 6 dB noise reduction, as the applied large-

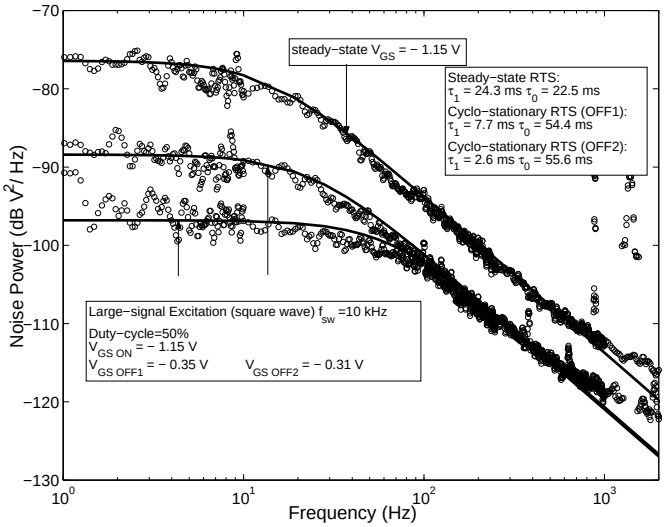

Figure 3.15 Measured noise PSD (spectrum analyzer), and calculated noise PSD (Machlup's analytical PSD expression and parameter extraction) for an RTS in steady-state and under periodic large-signal excitation (cyclo-stationary RTS).

signal excitation had a duty-cycle of 50%). This can be easily verified by matching our results with the spectral results as the PSD from the spectrum analyzer has the complete information.

As discussed in the statistical analysis section, if the correlation between the data points in the 'off' and 'on' states of a signal under periodic large-signal excitation was zero, sampling the 'on' states only would yield in a signal exactly similar to the signal in the steady-state. In the context of our RTS measurements, the RTS (or noise) under steady-state would be unchanged after periodically turning the MOSFET 'off' by a large-signal. But our measurements show that the noise is changed under large-signal excitation. This is a strong indication that there is a correlation between the 'off' state and 'on' state, or putting it simply, the signal in the 'on' state has some bias history. Our measurements also show that the cyclo-stationary RTS time-constants are different from the steady-state RTS time-constants and also that these time-constants are a function of the biasing conditions in the 'off' state of the device. This is why the noise under periodic large-signal excitation is different from the noise in steady-state after accounting for the 'off' state noise.

The results of the time-domain separation method verify the assumption of the dominating two-level RTS on top of the $1/f$ noise in MOSFETs. In our noise measurements, an RTS was observed when N$<1/10\alpha_H$ (N being the number of carriers). Also the PSD

of the device background noise is $1/f$ in nature for both the steady-state RTS and the cyclo-stationary RTS. The extracted Hooge parameter α_H=6.8×10^{-6}, for the devices under steady-state, is quite a normal value for these type of devices [30]. Our results show that the time domain analysis of an RTS is not only useful in extracting the RTS parameters, but also in extracting the $1/f$ noise of the device using the separation procedure.

3.5 Conclusions

Time-domain RTS measurements yield results leading to a better understanding of the RTS. Using the time-domain analysis we are able to extract the RTS parameters under periodic large-signal excitation, which would otherwise (frequency-domain) have not been possible, thus providing more insights into the cyclo-stationary RTS behavior. Our measurement results show that the RTS parameters under periodic large-signal excitation conditions (cyclo-stationary RTS) are different as compared to the parameters under steady-state. The analytical expression for the noise PSD of an RTS [2] holds good for cyclo-stationary RTS, in the low-frequency range below the switching frequency of the RTS. The time-domain procedure in [48] has been used to separate the two-level RTS from the device background noise. Measurement results indicate that this noise is $1/f$ in nature (α_H=6.8×10^{-6}).

The physical origins of an RTS in a MOSFET,
Lie in the trapping/detrapping of carriers in a defect.
Generation-recombination is not new after all,
T'was developed in the fifties by Shockley-Read-Hall !!

The topic has received renewed attention,
Especially under periodic large-signal excitation.
The measured noise reduction for a 50% duty-cycle is more than 6 dB..
Which is not predicted by the (circuit) simulated noise PSD !!

The steady-state RTS model is based on the S-R-H theory,
Extended to the dynamic case, using the state-variable- trap-occupancy !!
The 'anomalous' change in the cyclo-stationary RTS noise PSD,
Can be traced to the large change in the measured 'cyclo-stationary' RTS 'τ_e' !!

4

Modeling of Random Telegraph Signals

COMPUTER Aided Design (CAD) is an essential component in the design of modern integrated circuits. This process involves solving a large set of equations describing the connections between various circuit elements and the models in CAD which describe the circuit elements. Statistics show that most of the computation time is spent in evaluating the quantities described by the device model equations. Thus the growing need for developing simple analytical device models without compromising on the accuracy. Such efficient models are called *compact* models [59].

A rigorous method of modeling is to divide the device into finite volume elements, and write the semiconductor equations in three dimensions describing the particular element. These are typically non-linear differential equations, each defined for the finite volume element in the device. There are programs available for setting up such equations and solving them numerically under given boundary conditions. Although such programs are invaluable for a device (as opposed to circuit) analysis, they are computationally intensive and slow as compared to compact device models.
There are three main types of compact models [59].

- *Physical models*: These are based on device physics and the model parameters have a physical significance.
- *Empirical models*: Empirical models rely on curve fitting using any equation that adequately fits the observed behavior. The parameters in a empirical model are just coefficients, exponents etc. and have no physical significance.
- *Table models*: These are typically in the form of tables containing the values of the required device parameters for a large combination of biasing voltages. It is

like a look-up table whose values come from measurements or numerical device simulations. For higher accuracy, large number of values need to be stored.

Empirical and table models provide values independent of the phenomenon responsible for the values. These models are unable to make a prediction when device parameters are changed. They cannot be used for statistical modeling. Physical models on the other hand can accurately describe a model parameter under changing device parameters.

The device parameter of our interest is RTS noise in MOSFETs. The RTS noise limits the achievable circuit performance in analog and RF CMOS (*e.g.* LF noise in amplifiers and filters for radio receivers and phase noise due to up-converted LF noise in oscillators). The need for an accurate RTS noise model is thus important as it helps in the optimization of the circuit design. In *chapter 3* we reported that the RTS parameters extracted from the time-domain can be used in an analytical expression to predict the RTS noise PSD [2]. Thus in order to model the RTS noise, the RTS parameters have to be modelled first. The RTS model presented in this chapter is primarily based on the Shockley-Read-Hall statistics of capture and emission [60–62].

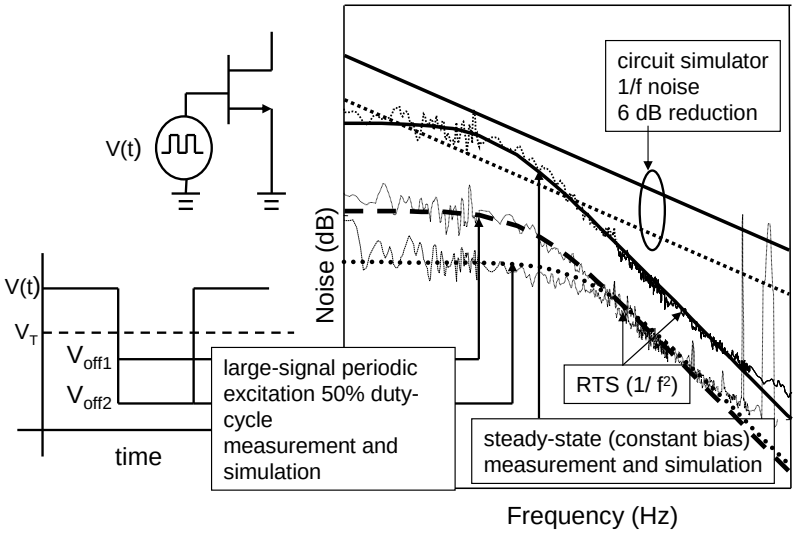

Figure 4.1 Steady-state LF noise spectrum and LF noise spectra under periodic large-signal excitation for two 'off' voltages ($V_{GS-off1}$ and $V_{GS-off2}$), measurement and simulated using our model. Also shown is the LF noise predicted by circuit simulator 'Spectre-RF' in steady-state and periodic excitation with a 50% duty-cycle.

In *chapter 3* we have seen that the RTS time-constants and thus the RTS noise in MOSFETs changes significantly under changing gate bias [40, 41, 43, 47], and can prove to be beneficial for oscillators and PLLs. Unfortunately, the circuit simulators available

do not model this behavior [34]. Even circuit simulators that support time-variant noise sources (*e.g*. periodic steady-state analysis of Spectre RF), do not adequately model the observed effects. A statistical simulation model [63] was proposed, which modelled the macroscopically observed bias dependence of the RTS time-constant without a physical basis. To address these issues and overcome the shortcomings, in this chapter we present a physical RTS model, which can be used under steady-state and under large-signal excitation. This is shown in Fig.4.1. Our model results are verified by the time-domain RTS measurements under steady-state and periodic large-signal excitation presented in *chapter 3*. In addition, we investigate trap behavior under transient biasing conditions that is not observable in steady-state, thus providing more insight in trapping and de-trapping mechanisms. By using our time-domain RTS measurements during transient biasing and under periodic large-signal excitation we are able to predict the RTS time-constants belonging to the 'off' state of the device!

The organization of this chapter is as follows. The following section provides a brief description of the origins of RTS and traps in MOSFETs. In the next section, we introduce the physics based RTS noise model under steady-state primarily based on the Shockley-Read-Hall statistics. After having completed the steady-state analysis of RTS, the next section discusses our transient biasing time-domain RTS measurements. The transient trap-occupancy (for a step response) analysis is also discussed. This is followed by the RTS behavior under periodic large-signal excitation. In this section our measurement results are compared with our model. Finally, the chapter concludes with discussions and conclusions.

4.1 Traps and origin of RTS

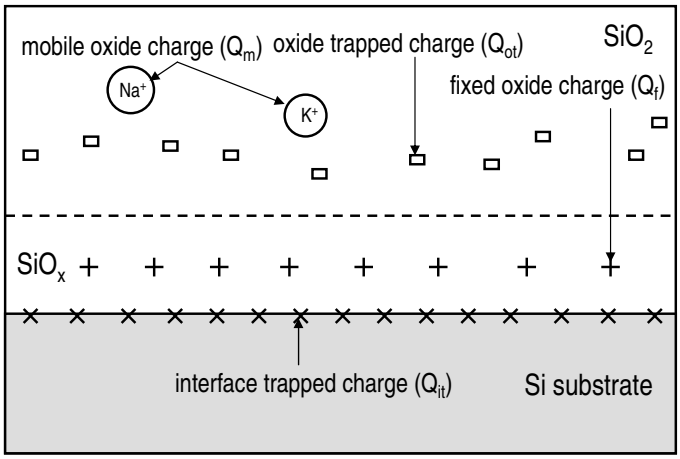

Figure 4.2 Different types of charges associated with the Si-SiO_2 interface.

The enormous growth in CMOS technology has been made possible by the unique properties of silicon dioxide (SiO_2): the only native oxide of a common semiconductor which is stable in water and at elevated temperatures, an excellent electrical insulator, a mask to common diffusing species, and capable of forming a nearly perfect electrical interface with its substrate. Deposited silicon dioxide has almost been studied as long as thermal growth on the substrate, and has been employed in various ways in IC fabrication due to its familiarity, versatility, and reliability. With downsizing the demands made on the gate-oxide are still strengthened and the quality of the gate-oxide needs to be of the highest quality [64, 65]. However, this is not always possible and in general there are four kinds of possible defects or traps associated with the Si-SiO_2 system [65]. This is shown in Fig.4.2.

- Mobile Na^+ and K^+ ionic charge in the SiO_2 (Q_m). This could be introduced as contamination during the processing.
- The fixed oxide charge (Q_f) exists mostly due to structural defects in the oxide layer, and is located relatively close to the interface. The density of this charge, whose origin is related to the thermal oxidation process, depends on the oxidation temperature, on the cooling conditions and on the silicon orientation. It is not influenced by the electrical operating conditions of the MOSFET.
- The interface trapped charge (Q_{it}), which is situated at the Si-SiO_2 interface, is believed to originate from structural oxidation induced defects, metal impurities and different kinds of bond breaking processes, caused by radiation, hot carrier stress or other phenomena. Although the physical origin of the interface traps is not totally known, experiments support the view that these traps primarily arise from dangling bonds at the Si-SiO_2 interface. This is supported by the fact that most of the interface trap charge created during processing is passivated by a low temperature anneal, in which hydrogen atoms are bonded to the dangling bonds.
- The oxide trapped charge (Q_{ot}) may be positive or negative due to holes or electrons trapped in the bulk of the oxide. This charge is introduced in MOSFETs due to ionizing radiation, hot carrier stress, Fowler-Nordheim tunneling, or other mechanisms. The oxide trapped charge created during processing is normally removed by a low temperature anneal. Oxide trapped charge influences the transistor characteristics. Electrons (holes) trapped in the oxide lead to an increase (decrease) in the threshold voltage.

The interface trapped charge and the oxide trap charge are, unlike the fixed and the mobile oxide charge, in electrical communication with the underlying silicon, and can thus be charged and discharged, depending on the surface potential. These traps can be donor or acceptor type [66]. The donor trap is neutral when filled with an electron and positively charged when empty. An acceptor-like trap is negative charged when filled with an electron and neutral when empty.

From the previous chapter, the fluctuation in the drain current of small dimension MOSFETs is more than often dominated by RTS. The RTS can switch from two or more

discrete states. The origin of such RTSs are attributed to trapping-detrapping events caused by an individual interface defect near the Si-SiO_2 interface. The discrete levels of a two-level RTS correspond to a high and low conductivity in the channel caused as a direct outcome of the trapping-detrapping of charge carriers which change the channel conductivity. The times in the high and low-current states correspond to carrier capture and emission in traps or defects. The physics behind the capture and emission of charge carriers in traps is described by the Shockley-Read-Hall statistics in the following section.

4.2 RTS in steady-state

The influence of interface traps and the traps in the oxide on the performance of a semiconductor device is determined by the density of interface states and the probability that these states are occupied by a charge carrier. A trap can change its occupancy by either capturing or emitting a charge carrier. The Shockley-Read-Hall (S-R-H) theory [60, 61], originally meant to describe the action of bulk states has been generally adopted to describe the trapping-detrapping behavior for the interface traps as well. For the traps located in the oxide, the mechanism is a two-step process, capture and then tunneling through the oxide. This process is explained later in detail in the following section.

4.2.1 S-R-H statistics

In this section we primarily consider the behavior in n-MOSFETs where the exchange of charge carriers is primarily between the conduction band and the interface state. The assumptions made by the theory do not impose serious limitations on the applicability of the theory. The underlying assumptions of the theory are as follows:

- The trap changes occupancy by a unit charge. A donor trap will change charge state from 0 to $+q$ and vice versa, while an acceptor trap will change charge state from 0 to $-q$ (q being the elementary charge).
- Capture and emission are instantaneous processes. No lattice dynamical phenomenon (such as phonon emission and lattice relaxation) are included.
- The trap is defined by an energy level (E_T) which is independent of its occupancy.
- The traps do not interact with each other and as a result do not form an energy band.

The charge exchange process between an interface trap and the conduction or valence band of the silicon is illustrated in Fig.4.3. Similar to other topics in semiconductor physics, it is convenient to describe the exchange of charge carriers with the valence band in terms of holes instead of electrons: capture of an electron from the valence band is equivalent to emission of a hole, and the emission of an electron to the valence band is equivalent to a hole capture.

An interface trap is characterized by two parameters: the trap energy (E_T) and the cross section for capture (σ). The rate of capture of an electron is given by

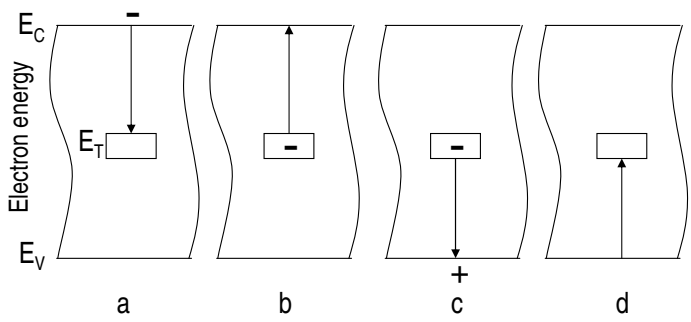

Figure 4.3 The basic processes involved in recombination by trapping: (a) denotes electron capture, (b) electron emission, (c) hole capture and (d) denotes hole emission.

$$R_c = n v_{th} \sigma [1 - P_f] \tag{4.1}$$

where $1 - P_f$ represents the probability that the trap is empty and thus capturing an electron, n is the electron concentration at the interface, v_{th} is the thermal velocity and σ represents the cross section for capture of an electron by the trap.

The rate of emission of an electron from the trap to the conduction band is given by

$$R_e = n_1 v_{th} \sigma P_f \tag{4.2}$$

where P_f represents the probability that the trap is filled and thus emitting an electron, n_1 is the electron concentration in the conduction band where the Fermi-level falls at E_{T}.

Since the processes involved are governed by the Fermi-Dirac statistics [60], the probability that a trap is occupied (P_f) is a function of its energy (E_{T}) and the Fermi-level associated with the trap (F_t).

$$P_f = 1/[1 + exp(E_T - F_t)/kT] \tag{4.3}$$

where k represents the Boltzmann's constant and T is the absolute temperature. Thus $1 - P_f$ represents the probability that the trap is empty. The electron concentration (n) at the interface is given by

$$n = N_c exp[(F_p - E_c)/kT] \tag{4.4}$$

where N_c represents the density of states in the conduction band, E_c represents the conduction band energy, and F_p is the Fermi-level associated with the electrons. On similar lines, n_1, the electron concentration in the conduction band where the Fermi-level falls at E_{T} is given by

$$n_1 = N_c exp[(E_T - E_c)/kT] \tag{4.5}$$

For a trap-electron system in thermal equilibrium, $F_p = F_t$. Introducing the mean time-constants for the capture and emission process, $\bar{\tau_c}$ and $\bar{\tau_e}$ which are given by:

$$\bar{\tau_c} = \frac{1}{n\sigma v_{th}}; \qquad \bar{\tau_e} = \frac{1}{n_1\sigma v_{th}} \tag{4.6}$$

the capture and emission rates can be expressed as:

$$R_c = \frac{1-P_f}{\bar{\tau_c}}; \qquad R_e = \frac{P_f}{\bar{\tau_e}} \tag{4.7}$$

In steady-state, the principle of detail balancing requires that the rate of capture and the rate of emission of electrons must be equal. Using Eqns.4.3 through 4.7 we get

$$\frac{\bar{\tau_c}}{\bar{\tau_e}} = exp[(E_T - F_p)/kT] \tag{4.8}$$

From Eqn.4.8 we see that when the trap energy (E_T) is equal to the Fermi-level (F_p), the mean capture time ($\bar{\tau_c}$) is equal to the mean emission time ($\bar{\tau_e}$).

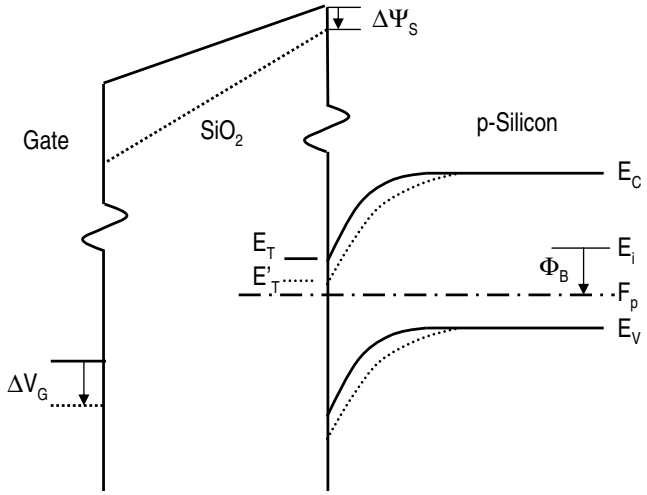

Figure 4.4 The band bending in an n-MOSFET. The dotted lines show the change corresponding to an increase in the gate voltage (ΔV_G). $\Delta\psi_s$ is the change in the surface potential. ϕ_B denotes the potential of the bulk Fermi-level F_p with respect to the intrinsic level E_i.

4.2.2 Effect of V_{GS} on $\bar{\tau_c}$

Consider the case of an increasing gate-to-source voltage (V_{GS}). Qualitatively it can be observed that an increasing V_{GS} causes an increase in the band bending and thus an increase in the electron concentration at the interface (n) (see Fig. 4.4). This increase then

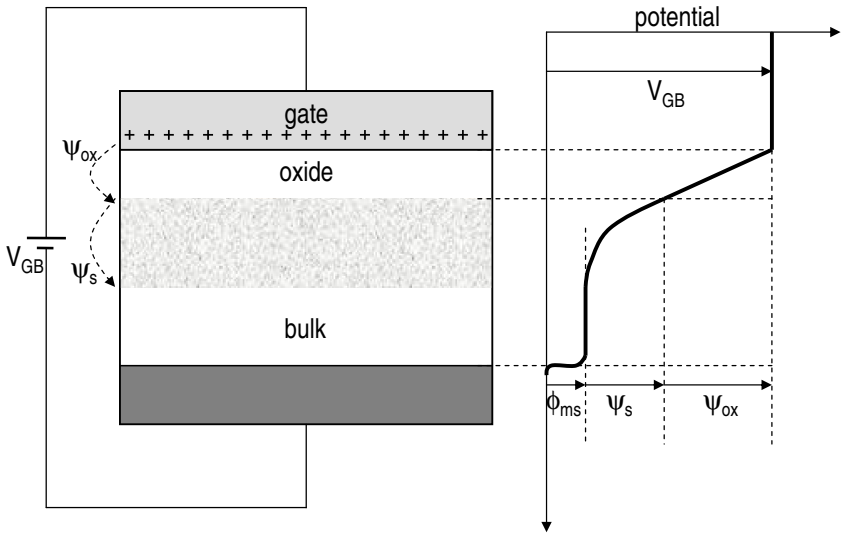

Figure 4.5 A p-substrate two-terminal MOS structure under gate bias. The graph on the right indicates the potential distribution along the MOS structure from gate to bulk.

results in the decrease of $\bar{\tau_c}$ (from Eqn.4.6). Note that in our RTS measurements, we denoted the time-constants of the RTS as $\bar{\tau_1}$ and $\bar{\tau_0}$ corresponding to the 'high' and the 'low' state. In order to identify which state corresponds to an 'empty' or 'filled' state, we have to distinguish between acceptor and donor traps [66]. An acceptor is negatively charged after capturing an electron and neutral after emitting it. For the donor trap the neutral state corresponds to a captured state and is positively charged after emission [67,68]. Note that in both type of traps, the neutral state corresponds to the 'higher' current state (as an outcome of a reduced threshold voltage due to the presence of the oxide charge). Thus for an acceptor trap, the 'high' current state corresponds to an electron capture. Acceptor traps are commonly observed in n-MOSFETs, where as donor traps are only observed at low-temperatures below 70K [67]. In our RTS time-domain measurements the time-constant ($\bar{\tau_1}$) decreasing with increasing V_{GS} thus corresponds to $\bar{\tau_c}$, and the other ($\bar{\tau_0}$) corresponds to $\bar{\tau_e}$.

Surface Potential (ψ_s)

The increase in the electron concentration with increasing V_{GS} is given by Eqn.4.4. The change in the conduction band edge E_c at the interface with increasing V_{GS} is given by the change in the surface potential ψ_s (Fig.4.4). Fig.4.5 shows the potential distribution in a two-terminal MOSFET for an increasing gate potential. In all our RTS measurements the source and the bulk are kept at the same potential ($V_{SB} = 0$). For a MOSFET with

a source and drain the surface potential varies from the source side to the drain side and can be determined using the charge sheet model [59]. Using the principles of potential balance and charge balance along the MOSFET, we can derive a relation between the surface potential ψ_s and the gate-voltage V_{GB} using the bulk or substrate as reference [59].

$$\psi_{s0} = V_{GB} - V_{FB} - \gamma\sqrt{\psi_{s0} + \frac{kT}{q}e^{(\psi_{s0}-2\phi_B-V_{SB})/kT}}$$
$$\psi_{sL} = V_{GB} - V_{FB} - \gamma\sqrt{\psi_{sL} + \frac{kT}{q}e^{(\psi_{sL}-2\phi_B-V_{DB})/kT}} \tag{4.9}$$

where V_{FB} is the flat-band voltage of the MOSFET, γ is the body effect coefficient, ϕ_B is the built in voltage as seen from Fig.4.4, ψ_{s0} and ψ_{sL} represent the surface potential at the source and drain side respectively (L being the channel length), V_{SB} and V_{DB} are the source-bulk and drain-bulk voltages respectively. The body effect coefficient is given by

$$\gamma = \frac{\sqrt{2q\varepsilon_s N_A}}{C_{ox}} \tag{4.10}$$

where ε_s is the permittivity of silicon, N_A is the bulk doping concentration, q the electron charge, and C_{ox} the gate-oxide capacitance per unit area. ψ_s from Eqn.4.9 is a function of the longitudinal channel position y_T (which is zero at the source side and equal to L, the channel length, at the drain side). The surface potential can be written as

$$\psi_s(y_T) = \psi_{s0} + V_{ch} \tag{4.11}$$

where ψ_{s0} is the surface potential at the source side of the MOSFET. In the linear mode, for small values of V_{DS}, the channel voltage V_{ch} can be expressed in terms of V_{DS}, the longitudinal position y_T and the channel length L

$$V_{ch} = \frac{y_T V_{DS}}{L} \tag{4.12}$$

Eqn.4.9 can be iteratively solved using a computer. Methods to speed computation of ψ_s are available in literature [59].

4.2.3 Effect of V_{GS} on $\bar{\tau}_e$

A closer look at Eqns.4.5 and 4.6 tells us that the mean emission time $\bar{\tau}_e$ depends on the energy of the trap (E_{T}). Thus one would expect that with increasing V_{GS} there would be no change in $\bar{\tau}_e$, as the energy of the trap is independent of the applied gate voltage. This is indeed the case for an interface trap. But for a trap located in the oxide this is not the case.

There are two mechanisms for explaining the capture and emission of an electron for a trap located in the oxide. The 'Tunneling and Capture' model [7], in which the carriers first tunnel to a distance from the conduction band edge at the interface into the oxide,

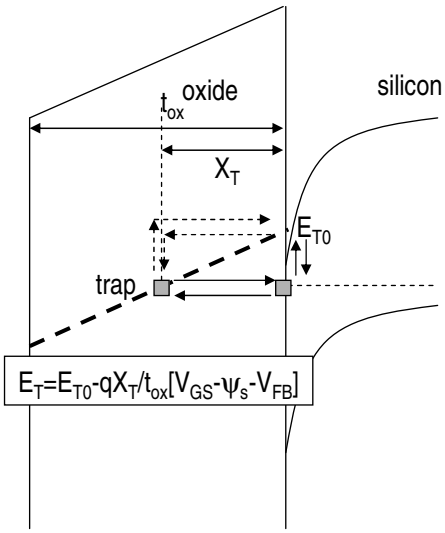

Figure 4.6 'Tunneling and Capture' (dotted arrows), and 'Capture and Tunneling' (solid arrows) mechanisms for the capture and emission process for a trap located in the oxide at a distance X_T from the interface for an n-MOSFET. The arrows indicate electron transitions. Also shown is the trap energy E_T in the oxide as function of the applied gate voltage.

and then are captured by traps that have the same energy as F_p. This model is illustrated in Fig.4.6 by the dotted arrows. This model had problems, since the measurement data did not support energy dissipation in the oxide [69]. The 'Capture and Tunneling' model [10] was proposed as an alternative to the previous proposed model. In the latter, the carriers first get trapped by fast defect centers at the interface through a Shockley-Read-Hall (SRH) process, and then tunnel into the traps in the oxide, illustrated in Fig.4.6 by the solid arrows. Thus the carriers do not dissipate energy in the oxide. A continuous trap energy distribution over the band gap at the interface is required for this process to be effective, the presence of which is generally accepted for the Si-SiO_2 interface system. Fu and Sahs 'Capture and Tunneling' model was used as the basis for the oxide trapping mechanism implemented in our RTS model.

An increasing V_{GS} increases the potential across the oxide and as a result leads to the band-bending in the conduction band edge of the oxide (Fig.4.6). The potential across the oxide is a function of the flat-band voltage of the MOSFET (V_{FB}) and the surface potential (ψ_s) (See Fig.4.5). Thus the trap energy (for a trap located in the oxide) can be expressed

as function of the applied $V_{\rm GS}$ as [70, 71]

$$E_T = E_{T0} - \frac{qX_T}{t_{ox}}[V_{GS} - \psi_s - V_{FB}] \tag{4.13}$$

where X_T is the distance of the trap from the Si-SiO_2 interface, t_{ox} is the gate-oxide thickness, and E_{T0} represents the trap-energy at flat-band.

From Eqn.4.13 we can see that for a trap at the interface ($X_T = 0$), E_T is independent of $V_{\rm GS}$. Throughout our model, the reference energy level is the conduction band energy level E_c in bulk silicon in equilibrium. From Eqns.4.5 4.6 and 4.13 we see that for a trap located in the oxide, increasing the $V_{\rm GS}$ leads to a decrease in n_1 which in turn leads to an increase in $\bar{\tau_e}$.

4.2.4 Capture Cross Section (σ)

In Eqn.4.6 the capture cross section (σ) is the effective area of the trap and is a quantitative way of expressing the capability of the trap to capture free charge carriers. In semiconductor physics, the probability of occurrence of a particular event (in our case the capture of an electron in a defect) is conveniently expressed in terms of the cross-section [60]. A larger cross-section indicates a higher probability of capturing an electron and thus a smaller $\bar{\tau_c}$ (Eqn.4.6).

As described earlier, for a trap located in the oxide, the electron needs to tunnel through the SiO_2 in order to be captured. This tunneling is a quantum mechanical phenomenon and a detailed analysis of such a mechanism would involve knowledge about the trap structure. Since this information is unavailable, a semiclassical approach is taken in which the details of the trapping site are included in the capture cross section of the trap (σ).

The problem of an electron tunneling through a potential barrier (in our case the potential barrier is the difference between the electron affinities of Si and SiO_2) is a familiar problem in quantum mechanics. On solving Schrödinger's equation in the region inside the barrier, the wave-function $\varphi(x)$ decays exponentially as the electron tunnels deeper into the oxide [72–74].

$$\varphi(x) = Ce^{-\kappa x} \tag{4.14}$$

The decay constant is given by

$$\kappa^2 = \frac{2m^*}{\hbar^2}(W - E_0) \tag{4.15}$$

where m^* is the electron mass, $\hbar$ is Planck's constant, W is the potential barrier, and E_0 is the energy (kinetic) of the electron. The wave-function $|\varphi(x)|^2$ represents the probability of finding an electron as a function of the distance x. As we go deeper into the oxide, the probability of finding an electron reduces exponentially. This probability is included in the capture cross section of the trap which is given by [74]

$$\sigma = \sigma_0 e^{-X_T/X_0} \tag{4.16}$$

where X_T is the distance of the trap in the oxide, X_0 is the decay constant ($X_0 = 1/2\kappa$) (see Eqn.4.15), and σ_0 represents the intrinsic capture cross section of the trap at the interface. Thus the quantum mechanical tunneling of the electron in the oxide trap is effectively included by the capture cross section in Eqn.4.16.

4.2.5 Occupancy

The steady-state trap-occupancy (P_f) is the probability that the trap is filled or occupied and is given by Eqn.4.3. In steady-state we have $F_t = F_p$, and P_f is a function of F_p, the Fermi-level for electrons in the conduction band. Thus, an increasing V_{GS} leads to an increase in P_f. Rather than expressing the trap-occupancy as a function of the Fermi-levels, a more convenient representation is

$$P_f = \frac{\overline{\tau_e}}{\overline{\tau_c} + \overline{\tau_e}} \tag{4.17}$$

Eqn.4.17 can be easily derived by substituting Eqns.4.4, 4.5, and 4.6 in Eqn.4.3. The advantage of expressing the trap-occupancy in terms of $\overline{\tau_e}$ and $\overline{\tau_c}$ is that $\overline{\tau_e}$ and $\overline{\tau_c}$ can be easily measured from an RTS measurement.

4.2.6 RTS Amplitude

The RTS amplitude ΔI_D is calculated by assuming an elementary electron charge in the channel that changes the channel conductivity [68, 75–77]. The amplitude of the RTS depends on instantaneous bias conditions. The relative RTS amplitude can be expressed as the sum of the number of carriers and the mobility fluctuation [75].

$$\frac{\Delta I_D}{I_D} = \frac{\Delta N}{N} + \frac{\Delta \mu}{\mu} = -\frac{1}{WL}[\frac{1}{N_s} \pm \alpha\mu] \tag{4.18}$$

where N_s is the sheet concentration of carriers in the channel, μ is the channel mobility, W and L are the gate width and length, and α is the mobility scattering coefficient. The sign in front of the second term depends on whether a trap is neutral or charged after capturing an electron. The first term of Eqn.4.18 expresses the screening of charged traps by channel electrons. For a given drain bias, the behavior of the RTS amplitude is determined by the number fluctuations. If the gate-voltage does not change too much, $\alpha\mu$ can be assumed to be constant. The second term of Eqn.4.18 describes the effect of mobility fluctuations, which are mainly due to Coulomb scattering by charged traps. Traps that are further away from the Si-SiO_2 interface produce a smaller $\Delta I_D/I_D$. Scattering increases for traps that are charged after electron capture. The relative RTS amplitude can be also explained by the strategic or less strategic position of the trap [77].

In our RTS measurements, the values of $\Delta I_D/I_D$ (ranging from 0.4 to 1.2 %) were found to match the values predicted by Eqn.4.18. In this study, the RTS amplitude was not the focus of attention. Our RTS measurements under periodic large-signal excitation showed that the RTS amplitude does not change as compared to the RTS amplitude in the steady-state.

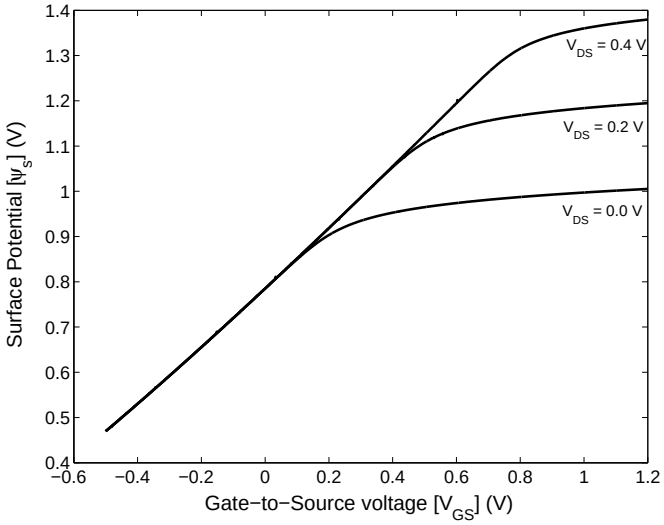

Figure 4.7 The surface potential ψ_s at the drain-side as a function of the gate-to-source voltage V_{GS} for different values of drain-to-source voltage V_{DS}. V_{FB}=-1.6 V.

4.2.7 Model Results (steady-state)

Our RTS model is based on the trapping-detrapping theory described in the previous section [51]. Our RTS model uses three physical parameters to characterize a trap located in the oxide: the trap energy in the silicon band-gap at flat-band (E_{T0}), the location of the trap in the oxide (X_T), and the intrinsic cross-section of the trap (σ_0). These model parameters were extracted from our RTS time-domain measurements of $\overline{\tau_e}$ and $\overline{\tau_c}$ versus V_{GS} in the steady state. The devices used for our RTS measurements were n-MOSFETs transistors with W:L=1:0.13 fabricated in a $0.18\,\mu m$ CMOS process flow with gate-oxide thickness t_{ox}=7 nm. As mentioned previously in chapter 3, the RTS was completely characterized in the time-domain. The biasing conditions *viz.* the gate-to-source voltage (V_{GS}) and the drain-to-source voltage (V_{DS}) were monitored during the RTS measurements.

As mentioned in the previous section, the surface potential determines the band-bending at the interface and thus the electron concentration. In order to accurately determine ψ_s as a function of the applied V_{GS} Eqn.4.9 has to be solved iteratively. Fig.4.7 shows ψ_s as a function of V_{GS} calculated using our model for an n-MOSFET with V_{FB}=-1.6 V. ψ_s along the MOSFET channel from the source (ψ_{s0}) to the drain (ψ_{sL}).

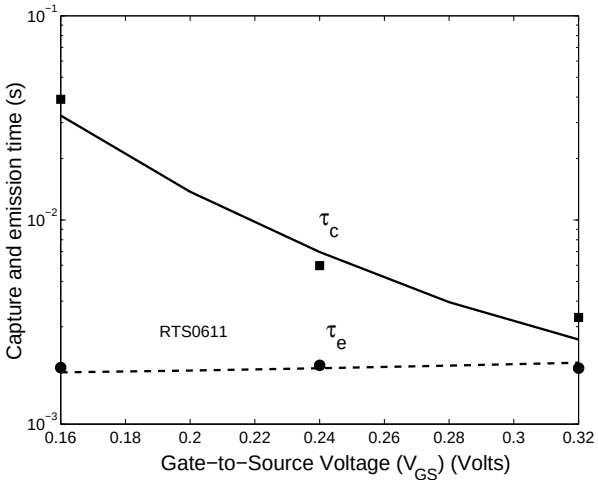

Figure 4.8 RTS time constants $\overline{\tau_e}$ and $\overline{\tau_c}$ as a function of V_{GS} variation for V_{DS} = 50 mV, measurements and simulation, for a trap located at the interface.

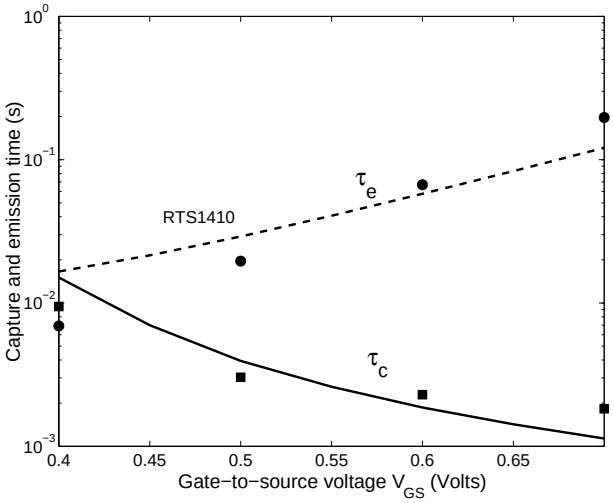

Figure 4.9 RTS time constants $\overline{\tau_e}$ and $\overline{\tau_c}$ as a function of V_{GS} variation for V_{DS} = 40 mV, measurements and simulation, for a trap located in the oxide.

In order to determine the band-bending at the trap location, ψ_s has to be determined at the longitudinal distance of the trap from the source (y_T). Figs.4.8 and 4.9 show the variation of $\bar{\tau_c}$ and $\bar{\tau_e}$ as a function of $V_{\rm GS}$, for a trap located at the interface and for a trap located in the oxide ($X_{\rm T}$ = 1.5 nm) respectively. The markers indicate measurement and the solid and dotted lines indicate our model simulation. The trap energy E_T does not affect $\bar{\tau_c}$ (See Eqns.4.6,4.4). The variation in $\bar{\tau_c}$ as a function of $V_{\rm GS}$ is because of the changing electron concentration at the surface (n). The change in n depends on $(F_p - E_c)$, and thus on the surface potential ψ_s at y_T the longitudinal distance of the trap from the source. From Fig.4.7, increasing $V_{\rm GS}$ beyond strong inversion does not influence ψ_s, and the increasing voltage is dropped across the oxide. In our model the effect of y_T on the RTS time-constants was accounted for by using ψ_s at y_T to fit the measured data.

The trap depth in the oxide, X_T, was determined by the slope in $\bar{\tau_e}$ (Eqns.4.5, 4.6, and 4.13). The shape of $\bar{\tau_c}$ and $\bar{\tau_e}$ was thus determined by computing ψ_s and extracting X_T. In order to match the measured values, the intrinsic cross-section σ_0, and the trap-energy E_{T0} were then extracted to match the measured $\bar{\tau_c}$ and $\bar{\tau_e}$ respectively. Table 4.1, shows

Table 4.1 Extracted physical model parameters for 3 different traps on 3 different devices.

	E_{T0} (eV)	X_T (nm)	σ_0 (cm^2)
RTS1410	0.126	1.5	1.0×10^{-17}
RTS1613	0.120	2.0	4.0×10^{-16}
RTS0611	0.015	0.2	2.2×10^{-23}

the extracted model trap-parameters for three different traps.

4.3 RTS under Transient Biasing

We concluded from chapter 3 that the RTS parameters under periodic large-signal excitation conditions (cyclo-stationary RTS) are different as compared to the parameters under steady-state. The first step towards analyzing the RTS behavior under periodic large-signal excitation (dynamic conditions) is to study the RTS behavior under transient biasing. In transient biasing conditions the device is 'off' for a long period, and is turned on at time $t = 0$ by applying a step voltage at the gate of the MOSFET.

We have already seen from the previous section how $\bar{\tau_c}$ and $\bar{\tau_e}$ vary as a function of $V_{\rm GS}$ in steady-state. Now consider the case of a MOSFET under transient biasing. The MOSFET is 'off' for t<0 and is 'on' for t>0. The Fermi-level for the electrons $F_{\rm n}$ changes instantaneously with changes in $V_{\rm GS}$. The RTS time constants corresponding to the two states are $\bar{\tau}_{c-on}$ and $\bar{\tau}_{e-on}$ for the 'on' state and $\bar{\tau}_{c-off}$ and $\bar{\tau}_{e-off}$ for the 'off' state. In steady-state when the device is 'on', the trap-occupancy is given by: $\bar{\tau}_{e-on}/(\bar{\tau}_{e-on} +$

$\overline{\tau}_{c-on}$). When the device is in the 'off' state for a long period, with no charge carriers in the channel, the trap-occupancy $(\overline{\tau}_{e-off}/(\overline{\tau}_{eoff}+\overline{\tau}_{c-off}))$ is almost zero as $\overline{\tau}_{c-off}\rightarrow\infty$. After the device is switched 'on' or 'off', the trap-occupancy takes time to adapt to the new bias condition.

This *instantaneous occupancy* or (trap-occupancy as a function of time) can be analyzed as follows. The analysis is along the lines of deriving the PSD of the RTS in *chapter 2* [2]. The RTS can be in one of the two states 0 (empty) or 1 (full). The probability of making a transition to 0 in a short time dt given that we are in state 1 is $dt/\overline{\tau}_e$ (mean time trap was filled). Similarly, the probability of making a transition to 1 in a short time dt given that we are in state 0 is $dt/\overline{\tau}_c$ (mean time trap was empty). It follows that the $\overline{\tau}_c$ and $\overline{\tau}_e$ are the mean capture and emission lifetimes.
At time $t=0$, the MOSFET is turned 'on'. The device was 'off' for a long period before turning 'on'. The occupancy is the probability of a trap being occupied or in other words it is the probability of being in state 1 $(P_{(0|1)1})$. (The probability of being in state 1, whatever the initial state (0 or 1) at $t=0$).
The differential equation for $P_{(0|1)1}$ is as follows. For a small increment dt we get

$$P_{(0|1)1}(t+dt)=P_{(0|1)0}(t)\frac{dt}{\overline{\tau}_c}+P_{(0|1)1}(t)(1-\frac{dt}{\overline{\tau}_e}) \tag{4.19}$$

The probability $P_{(0|1)1}(t+dt)$ of being in state 1 at time $t+dt$, is the sum of the probabilities of two mutually exclusive events:
(a) probability of being in the state 0 (empty) at time $t,(P_{(0|1)0})$ and one transition (0 to 1) in $dt,(dt/\overline{\tau}_c)$,
(b) probability of being in the state 1 (full) at time $t,(P_{(0|1)1})$ and no transition in $dt,(1-dt/\overline{\tau}_e)$,
We also have,

$$P_{(0|1)1}(t)+P_{(0|1)0}(t)=1 \tag{4.20}$$

In the limit that $dt\rightarrow 0$, from 4.19 and 4.20, and eliminating $P_{(0|1)0}(t)$, we obtain a differential equation

$$\frac{dP_{(0|1)1}}{dt}+(\frac{1}{\overline{\tau}_e}+\frac{1}{\overline{\tau}_c})P_{(0|1)1}=\frac{1}{\overline{\tau}_c} \tag{4.21}$$

Substituting

$$\tau_R=\frac{\overline{\tau}_e\overline{\tau}_c}{\overline{\tau}_e+\overline{\tau}_c} \tag{4.22}$$

and solving 4.21 we get

$$-\tau_R\ln(\frac{1}{\overline{\tau}_c}-\frac{P_{(0|1)1}(t)}{\tau_R})+C=t \tag{4.23}$$

At $t=0$, let the occupancy (probability of being being in state 1 at $t=0$) be P_f^0. The value of the constant C is thus

$$C=\tau_R\ln(\frac{1}{\overline{\tau}_c}-\frac{P_f^0}{\tau_R}) \tag{4.24}$$

Substituting 4.24 in 4.23 we get

$$-\tau_R \ln(\frac{\tau_R - \bar{\tau}_c P_{(0|1)1}(t)}{\tau_R - \bar{\tau}_c P_f^0}) = t \tag{4.25}$$

Simplifying further the instantaneous occupancy is expressed as

$$P_{(0|1)1}(t) = \frac{\bar{\tau}_e}{\bar{\tau}_c + \bar{\tau}_e} - (\frac{\bar{\tau}_e}{\bar{\tau}_c + \bar{\tau}_e} - P_f^0)e^{-t/\tau_R} \tag{4.26}$$

Thus for a device turned 'on' at time $t = 0$, the trap-occupancy $P_f(t)$ is given by

$$P_f(t) = \frac{\bar{\tau}_{e-on}}{\bar{\tau}_{c-on} + \bar{\tau}_{e-on}} - (\frac{\bar{\tau}_{e-on}}{\bar{\tau}_{c-on} + \bar{\tau}_{e-on}} - P_f^0)e^{-t/\tau_{R-on}} \tag{4.27}$$

where P_f^0 represents the trap-occupancy at $t = 0$, and the time-constant for the exponent $\tau_{R-on} = \bar{\tau}_{e-on}\bar{\tau}_{c-on}/(\bar{\tau}_{e-on} + \bar{\tau}_{c-on})$. On similar lines, for a device turned 'off' at time $t = 0$, the trap-occupancy $P_f(t)$ is given by

$$P_f(t) = \frac{\bar{\tau}_{e-off}}{\bar{\tau}_{c-off} + \bar{\tau}_{e-off}} - (\frac{\bar{\tau}_{e-off}}{\bar{\tau}_{c-off} + \bar{\tau}_{e-off}} - P_f^0)e^{-t/\tau_{R-off}} \tag{4.28}$$

where P_f^0 represents the trap-occupancy at $t = 0$, and the time-constant for the exponent $\tau_{R-off} = \bar{\tau}_{e-off}\bar{\tau}_{c-off}/(\bar{\tau}_{e-off} + \bar{\tau}_{c-off})$. Substituting $t = \infty$ in Eqns.4.27 and 4.28, and comparing with Eqn.4.17 we get the steady-state trap-occupancy in the 'on' and 'off' state respectively.

4.3.1 Measuring Trap-Occupancy under Transient biasing

We devised a measurement method to determine the trap-occupancy change from an 'off' state to an 'on' state. Fig.4.10 shows this technique. The MOSFET was turned 'on' at time $t = 0$ and the RTS frame of a specified time length was captured. Typically the length of the time frame was kept much higher than $\bar{\tau}_c$ and $\bar{\tau}_e$. Several such RTS frames were then recorded. The instantaneous trap-occupancy was then determined by averaging the state of the RTS (high or low) over the recorded RTS time-frames, for a given instant during the 'on' period.

The RTS behavior under transient biasing conditions (step-response) showed that the instantaneous trap-occupancy increased exponentially from the 'off' state occupancy to the 'on' state occupancy. τ_R (the time-constant for the trap-occupancy) is the mean time before the trap-occupancy reaches its steady-state value, and is the given by Eqn.4.22 from the analysis of the trap-occupancy under step-response. Fig.4.11 shows the measurements on three different RTS. In each case, the instantaneous trap-occupancy increased exponentially from the 'off' state occupancy to the 'on' state occupancy. The steady-state 'on' values of $\bar{\tau}_{c-on}$ and $\bar{\tau}_{e-on}$ were measured and used in Eqn.4.27 for our model simulation. Fig.4.11 shows that our model simulation results matches quite well with the measured data.

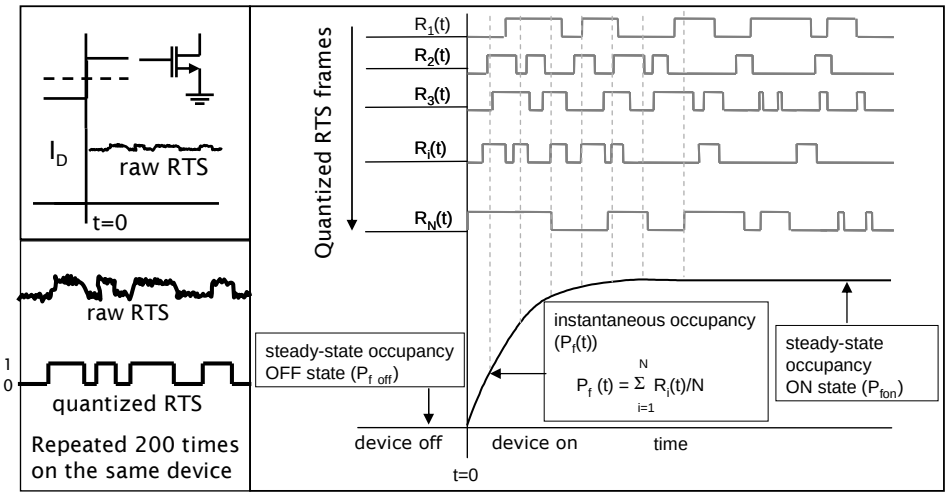

Figure 4.10 Technique for measuring the instantaneous occupancy. The instantaneous trap occupancy is calculated by averaging the state of the RTS over many RTS frames, during the 'on' period.

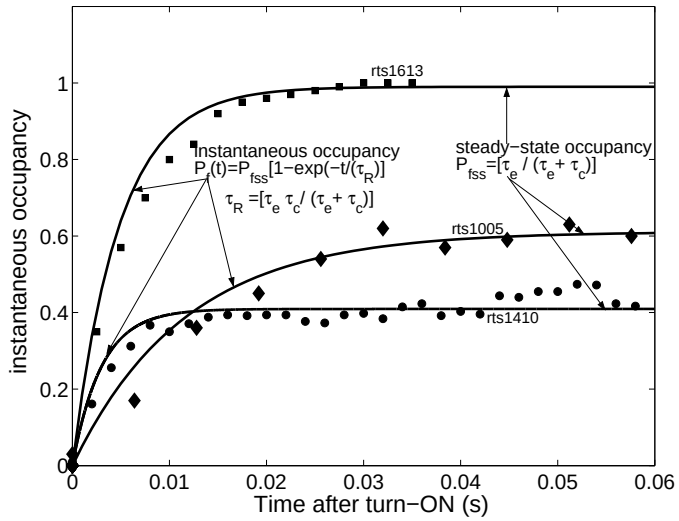

Figure 4.11 Measured and simulated instantaneous occupancies during the 'on' transients for three different RTS on three different devices.

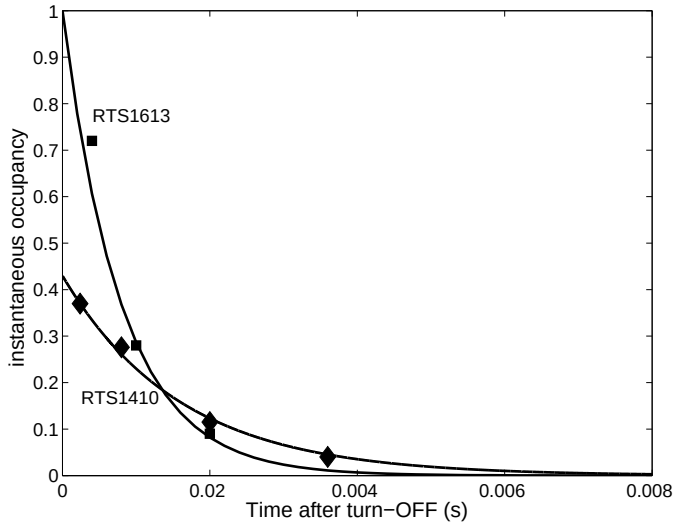

Figure 4.12 Measured and simulated instantaneous occupancies during the 'off' transients for two different RTS.

Now consider the case of the 'off' transience, where the MOSFET is turned 'off' at time $t = 0$. The instantaneous trap-occupancy ($P_f(t)$) during the 'off' transience cannot be measured directly because the transistors are 'off'. $P_f(t)$ was derived indirectly by making use of the the property that the trap-occupancy is a time continuous function. The trap-occupancy before the MOSFET is switched 'on' is equal to the occupancy immediately after turn 'on' (if the sample time is much higher than the mean instantaneous time constants). Thus by varying the time the MOSFET is 'off' and measuring the trap-occupancy the instant the MOSFET is turned 'on', we were able to measure the trap-occupancy transience during the 'off' state.

Fig.4.12 shows the measured instantaneous occupancy during the 'off' transients using the above mentioned technique for two different RTS. Also shown are the model simulation results. Eqn.4.28 is the model expression for the instantaneous occupancy during the 'off' transients. Typically during the 'off' state with no electrons available in the channel for an electron capture, $\overline{\tau}_{c-off} \approx \infty$ is a reasonably good approximation. Substituting this in Eqn.4.28 the expression for the occupancy reduces to

$$P_f(t) = P_f^0 \; e^{-t/\tau_{R-off}} \tag{4.29}$$

where P_f^0 represents the trap-occupancy at $t = 0$ or the steady-state occupancy when the device is 'on', and $\tau_{R-off} = \overline{\tau}_{e-off}$. Using Eqns.4.5, 4.6, and 4.13 our model is able to predict the value of $\overline{\tau}_{e-off}$. From Fig.4.12 we can see that our model simulation of the instantaneous occupancy during the 'off' transience matches quite well with the measurement data.

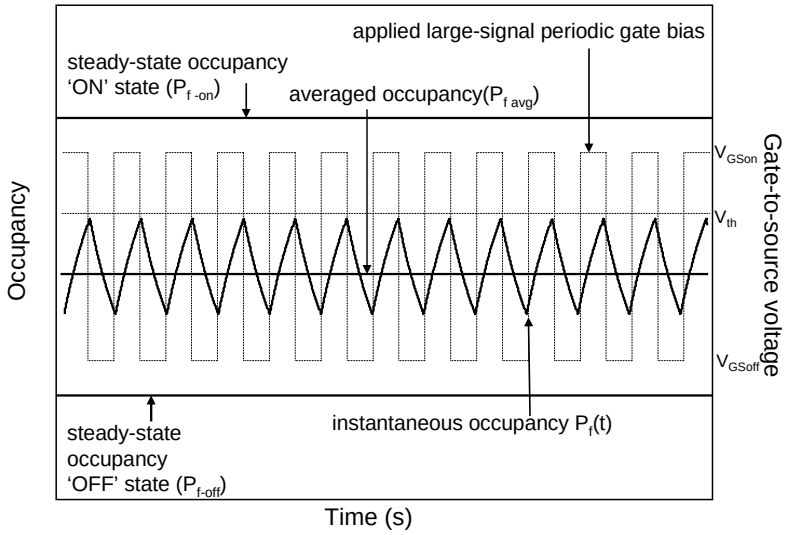

Figure 4.13 Instantaneous occupancy under periodic large-signal excitation simulated using the model. The excitation frequency (f_{sw}) is higher than the corner frequency of RTS. Also shown is the averaged occupancy which lies between the steady-state occupancies in the 'on' and 'off' states.

4.4 RTS Under Periodic Large-Signal Excitation

Under periodic large-signal excitation, the device is alternating between an 'on' state and an 'off' state, by applying a square wave at the gate. Thus we have the case where in the 'on' and 'off' transient conditions are occurring in a periodic fashion. During transients, the capture rate is not equal to the emission rate. Fig.4.13 shows the time-varying trap-occupancy under the influence periodic large-signal excitation. If the periods of the 'on' and 'off' states are much larger than the τ_R (the time-constant for trap-occupancy), the trap-occupancy increases exponentially from the 'off' state occupancy to the 'on' state occupancy, and decreases exponentially from the 'on' state occupancy to the 'off' state occupancy, in a cyclic manner. On the other hand, if the excitation frequency (f_{sw}) is high (typically higher than the corner frequency of the RTS), then the trap-occupancy does not reach the steady-states values in the 'on' and 'off' states. The average trap-occupancy (P_{f-avg}) is somewhere between the steady-state trap occupancy in the 'on' and 'off' state (See Fig.4.13). Intuitively, this makes sense, as it is clear that slow traps cannot adapt quick enough to fast changes in the biasing, resulting in relaxation effects.

Since the RTS time-constants $\overline{\tau}_c$ and $\overline{\tau}_e$ change instantaneously in response to the change in the gate bias from $V_{\mathrm{GS-off}}$ to $V_{\mathrm{GS-on}}$, there exists four RTS time-constant corresponding to the two biasing conditions: $\overline{\tau}_{c-off}$, $\overline{\tau}_{e-off}$, $\overline{\tau}_{c-on}$ and $\overline{\tau}_{e-on}$. These are

shown in Fig.4.14. The 'on' and 'off' states correspond to two instantaneous capture and emission rates given by

$$R_{c-on} = \frac{1-P_{f-avg}}{\bar{\tau}_{c-on}}; \quad R_{e-on} = \frac{P_{f-avg}}{\bar{\tau}_{e-on}}$$
$$R_{c-off} = \frac{1-P_{f-avg}}{\bar{\tau}_{c-off}}; \quad R_{e-off} = \frac{P_{f-avg}}{\bar{\tau}_{e-off}} \tag{4.30}$$

For an excitation frequency much higher than the RTS corner frequency, the mean capture and emission rates (for a periodic large-signal excitation with period T) are as follows:

$$R_{c-cyclo} = \frac{1}{T}\int_0^T R_c(t)\,dt$$
$$R_{e-cyclo} = \frac{1}{T}\int_0^T R_e(t)\,dt \tag{4.31}$$

These mean values correspond to the cyclo-stationary RTS capture and emission rates. The cyclo-stationary RTS time-constants are modelled as:

$$\bar{\tau}_{c-cyclo} = \frac{1-P_{f-avg}}{R_{c-cyclo}}$$
$$\bar{\tau}_{e-cyclo} = \frac{P_{f-avg}}{R_{e-cyclo}} \tag{4.32}$$

When the periodic large-signal excitation used is a square-wave, the two-levels of the large-signal correspond to two-states in the MOSFET, 'on' and 'off', leading to four RTS time-constants: $\bar{\tau}_{c-on}$, $\bar{\tau}_{e-on}$, $\bar{\tau}_{c-off}$, and $\bar{\tau}_{e-off}$ which are shown in Fig.4.14. For the square-wave excitation case, the modelled cyclo-stationary RTS time-constants can be simplified as

$$\frac{1}{\bar{\tau}_{cyclo}} = (\frac{T_{on}}{T})\frac{1}{\bar{\tau}_{on}} + (\frac{T_{off}}{T})\frac{1}{\bar{\tau}_{off}} \tag{4.33}$$

where T_{on} and T_{off} correspond to the durations of 'on' and 'off' periods of the square-wave excitation, T is the time period of the square-wave excitation, and $\bar{\tau}_{on}$ and $\bar{\tau}_{off}$ are the RTS time-constants (emission and capture) in the 'on' and 'off' states respectively.

4.4.1 Model Results (Periodic Large-Signal Excitation)

During our RTS measurements under periodic large-signal excitation, the excitation frequency was kept well above the corner frequency of the RTS. Under these biasing conditions the drain-current was sampled during the 'on' state of the device, to give a 'cyclo-stationary RTS. The cyclo-stationary RTS parameters (time-constants and amplitude) were measured in a manner similar to the steady-state case (See *chapter 3*). The cyclo-stationary RTS time-constants were observed to be significantly different compared to the RTS parameters in the steady-state. The different measurements included changing the duty-cycle and frequency of excitation, and the 'off' voltage level of the applied

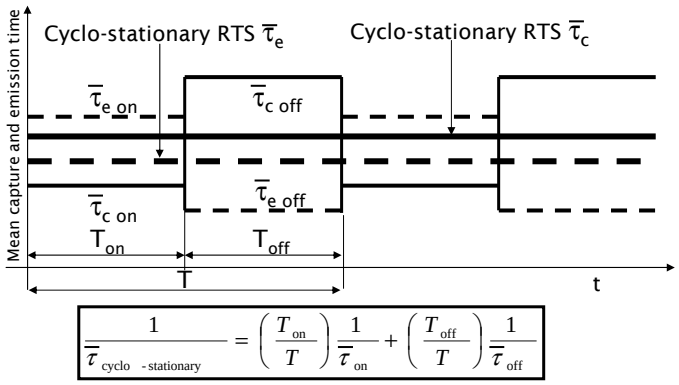

Figure 4.14 Model for determining the cyclo-stationary RTS time parameters under periodic large-signal excitation (square-wave at the gate corresponding to two states 'on' and 'off').

large-signal. Each of them were independently varied and the resulting cyclo-stationary RTS time-constants were measured. The trap parameters needed for our model were extracted from the steady-state RTS measurements (Table 4.1). We used our model to first simulate the steady-state RTS time-constants. The cyclo-stationary RTS time-constants are derived from the steady-state RTS time-constants as mentioned in section 4.4. These cyclo-stationary RTS time-constants were then matched with the measured data.

Varying duty-cycle and frequency of excitation

The duty-cycle of the periodic large-signal (square wave applied at the gate of the MOSFET) was varied and the corresponding cyclo-stationary RTS time-constants were measured. The 'on' and the 'off' voltage levels of the applied large-signal were kept constant during the measurement. Fig.4.15 shows the cyclo-stationary RTS $\overline{\tau_e}$ and $\overline{\tau_c}$ as a function of the duty-cycle of the applied periodic large-signal for two different RTS (trap located in the oxide and trap located at the interface). In Fig.4.15 the 0% duty-cycle corresponds to the device being 'off' while the 100% duty-cycle corresponds to the device being 'on'. Notice that $\overline{\tau}_{c-off} \rightarrow \infty$ as the duty-cycle approaches 0%. The formula in Fig.4.14 was used to predict the cyclo-stationary RTS time-constants under various duty-cycles of excitation. From Fig.4.15 we can see that our model results fit the measurement data quite well.

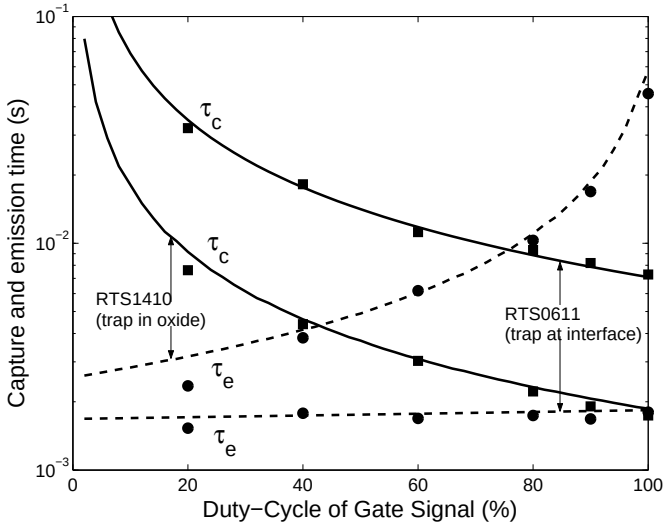

Figure 4.15 Cyclo-stationary RTS time constants $\overline{\tau_c}$ and $\overline{\tau_e}$ as a function of varying duty-cycle for two different RTS. RTS1410: $V_{\mathrm{GS-on}}$ = 0.6 V, $V_{\mathrm{GS-off}}$ = -0.2 V, V_{DS} = 40 mV, f_{sw} = 10 kHz. RTS0611: $V_{\mathrm{GS-on}}$ = 0.22 V, $V_{\mathrm{GS-off}}$ = 0.0 V, V_{DS} = 40 mV, f_{sw} = 16.7 kHz.

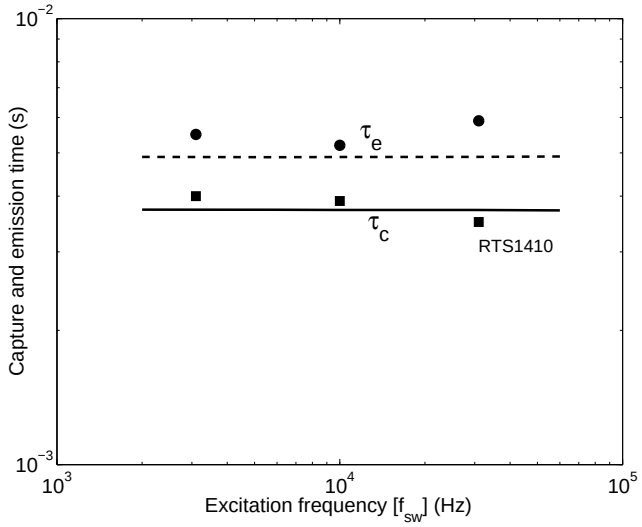

Figure 4.16 Cyclo-stationary RTS time constants $\overline{\tau_c}$ and $\overline{\tau_e}$ as a function of the excitation frequency (f_{sw}) for $V_{\mathrm{GS-on}}$ = 0.6 V, $V_{\mathrm{GS-off}}$ = -0.2 V, V_{DS} = 40 mV, duty-cycle = 50%.

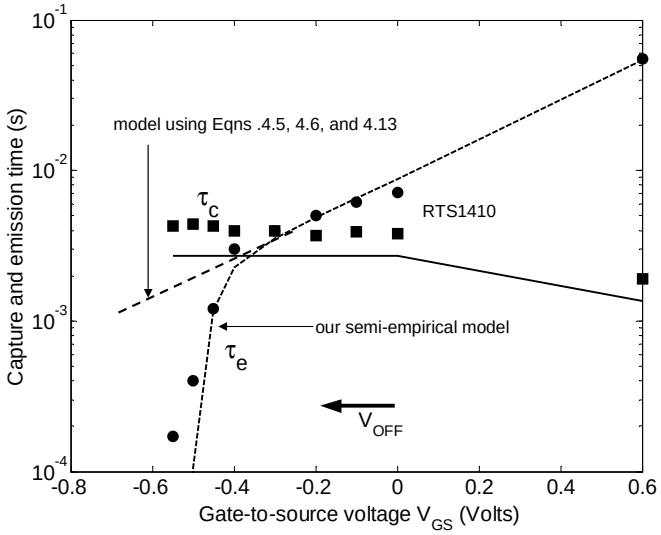

Figure 4.17 Cyclo-stationary RTS time constants $\overline{\tau_c}$ and $\overline{\tau_e}$ as a function of $V_{\mathrm{GS-off}}$ for $V_{\mathrm{GS-on}}$ = 0.6 V, V_{DS} = 50 mV, duty-cycle = 50%, f_{sw} = 31.6 kHz.

Fig.4.16 shows measurement and model simulation results for a cyclo-stationary RTS with varying frequency of excitation. The duty-cycle was constant (50%) for these measurements. Also the 'on' and the 'off' voltage levels of the applied large-signal were kept constant. From Fig.4.16 we observe that for excitation frequencies above the corner frequency of the RTS, there is no change in the cyclo-stationary RTS time-constants.

Varying 'off' voltage

The 'off' voltage level of the applied square wave at the gate is varied and the corresponding cyclo-stationary RTS time-constants were measured. The need to investigate the 'off' voltage dependence on the cyclo-stationary RTS parameters was two fold. Firstly, from the spectral measurements in chapter 2 we reported that the LF noise was decreasing as the 'off' voltage increased beyond the threshold voltage of the device. As the RTS noise is strongly related to the RTS time-constants, their dependence on the 'off' voltage had to be investigated. Secondly, the RTS time constants are more sensitive to changes in the 'off' voltage than to the 'on' voltage. This is because the 'off' voltage applied to the MOSFET corresponds to the weak inversion or accumulation regime in the MOSFET. These are the regimes in which the Fermi-level associated with the electrons (and thus the electron concentration at the interface) is strongly dependent on the applied bias ('off' voltage level). The 'on' voltage on the other hand, corresponds to the strong inversion regime in the MOSFET. From Fig.4.7 we have seen that increasing the 'on' voltage above the threshold has little influence on the electron concentration at the interface. Moreover,

the RTS time-constants can be extracted in the steady-state for different 'on' voltages (See section 4.2). The 'off' voltage dependence on the RTS time-constants however cannot be measured in the steady-state as there is no RTS visible (device being 'off'!!) Our cyclo-stationary RTS measurements with varying 'off' voltage are thus very useful as they are an indirect way of studying the RTS time-constants in the weak-inversion and accumulation regimes.

Fig.4.17 shows the variation of the cyclo-stationary RTS time-constants $\bar{\tau_e}$ and $\bar{\tau_c}$ as a function of the 'off' voltage of the applied periodic large-signal. The 'on' voltage level was kept at $V_{\mathrm{GS-on}}$ = 0.6 V during the measurements and the duty-cycle of excitation was 50%. The measurement data at V_{GS} = 0.6 V indicates the steady-state measurement of the RTS time-constants. Note that cyclo-stationary RTS $\bar{\tau_c}$ is double the steady-state $\bar{\tau_c}$ value. This can be easily explained using the relation in Eqn.4.33 to predict the cyclo-stationary RTS $\bar{\tau_c}$ at 50% duty-cycle, as $\bar{\tau}_{c-off} \rightarrow \infty$.

In Fig.4.17 our measurements show that $\bar{\tau_e}$ decreases rapidly as the 'off' voltage goes deeper below the threshold voltage. Although, Fig.4.17 shows RTS measurements on an n-MOSFET, similar behavior of the cyclo-stationary $\bar{\tau_e}$ is also observed for RTSs in p-MOSFETs. This sharp decrease of $\bar{\tau_e}$ with decreasing 'off' voltage (below threshold) is not predicted by Eqns.4.5, 4.6, and 4.13. They only predict a $\bar{\tau_e}$ as shown by the dashed line in Fig.4.17.

In order to explain this behavior we propose a semi-empirical model to explain this 'off' voltage dependence on $\bar{\tau_e}$. From Eqn.4.6 it can be seen that an increase in the σ leads to a decrease in $\bar{\tau_e}$. As explained in section 4.24, the capture cross section (σ) is a physical parameter indicative of the tunneling probability and thus the capture and emission probabilities of charge carriers. In Eqn.4.16, the parameter X_0 is a decay constant which depends on the potential barrier height and the energy of the electron trying to tunnel through (Eqn.4.15). Now consider the case when the MOSFET is 'off'. Increasing the negative bias at the gate below the threshold voltage, increases the probability of emission of the trapped electron (in a trap in the oxide). This would result in a decrease of $\bar{\tau_e}$. In our model, the trap cross section decay constant (X_0) is semi-empirically modelled as a function of V_{GS}

$$X_V = X_0 \ (1 + e^{(-V_{GS} - V_{FB} - \psi_s)/kT}) \tag{4.34}$$

where X_0 is the decay constant from Eqn.4.16, V_{GS} the applied voltage, V_{FB} is the flat-band voltage, and ψ_s is the surface potential. In Eqn.4.34 for V_{GS} values corresponding to the 'on' level, the capture cross section decay constant $X_V \approx X_0$. On the other hand, decreasing V_{GS} below the threshold voltage leads to an exponential increase in the capture cross section decay constant X_V. This increase in X_V for decreasing V_{GS} together with Eqns.4.16 and 4.6, is able to predict the rapid decrease in $\bar{\tau_e}$ as seen in our measurements (Fig. 4.17).

4.5 RTS Noise PSD

The cyclo-stationary RTS time constants are used in Eqn.3.28 to give the RTS noise PSD under steady-state and under large-signal periodic excitation (See *chapter 3*) [2]. The

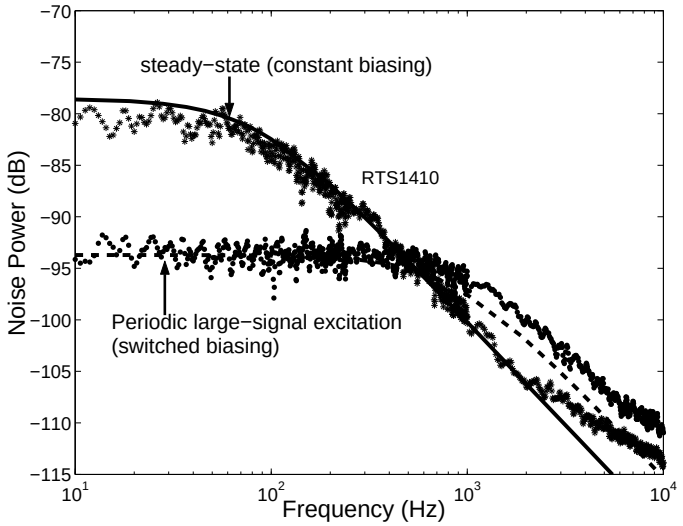

Figure 4.18 LF RTS noise spectra under steady-state and large-signal periodic excitation (cyclo-stationary RTS). f_{sw} = 31.6 kHz, $V_{\mathrm{GS-on}}$ = 0.6 V, $V_{\mathrm{GS-off}}$ = -0.5 V, duty-cycle = 50%.

RTS noise PSD under steady-state and under periodic large-signal excitation are shown in Fig.4.18. Our model simulation fits excellently with the RTS noise PSD measured by a spectrum analyzer.

It has been reported in literature that the RTS noise not only decreases under periodic large-signal excitation but also increases in some cases [44, 63]. The relation between the RTS noise power and the RTS time constants is given by Eqn.3.28. In *chapter 3*, Fig.3.3 showed the RTS noise power as a function of the ratio of the RTS time constants ($\overline{\tau_c}/\overline{\tau_e}$). The noise power is maximal when the ratio is equal to unity. From our model and measurements results we have seen that the cyclo-stationary RTS time constants change under periodic large-signal excitation as compared to the steady-state case. More specifically, the cyclo-stationary RTS $\overline{\tau_c}$ increases by a factor 2 (for a 50% duty-cycle of periodic large-signal) and $\overline{\tau_e}$ decreases. The change in cyclo-stationary RTS $\overline{\tau_e}$ depends on the trap energy E_T, the distance of the trap from the interface in the oxide X_T, and the 'off' voltage of the applied periodic gate bias as seen from the previous section. This implies that the ratio $\overline{\tau_c}/\overline{\tau_e}$ is increasing for the cyclo-stationary RTS as compared to the steady-state case. Thus depending on the ratio of $\overline{\tau_c}/\overline{\tau_e}$ in steady state and the ratio for cyclo-stationary RTS, we can have an increase in noise power, decrease in noise power, and no change in noise power of the cyclo-stationary RTS (Fig.3.3).

4.6 Discussions

This chapter described the trap behavior responsible for the origin of RTS in MOSFETs. Throughout, the discussions were involving n-MOSFETs. For p-MOSFETs the behavior is not much different. The only difference being the charge carriers at the interface (channel): holes for the p-MOSFETs (exchange of carriers between the valence band and the trap) and electrons for the n-MOSFETs.

Our RTS measurements in the time-domain for the transient bias case showed that the instantaneous trap-occupancy does not follow the instantaneous step-voltage but instead it changes exponentially to reach the steady-state value. Existing circuit simulators implicitly assume an instantaneous change in the trap-occupancy with changing gate-bias, thus giving erroneous noise predictions under periodic bias excitation.

In terms of circuit analogy, our RTS model for the trap-occupancy can be thought of as a resistor-capacitor network (low-pass filter), with the voltage across the capacitor being equivalent to the trap-occupancy. The cut-off frequency of the low-pass filter is analogous to the RTS corner frequency. The input is the applied large-signal at the gate of the MOSFET. When the large-signal excitation frequency is higher than the RTS corner frequency, analogous to a low-pass filter, the trap-occupancy does not follow the applied input signal, but is somewhere in between the 'off' and the 'on' state trap-occupancy. This cyclo-stationary RTS trap-occupancy is a constant and can be determined by the cyclo-stationary RTS time-constants, similar to the steady-state occupancy given in Eqn.4.17. In our RTS model, the trap-occupancy was identified as the key parameter under dynamic biasing conditions. In all cyclo-stationary RTS measurements involving periodic large signal excitation, the frequency of excitation was kept much higher than the corner-frequency of the RTS.

If the frequency of excitation is much lower than the corner frequency of the RTS, the trap-occupancy would have enough time to follow the applied input signal. This implies that the trap-occupancy would be a function of time and vary from the steady-state 'off' value to the steady-state 'on' value. As a consequence, the cyclo-stationary RTS would be the same as the steady-state RTS. On the other hand if the frequency of excitation is comparable to the RTS corner frequency, the analysis of the cyclo-stationary RTS is more involved. Firstly, the cyclo-stationary RTS measurements cannot be done, as we cannot measure the time-constants since the 'on' and 'off' periods are comparable to the RTS time-constants. Secondly, instead of having a fixed cyclo-stationary trap-occupancy, we have a time-varying trap-occupancy.

In our RTS noise analysis under periodic large-signal excitation, we observed a rapid decrease in the cyclo-stationary RTS $\overline{\tau_e}$ when the 'off' voltage of the applied large-signal is going deeper below threshold. In Fig.4.17 the measured data ($\overline{\tau_e}$) deviates from the conventional theory predictions. At first one might think of a measurement artefact but several checks [78] and the fact that each measurement data was verified with a spectral measurement proves that the measured data was indeed correct.

A key point to be noted is that the significant change in the RTS noise due to the periodic large-signal excitation is mainly because of the sharp decrease in the cyclo-stationary $\overline{\tau_e}$. This is because the cyclo-stationary RTS $\overline{\tau_c}$ increases only by a factor 2, while $\overline{\tau_e}$ de-

creases by a factor 100 (See Fig.4.17). In section 4.2.3 we discussed for a trap located deeper in the oxide, the resulting RTS $\overline{\tau_e}$ is more sensitive to changes in the applied gate bias. Combining the two, we can infer that deeper the trap in the oxide, the larger is the change in the cyclo-stationary RTS noise as compared to the steady-state RTS noise. $\overline{\tau_e}$ is thus the key parameter responsible for the change in the RTS noise under periodic large-signal excitation.

This chapter describes the steady-state and periodic large-signal noise analysis for a single RTS. In principle we can extend this analysis to predict the LF noise in small geometry MOSFETs given a distribution in the trap-energy and location. As a first step, the simplest way of doing it is assuming no inter-trap interactions. It is possible for charge-carriers to jump from one trap to other traps deeper in the oxide, leading to multi-level RTSs [58]. Our single trap analysis under dynamic biasing conditions is a starting point for explaining the already complex RTS behavior observed.

4.7 Conclusion

For the first time we investigate trap behavior under transient biasing conditions that is not observable in steady-state, thus providing more insight in trapping and de-trapping mechanisms. We present a simple physics based analytical model to accurately predict the RTS parameters and noise spectra, in steady-state as well as under large signal excitation. All our model parameters have a physical significance and the model shows excellent agreement with measured data on a single RTS. Given a distribution of traps in energy and location, it is possible to extend our model to accurately predict the LF noise in MOSFETs, under varying bias conditions, leading to better optimization of analog and RF designs.

How reliable is my electronics? is a question asked by many,
Which is answered by a growing interest and study in the device reliability !
Accelerating the aging process by a hot-carrier degradation,
Increases the defects because of impact ionization !

Change in V_t, g_m, and the Low-Frequency noise of the MOSFET,
Are due to the increased defects- a hot-carrier effect !!
But more sensitive is the noise after hot-carrier injection,
Measured under periodic large-signal excitation !!

Using Deuterium instead of Hydrogen, during the post-metal anneal,
Shows better hot-carrier resistance improving the reliability a good deal !!

5

Hot-Carrier Degradation and LF Noise in MOSFETs

WITH shrinking device dimensions, the reliability of the oxide and its interface gains importance. Trapped charge and defects or traps both in the oxide and at the Si-SiO_2 interface play an important role in the gradual degradation of oxide characteristics. Time accelerated degradation has been forced by hot-carrier stressing that changes the density and the distribution of the trapped oxide charge and the trapped interface charge. Hot carriers have more kinetic energy than the average carrier, when the transistor is biased in the saturation regime with a high drain-to-source voltage. At the drain side of the channel, the electrons gain enough energy to be injected into the gate-oxide and cause damage to the interface. The substrate current is considered as a reliable and convenient monitor for the amount of hot-carrier degradation in MOSFETs. The damage caused by the hot-carrier injection is clearly visible in the reduction of the maximum transconductance (g_{mmax}) and an increase in the threshold voltage (V_t) of the device [79].

From *chapter 4* we have seen that traps or defects located at the Si-SiO_2 interface or in the oxide are responsible for the RTS noise in MOSFETs, and with decreasing device sizes, the RTS noise dominates the LF noise in MOSFETs. Increasing the trap concentration by subjecting the MOSFET to hot-carrier stress would result in more charge carriers being trapped in defects and an increase in the LF noise. The LF noise has often been used to characterize the hot-carrier degradation in MOSFETs [26, 80, 81]. In addition, it has been reported in literature that the LF noise is more sensitive to hot-carrier degradation than the static device parameters (g_{mmax} and V_t) [81], and has been used as an diagnostic tool in hot-carrier degradation studies.

It is commonly accepted that interface traps arise from dangling bonds at the Si-SiO_2

interface. This is also supported by the fact that most of the interface traps created during processing are passivated by a low temperature anneal, in which atoms of an annealing gas, like hydrogen, is bonded with the dangling bonds. When a transistor is subjected to hot-carrier stress some of the hydrogen will desorb, resulting in device degradation. It has been reported in literature that, replacing H_2 with D_2, results in a reduction of transistor parameter degradation due to hot-carrier stress [82, 83].

In *chapter 2-4*, our analysis of the LF noise under periodic large-signal excitation showed that the LF noise decreased anomalously, when the gate bias was periodically alternated between an on state and an off state with the V_{GS} well below the threshold voltage of the device. LF noise reduction of more than the normal 6 dB was observed for a 50% duty-cycle of periodic large-signal excitation. In this work we used hot-carrier stressing to degrade n-MOSFETs in a time-accelerated way in order to study the change in the LF noise and the impact of device degradation on the LF noise under periodic large-signal excitation. Although, the effect of hot-carrier stress on the steady-state LF noise has been extensively studied, the LF noise behavior under periodic large-signal excitation is an unexplored area.

In this chapter, we investigate the effects of hot-carrier degradation on the LF noise under steady-state and under periodic large-signal excitation in MOSFETs . Devices using H_2/N_2 or D_2/N_2 ambient during the post metal anneal are used in this study and the results are then compared with each other.

5.1 Experimental

The devices under test (DUT) are n-MOSFETs, fabricated in a standard $0.18\,\mu$m CMOS process. The devices used in this study have a gate length L=$0.5\,\mu$m and a width W=$2\,\mu$m. The DUT received a post metal anneal in H_2/N_2 gas or D_2/N_2 gas. The oxide thickness of the DUT was 7 nm, as calculated from quasi-static capacitance voltage measurements. Initially, the LF noise under steady-state and under periodic large-signal excitation was measured on fresh devices. These selected devices were then subjected to hot-carrier stress for a fixed time. After stressing, the LF noise (under steady-state and under periodic large-signal excitation) was again measured on these devices.

5.1.1 LF Noise measurements

In order to measure MOSFET noise under steady-state and under periodic large-signal excitation, a differential measurement setup was used (*Chapter 2,3*). A differential probe was used to measure small differential noise currents of the two matched MOSFETs. The differential drain current was converted into an equivalent voltage, whose spectral density was then measured by a spectrum analyzer. In the setup, the bipolar cascode transistors maintain an almost constant voltage at the drains of the MOSFETs. All the steady-state LF noise measurements were performed at a fixed drain current of $10\,\mu$A, making a reliable comparison between the noise measured before and after stress. This was made possible by increasing V_{GS} to compensate for the increase in V_t due to hot-carrier stress.

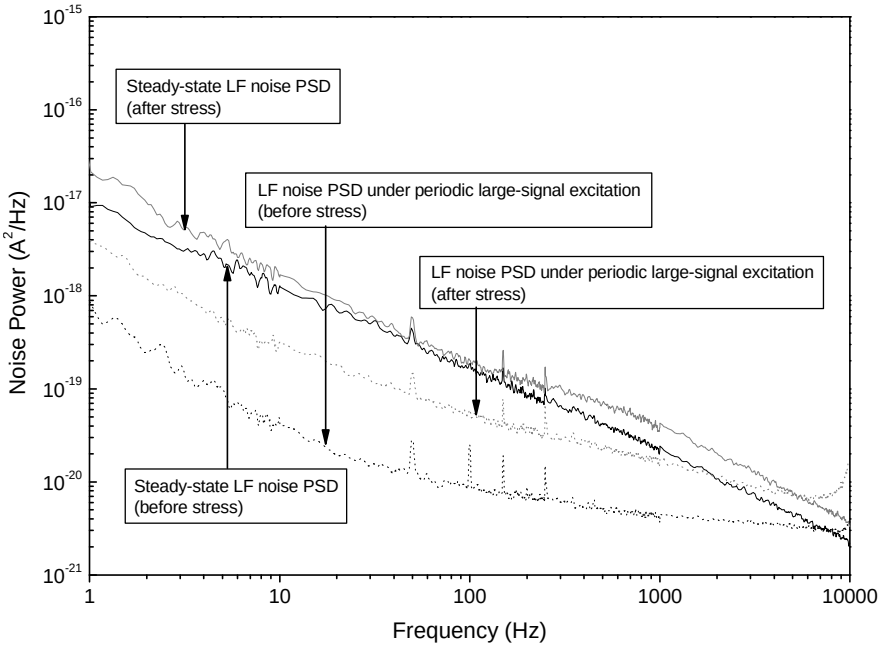

Figure 5.1 The LF noise PSD of a fresh and hot-carrier stressed DUT (stressing time 1000s) measured under steady-state and under periodic large-signal excitation. The LF noise after stressing is measured in the reverse mode.

For the periodic large-signal excitation case, the V_{GS} of the two DUTs were driven by a common square-wave signal corresponding to two distinct bias conditions: in the first, both MOSFETs are 'off' (below threshold), and in the second, they are 'on' in strong inversion and saturation. The excitation frequency used was 10 kHz with a duty cycle of 50%. The 'on' voltage of the periodic large-signal at the gate was kept the same as the gate bias in the steady-state case, and the 'off' voltage of the periodic large-signal was kept at a fixed level of -0.5 V. This 'off' value corresponded to the maximum noise reduction that could be obtained due to periodic large-signal excitation. In both biasing conditions, the noise power was calculated at a frequency of 10 Hz.

5.1.2 Hot Carrier Stressing

The hot-carrier stressing was carried out at $V_{DS} = 4.5$ V, and $V_{GS} = 2.1$ V, with the source and bulk grounded. The V_{DS} value was chosen below the breakdown value of the device. These conditions correspond to a maximum substrate current. The DC device parameters, V_t and g_{mmax}, for fresh and stressed devices were derived in the standard way

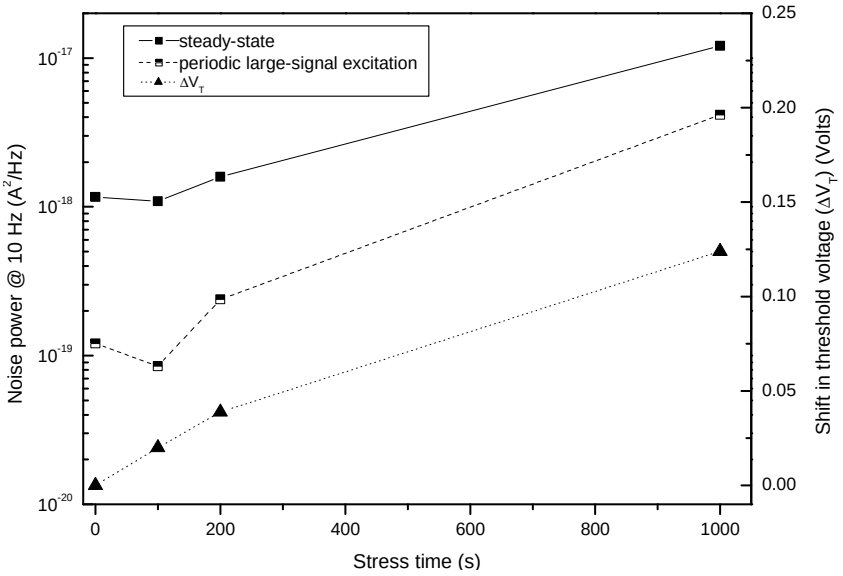

Figure 5.2 The LF noise of fresh and hot-carrier stressed DUT measured under steady-state and under periodic large-signal excitation for different stressing times. Also shown is the shift in the threshold voltage of the DUT before and after stress.

from the input characteristics at $V_{DS} = 0.1$ V, using an Agilent 4156C Parameter Analyzer. As the hot-carriers induce damage on the drain side, all the DC characteristics and the LF noise in a post-stressed device were measured in the reverse mode, i.e., with the source and drain interchanged, so that the degraded region forms a part of the channel. The stressing times for our measurements were 100, 200, 1000 and 4000 seconds. The hot-carrier stressing was performed on both transistors of the matched pair at the same time.

5.2 Results

The setup measures the drain current noise power spectral density (PSD) of the device under test (A^2/Hz). Fig.5.1 shows the LF noise PSD of a DUT in the steady-state. Also shown is the LF noise PSD measured on the same device after applying a hot-carrier stress for a duration of 1000 s. Notice the increase in the LF noise PSD after stressing. The LF noise PSD measured on the same DUT under periodic large-signal excitation is also shown for both fresh and stressed device. The LF noise measured on the fresh device under periodic large-signal excitation is observed to be well below (more than 6 dB) the LF noise measured in steady-state. After stressing the increase in the LF noise mea-

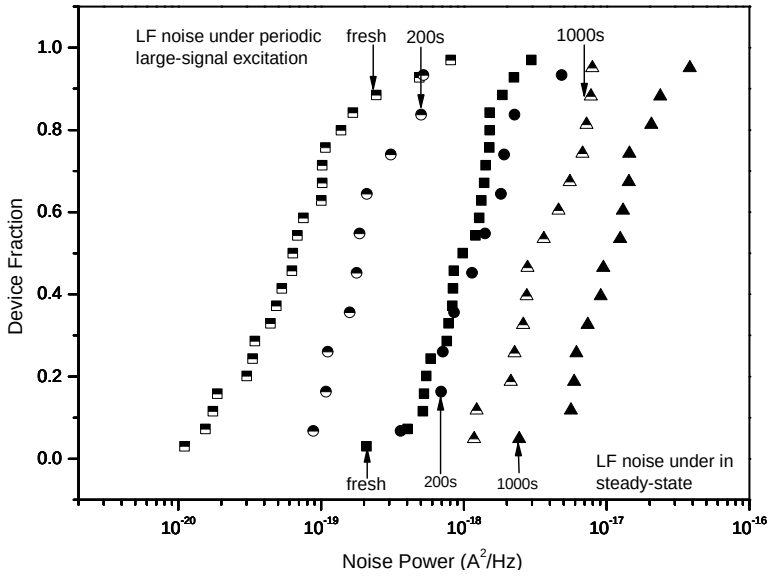

Figure 5.3 The distribution of the LF noise measured at 10 Hz on devices spread over the wafer under similar biasing conditions. LF noise measurements were done under steady-state and under periodic large-signal excitation for different hot-carrier stress times.

sured under periodic large-signal excitation, is much more pronounced than the increase in the LF noise measured in steady-state over the frequency range below the excitation frequency.

The hot-carrier stressing also leads to a change in the DC static parameters (V_t and g_{mmax}) of the DUT. Fig.5.2 shows the change in the LF noise measured under steady-state and under periodic large-signal excitation after different stressing times. The LF noise measured under periodic large-signal excitation represents the actual measured value and is not corrected by 6 dB, the systematic noise reduction factor expected for a 50% duty-cycle. Also shown is the shift in the threshold voltage of the DUT. Each measurement data represents an average value over at least twelve devices. Prolonging the applied hot-carrier stress, increases the threshold voltage of the DUT, and decreases the maximum transconductance (Δg_{mmax}) (Not shown here). From Fig.5.2, it can be clearly seen that the LF noise measured under steady-state is increasing with increased hot-carrier stressing time. A more important and new observation is the behavior of the LF noise measured under periodic large-signal excitation for different hot-carrier stressing times. For a fresh device, the LF noise reduction due to periodic large-signal excitation is higher than the LF noise reduction after stressing the device. The noise reduction gained by periodically switching the transistors ‘off’, gradually diminishes in time as the transistor ages.

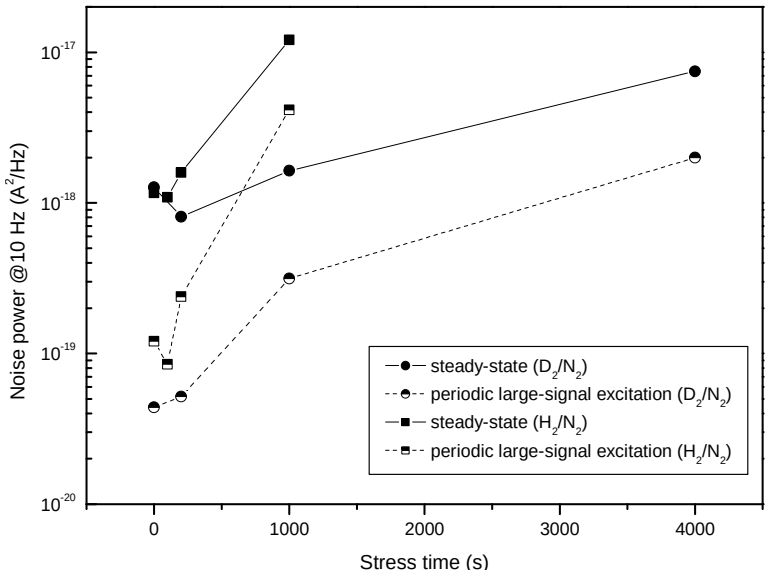

Figure 5.4 Comparison of LF noise measured under steady-state and periodic large-signal excitation on devices with D_2/N_2 and H_2/N_2 gas during post-metal anneal, before and after hot-carrier stressing.

The spread in the LF noise measured under similar biasing conditions over many devices on the same wafer can be substantial. Fig.5.3 shows the distribution of the noise power measured on devices over the wafer under similar biasing conditions. The shift in the distributions at a higher noise power upon prolonged hot-carrier stress time can be clearly observed.

Using hot-carrier techniques, a reduced degradation of the DC characteristics for samples with a deuterium passivated interface has been reported [82, 83]. Fig.5.4 shows the comparison between the LF noise measured on DUTs with two different post metal anneal conditions (H_2/N_2 and D_2/N_2) for different hot-carrier stress times. The LF noise measured under steady-state and periodic large-signal excitation for fresh devices using H_2/N_2 and D_2/N_2 are approximately the same. But the difference between the devices using H_2/N_2 and D_2/N_2 post metal anneal becomes evident when we stress the devices. Devices that received a H_2/N_2 post metal anneal degrade faster as compared to the devices using D_2/N_2 post metal anneal. To obtain a similar change in the observed LF noise (i.e. device degradation), devices with a deuterium passivated interface should be subjected to over four times longer hot-carrier stress.

The increase in the LF noise after hot-carrier stress is measured with respect to the LF noise measured on fresh (unstressed) devices. The correlation between the increase in the LF noise and the shift in V_t after hot-carrier stress is investigated in Fig.5.5. From Fig.5.5,

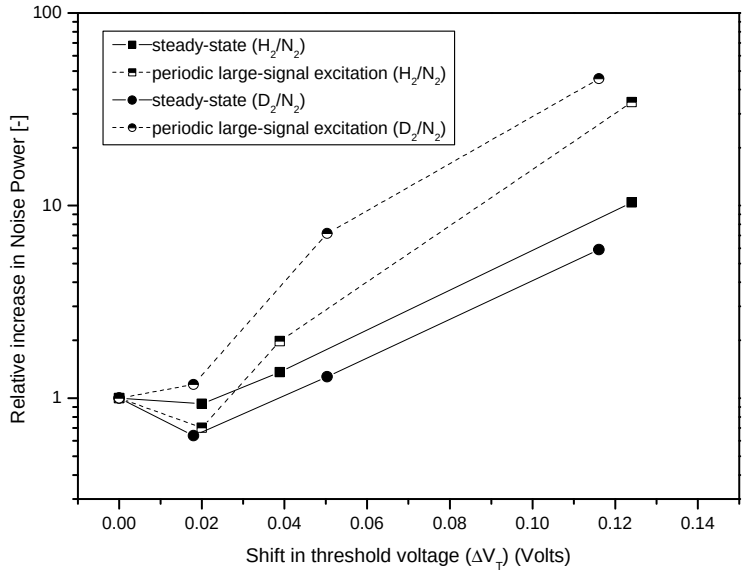

Figure 5.5 The change in the LF noise measured under steady-state and under periodic large-signal excitation versus the corresponding shift in the threshold voltage for DUTs (H_2 and D_2 passivated) under hot-carrier stress.

we can see that devices which showed a large shift in V_t due to hot-carrier stressing, were also the ones that exhibited a larger increase in the LF noise. For a given shift in V_t, the corresponding change in the LF noise measured under steady-state and under periodic large-signal excitation is the same for both devices with deuterium and hydrogen passivation. This indicates that the physical mechanism which is responsible for the shift in V_t and increase in the LF noise due to hot-carrier stress for both devices, is the same.

5.3 Discussion

Prolonged hot-carrier stressing leads to an increase in the trap density at the Si-SiO_2 interface which results in a decrease in the g_{mmax} and an increase in the V_t of the device.

For fresh devices, the steady-state LF noise is often dominated by RTS caused by trapping-detrapping of charge carriers in slow-traps situated in the oxide. From chapter 4 we have seen that periodic large-signal excitation affects the mean capture and emission times of these dominant slow-traps and results in a reduced LF noise spectra. The reduced LF noise PSD under periodic large-signal excitation is primarily due to the noise contribution due to the fast-traps at the interface. Hot-carrier stress increases the interface trap density, which in turn affects the LF noise under periodic large-signal excitation

more than it affects the steady-state LF noise. The increase in the LF noise under periodic large-signal excitation is faster as compared to the steady-state LF noise with prolonged hot-carrier stress.

The creation of interface traps due to hot-carrier stressing is considerably slower for samples that have received a D_2/N_2 post metal anneal as compared to a H_2/N_2 post metal anneal. This is often attributed to the fact that it is more difficult to break the Si-D bond due to a better coupling between the Si-D bending mode and the Si substrate as compared to the Si-H bending mode and Si substrate [83, 84].

5.4 Conclusion

We have investigated the LF noise in hot-carrier degraded devices with H_2/N_2 and D_2/N_2 ambient during the post metal anneal under steady-state and under periodic large-signal excitation. The LF noise under periodic large-signal excitation increases more rapidly due to hot-carrier degradation as compared to the LF noise measured under steady-state. The useful noise reduction, due to periodic large-signal excitation under non-stressed conditions, diminishes, as the devices are subjected to hot-carrier stress. Devices with D_2/N_2 ambient during post metal anneal show better resistance against hot-carrier injection than those with H_2/N_2 ambient during post metal anneal.

6
Conclusions

IN this thesis the low-frequency noise in MOSFETs under steady-state and dynamic biasing conditions was investigated. A key conclusion emerging from this thesis is that the low-frequency noise in MOSFETs dominated by RTS noise is the most sensitive to biasing changes. While periodic large-signal excitation is successfully used to reduce the LF noise dominated by RTS, it also occurs in some samples that the low-frequency noise increases because the normally 'dormant' traps under steady-state conditions get 'active' as a result of the dynamic biasing.

The p-MOSFET noise measurements under steady-state and under periodic large-signal excitation did not differ from the n-MOSFET noise measurements [43] [44]. In most cases, the low-frequency noise reduction obtained for the p-MOSFETs, was more than 6 dB for a 50% duty-cycle of excitation . The noise reduction increases with increasing 'off' value of switching gate voltage, and then tends to saturate. This indicates that periodic large-signal excitation is effectively used to nullify the RTS noise which overrides the $1/f$ noise. The larger the low-frequency noise in a p-MOSFET, the larger is the noise reduction observed under periodic large-signal excitation. The gate-oxide dependence on S_{I_D} (steady-state drain current spectral noise density) measured on our p-MOSFETs shows some RTS noise on top of $1/f$ noise. RTS noise dominates the LF noise spectra when the number of carriers $N<1/10\alpha_H$. A significant noise reduction under periodic large-signal excitation, suggests that RTS noise is the dominant noise source in sub-micron MOSFETs (n-type and p-type).

Our time-domain RTS measurements led to a better understanding of the RTS noise. Using the time-domain analysis we were able to extract the RTS parameters under periodic large-signal excitation, which would otherwise (frequency-domain) have not been possible, thus providing more insights into the cyclo-stationary RTS behavior. Our mea-

surement results show that the RTS parameters under periodic large-signal excitation conditions (cyclo-stationary RTS) differ from the parameters under steady-state. The analytical expression for the noise PSD of an RTS [2] holds good for cyclo-stationary RTS, in the low-frequency range below the switching frequency of the RTS. The time-domain procedure [48] was used to separate the two-level RTS from the device background noise $1/f$ with an α_H=6.8$\times 10^{-6}$.

For the first time we investigated trap behavior under transient biasing conditions that is not observable in steady-state, thus providing more insight in trapping and detrapping mechanisms. Our RTS measurements in the time-domain for the transient bias case showed that the instantaneous trap-occupancy does not follow the instantaneous step-voltage but instead it changes exponentially to reach the steady-state value. Existing circuit simulators implicitly assume an instantaneous change in the trap-occupancy with changing gate-bias, thus giving erroneous noise predictions under periodic bias excitation. When the large-signal excitation frequency is higher than the RTS corner frequency, the trap-occupancy does not follow the applied input signal, but is somewhere in between the 'off' and the 'on' state trap-occupancy. This cyclo-stationary RTS trap-occupancy is a constant and can be determined by the cyclo-stationary RTS time-constants in a similar way as the steady-state trap-occupancy. The significant change in the RTS noise due to the periodic large-signal excitation is primarily because of the sharp decrease in the cyclo-stationary $\overline{\tau}_e$. This implies that the change (increase or decrease) in the RTS noise under periodic large-signal excitation is the highest for traps located deeper in the oxide because deeper the trap in the oxide, the more sensitive $\overline{\tau}_e$ is to changes in the applied gate bias. Based on our RTS measurements, we present a simple physics based analytical model to accurately predict the RTS parameters and noise spectra, in steady-state as well as under large signal excitation [51]. All our model parameters have a physical significance and the model shows excellent agreement with measured data on a single RTS. Given a distribution of traps in energy and location, it is possible to extend our model to accurately predict the trap-related low-frequency noise in MOSFETs, under varying bias conditions, leading to better optimization of analog and RF designs.

Finally, we have investigated the low-frequency noise in hot-carrier degraded devices with H_2/N_2 and D_2/N_2 ambient during the post metal anneal under steady-state and under periodic large-signal excitation. The low-frequency noise under periodic large-signal excitation increases more rapidly due to hot-carrier degradation as compared to the low-frequency noise measured under steady-state. The useful noise reduction, due to periodic large-signal excitation under non-stressed conditions, diminishes, as the devices are subjected to hot-carrier stress. Devices with D_2/N_2 ambient during post metal anneal show better resistance against hot-carrier injection than those with H_2/N_2 ambient during post metal anneal. This analysis illustrates the diagnostic capabilities of the presented noise model and measurement technique.

Abbreviations

CAD	Computer aided design
CMOS	Complementary metal oxide semiconductor
dB	decibel
D	Deuterium
DC	Direct current
DUT	Device under test
FFT	Fast Fourier Transform
H	Hydrogen
IC	Integrated circuit
LF	Low-frequency
LNA	Low noise amplifier
n-MOSFET	n-channel Metal oxide semiconductor field effect transistor
p-MOSFET	p-channel Metal oxide semiconductor field effect transistor
N	Nitrogen
PLL	Phase locked loop
PSD	Power spectral density
rms	Root mean square
RF	Radio frequency
RTS	Random telegraph signal
Si	Silicon
SiO_2	Silicon dioxide
SNR (S/N)	Signal-to-noise ratio
SRH (S-R-H)	Shockley Read Hall
VCO	Voltage controlled oscillator

List of Symbols

ΔI_D	RTS amplitude
$\overline{\tau_1}$	Mean time spent in the 'high' state of the RTS
$\overline{\tau_0}$	Mean time spent in the 'low' state of the RTS
$\overline{\tau_c}$	Mean capture time of the RTS
$\overline{\tau_e}$	Mean emission time of the RTS
τ_R	Mean time for the trap-occupancy transients
E_{T}	Energy level of trap
E_{T0}	Energy level of trap at flat-band
σ	Capture cross section of the trap
σ_0	Intrinsic capture cross section of the trap
y_{T}	Longitudinal trap-position from source end
X_{T}	Vertical trap-position from the Si-SiO_2 interface
P_f	Probability that a trap is filled (Occupancy)
P_f^0	Trap-occupancy at $t = 0$
$P_f(t)$	Time-varying trap-occupancy
X_0	Decay constant for capture cross section
R_c	The capture rate
R_e	The emission rate
n	Electron concentration in the conduction band
n_1	Electron concentration in the conduction band where the Fermi-level falls at E_{T}
F_t	Fermi-level associated with the trap
F_p	Fermi-level associated with the electrons in p-type Si
W	MOSFET gate width (μm)
L	MOSFET gate length (μm)
q	Elementary charge
$\mathrm{v_{th}}$	Thermal velocity of electrons
k	Boltzmann's constant
T	Temperature (Kelvin)
N	Number of carriers
$\mathrm{N_s}$	Surface charge concentration (per unit area)
$\mathrm{N_c}$	Density of states in the conduction band
$\mathrm{N_v}$	Density of states in the valence band
$\mathrm{E_c}$	Conduction band energy
$\mathrm{E_v}$	Valence band energy
$\mathrm{E_i}$	Intrinsic energy level
$\mathrm{m^*}$	Effective electron mass
$\hbar$	Planck's constant
I_{D}	Drain current

μ	Mobility
α	Mobility scattering coefficient
α_H	$1/f$ noise parameter, for MOSFETs between 10^{-6} and 10^{-4}, and for n and p-type Si between 10^{-6} and 2×10^{-6}
V_{GS}	Gate-to-source voltage
V_{DS}	Drain-to-source voltage
V_{FB}	Flat-band voltage of the MOSFET
γ	Body coefficient
t_{ox}	Gate-oxide thickness
C_{ox}	Gate-oxide capacitance per unit area
g_{mmax}	Maximum transconductance
V_{t}	Threshold voltage of MOSFET
ϕ_B	Bulk potential
ψ_s	Surface potential
V_{ch}	Channel potential
ψ_{s0}	Surface potential at source side
ψ_{sL}	Surface potential at drain side
f_{sw}	Frequency of excitation

Bibliography

[1] P. R. Gray and R. G. Meyer, *Analysis and Design of Analog Integrated Circuits*, John Wiley & Sons, New York, 3rd edition, 1993.

[2] S. Machlup, "Noise in Semiconductors: Spectrum of a Two-Parameter Random Signal," *Journal of Applied Physics*, vol. 21, pp. 341–343, Mar. 1954.

[3] A. Hajimiri and T.H. Lee, "A General Theory of Phase Noise in Electrical Oscillators," *IEEE Journal of Solid-State Circuits*, vol. 33, no. 2, pp. 179–194, Feb. 1998.

[4] J. Craninckx and M.S.J. Steyaert, "A fully Integrated CMOS DCS-1800 Frequency Synthesizer," *IEEE Journal of Solid-State Circuits*, vol. 33, pp. 2054–2065, Dec. 1998.

[5] N. Krishnapura and P. Kinget, "A 5.3 GHz Programmable Divider for HiPerLAN in 0.25 μm CMOS," in *European Solid-State Circuits Conf. (ESSCIRC)*, 1999, pp. 142–145.

[6] A. van der Ziel, *Noise in Solid State Devices and Circuits*, Wiley New York, 1986.

[7] S. Christensson, I. Lundstrom, and C. Svensson, "Low Frequency Noise in MOS Transistors-I Theory," *Solid-State Electronics*, vol. 11, pp. 797–812, 1968.

[8] S.T. Hsu, D.J. Fitzgerald, and A.S. Grove, "Surface-state related $1/f$ noise in PN Junctions and MOS transistor," *Applied Physics Letters*, vol. 12, pp. 287–289, May 1968.

[9] F. Berz, "Theory of Low-Frequency Noise in Si MOSTs," *Solid-State Electronics*, vol. 13, pp. 631, 1970.

[10] H.S. Fu and C.T. Sah, "Theory and Experiments on Surface $1/f$ Noise," *IEEE Transactions on Electron Devices*, vol. ED-19, pp. 273–285, Feb. 1972.

[11] Z. Celik and T.Y. Hsiang, "Study of $1/f$ Noise in n-MOSFETs: Linear Region," *IEEE Transactions on Electron Devices*, vol. ED-32, pp. 2797–2802, Dec. 1985.

[12] C. Surya and T.Y. Hsiang, "Theory and Experiments on the $1/f$ Noise in p-channel Metal-Oxide-Semiconductor Field Effect Transistors at Low Drain Bias," *Physical Review B (Condensed Matter and Material Physics)*, vol. 33, pp. 4898, 1986.

[13] A.L. McWhorter, $1/f$ *Noise and Germanium Surface Properties,' in Semiconductor Surface Physics*, Philadelphia: Univ. of Pennsylvania Press, 1957.

[14] G. Abowitz, E. Arnold, and E.A. Leventhal, "Surface States and $1/f$ Noise in MOS Transistors," *IEEE Transactions on Electron Devices*, vol. 14, pp. 775, 1967.

[15] F.M. Klaassen, "Characterization of Low $1/f$ Noise in MOS Transistors," *IEEE Transactions on Electron Devices*, vol. 18, pp. 887, 1971.

[16] H. Mikoshiba, "$1/f$ Noise in n-channel silicon gate MOS Transistors," *IEEE Transactions on Electron Devices*, vol. 29, pp. 662, 1982.

[17] H.E. Maes, S.H. Usmani, and G. Groeseneken, "Correlation between $1/f$ Noise and Interface State Density at the Fermi Level in the Field Effect Transistor," *Journal of Applied Physics*, vol. 57, pp. 4811, 1985.

[18] F.N. Hooge, "$1/f$ Noise," *Physica B*, vol. 83, pp. 14, 1976.

[19] L.K.J. Vandamme, "Model for $1/f$ Noise in MOS Transistor biased in the Linear Region," *Solid-State Electronics*, vol. 23, pp. 317, 1980.

[20] L.K.J. Vandamme and H.M.M. de Werd, "$1/f$ Noise Model for MOSTs biased in Nonohmic Region," *Solid-State Electronics*, vol. 23, pp. 325, 1980.

[21] T.G.M. Kleinpenning and L.K.J. Vandamme, "Model for $1/f$ Noise in Metal-Oxide-Semiconductor Transistors," *Journal of Applied Physics*, vol. 52, pp. 1594, 1981.

[22] F.N. Hooge, "$1/f$ Noise Sources," in *Advanced Experimental Methods for Noise Research in Nanoscale Electronic Devices*, 2004, pp. 3–10.

[23] L.K.J. Vandamme, "$1/f$ Noise in MOSTs: Faster is Noisier," in *Advanced Experimental Methods for Noise Research in Nanoscale Electronic Devices*, 2004, pp. 109–120.

[24] L. Ren and M. R. Leys, "$1/f$ Noise in the Hall Voltage of Epitaxial n-GaAs," *Physica B*, vol. 183, pp. 40–44, 1993.

[25] L. Ren and M. R. Leys, "$1/f$ Noise at Room Temperature in n-type GaAs grown by Molecular Beam Epitaxy," *Physica B*, vol. 172, pp. 319–323, 1991.

[26] M. Stegherr, "Flicker Noise in Hot Electron Degraded Short Channel MOSFETs," *Solid-State Electronics*, vol. 27, pp. 1055–1056, 1984.

[27] C.H. Cheng and C. Surya, "The Effect of Hot Electron Injection on the Properties of Flicker Noise in n-channel MOSFETs," *Solid-State Electronics*, vol. 36, pp. 475–479, May 1993.

[28] H. Tsai and T.P. Ma, "$1/f$ Noise in Hot-Carrier Damaged MOSFETs: Effects of Oxide Charge and Interface Traps," *IEEE Electron Device Letters*, vol. 14, pp. 256–258, May 1993.

[29] J.C. Chang, A.A. Abidi, and C.R. Viswananthan, "Flicker Noise in CMOS Transistors from Subthreshold to Strong Inversion at Various Temperatures," *IEEE Transactions on Electron Devices*, vol. 41, pp. 1965–1971, Nov. 1994.

[30] L.K.J. Vandamme, X. Li, and D. Rigaud, "$1/f$ Noise in MOS Devices, Mobility or Number Fluctuations ?," *IEEE Transactions on Electron Devices*, vol. 41, pp. 1936–1944, Nov. 1994.

[31] K.K. Hung, P.K. Ko, C. Hu, and Y.C. Cheng, "A Unified for the FLicker Noise in Metal-Oxide-Semiconductor Field-Effect Transistors," *IEEE Transactions on Electron Devices*, vol. 37, pp. 654–665, Mar. 1990.

[32] K.K. Hung, P.K. Ko, C. Hu, and Y.C. Cheng, "A Physics based MOSFET Noise Model for Circuit Simulators," *IEEE Transactions on Electron Devices*, vol. 37, pp. 1323–1333, May 1990.

[33] E.P. Vandamme and L.K.J. Vandamme, "Critical Discussion on Unified $1/f$ Noise Models for MOSFETs," *IEEE Transactions on Electron Devices*, vol. 47, pp. 2146–2152, Nov. 2000.

[34] E.A.M. Klumperink, S.L.J. Gierkink, A.P. van der Wel, and B. Nauta, "Reducing MOSFET $1/f$ Noise and Power Consumption by Switched Biasing," *IEEE Journal of Solid-State Circuits*, vol. 35, pp. 994–1001, July 2000.

[35] R. Gregorian and G. C. Temes, *Analog MOS Integrated Circuits for Signal Processing*, Wiley, New York, 1986.

[36] R.J. van de Plassche, "Dynamic Element Matching for High Accuracy Monolithic D/A Converters," *IEEE Journal of Solid-State Circuits*, vol. SSC-11, pp. 795–800, Dec. 1976.

[37] G. Wegmann and E.A. Vittoz, "Very Accurate Dynamic Current Mirrors," *Electronic Letters*, vol. 24, pp. 644–646, May 1989.

[38] S.J. Daubert *et al.*, "Current Copier Cell," *Electronic Letters*, vol. 24, pp. 1560–1562, Dec. 1988.

[39] A. Hajimiri, S. Limotyrakis, and T.H. Lee, "Jitter and Phase Noise in Ring Oscillators," *IEEE Journal of Solid-State Circuits*, vol. 34, pp. 790–804, June 1999.

[40] I. Bloom and Y. Nemirovsky, "$1/f$ Noise Reduction of Metal Oxide Semiconductor Transistors by Cycling from Inversion to Accumulation," *Applied Physics Letters*, vol. 58, no. 15, pp. 1664–1666, Apr. 1991.

[41] B. Dierickx and E. Simoen, "The decrease of 'Random Telegraph signal' Noise in Metal-Oxide-Semiconductor Field-Effect Transistors when Cycled from Inversion to Accumulation," *Journal of Applied Physics*, vol. 71, pp. 2028–2029, Feb. 1992.

[42] S.L.J. Gierkink, E.A.M. Klumperink, A.P. van der Wel, G. Hoogzaad, A.J.M. van Tuijl, and B. Nauta, "Intrinsic $1/f$ Device Noise Reduction and its Effect on Phase Noise in CMOS Ring Oscillators," *IEEE Journal of Solid-State Circuits*, vol. 34, pp. 1022–1025, July 1999.

[43] A.P. van der Wel, E.A.M. Klumperink, S.L.J Gierkink, R.F. Wassenaar, and H. Wallinga, "MOSFET $1/f$ Noise Measurement under Switched Bias Conditions," *IEEE Electron Device Letters*, vol. 21, pp. 43–46, Jan. 2000.

[44] A.P. van der Wel, E.A.M. Klumperink, and B. Nauta, "Effect of Switched biasing on $1/f$ Noise and Random Telegraph Signals in Deep-Submicron MOSFETs," *Electronic Letters*, vol. 37, pp. 56–57, Jan. 2001.

[45] M.J. Knitel, P.H. Woerlee, A.J. Scholten, and A.T.A. Zegers-Van Duijnhoven, "Impact of Process Scaling on $1/f$ Noise in Advanced CMOS Technologies," in *International Electron Devices Meeting (IEDM)*, 2000, p. 19.4.1.

[46] J.S. Kolhatkar, C. Salm, M.J. Knitel, and H. Wallinga, "Constant and Switched Bias Low-Frequency Noise in p-MOSFETs with Varying Gate-Oxide Thickness," in *European Solid-State Device Research Conf. (ESSDERC)*, 2002, pp. 83–86.

[47] J.S. Kolhatkar, A.P. van der Wel, E.A.M. Klumperink, B. Nauta, C. Salm, and H. Wallinga, "Measurement and Extraction of RTS Parameters under Switched Biased Conditions in MOSFETs," in *International Conference on Noise and Fluctuations (ICNF)*, 2003, pp. 237–240.

[48] Y. Yuzhelevski, M. Yuzhelevski, and G. Jung, "Random Telegraph Noise Analysis in Time Domain," *Reviews of Scientific Instruments*, vol. 71, pp. 1681–1688, Apr. 2000.

[49] A.V. Belyakov, L.K.J. Vandamme, M.Y. Perov, and A.V. Yakimov, "Burst Noise and $1/f$ Noise in Light Emitting Structures with Quantum Dots," in *International Conference on Noise and Fluctuations (ICNF)*, 2003, pp. 397–400.

[50] J.S. Kolhatkar, L.K.J. Vandamme, C. Salm, and H. Wallinga, "Separation of Random Telegraph Signals from $1/f$ Noise in MOSFETs under Constant and Switched Bias Conditions," in *European Solid-State Device Research Conf. (ESSDERC)*, 2003, pp. 549–552.

[51] J.S. Kolhatkar, E. Hoekstra, C. Salm, A.P van der Wel, E.A.M. Klumperink, J. Schmitz, and H. Wallinga, "Modelling of RTS Noise in MOSFETs under Steady-state and Large-Signal Excitation," in *International Electron Devices Meeting (IEDM)*, 2004.

[52] A. Bruce Carlson, *Communication Systems*, McGraw-Hill Publishing Company, New York, 2nd edition, 1986.

[53] H. Taub and D.L. Schilling, *Principles of Communication Systems*, New York: McGraw-Hill, 1986.

[54] K. Sam Shanmugam, *Digital and Analog Communication Systems*, John Wiley & Sons, New York, 1985.

[55] Athanasios Papoulis, *Probability, random variables, and stochastic processes*, McGraw-Hill, New York, 2nd edition, 1984.

[56] Joel Phillips and Ken Kundert, "Noise in Mixers, Oscillators, Samplers, and Logic An Introduction to Cyclostationary Noise," *Downloaded from www.designers-guide.com*, vol. 14, May 2000.

[57] K.K. Hung, P.K. Ko, C. Hu, and Y.C. Cheng, "An Automated System for Measurement of Random Telegraph Noise in Metal-Oxide-Semiconductor Field-Effect Transistors," *IEEE Transactions on Electron Devices*, vol. 36, pp. 1217–1219, June 1989.

[58] M.J. Kirton and M.J. Uren, "Noise in Solid-State Microstructures: A New Perspective on Individual Defects, Interface States," *Advances in Physics*, vol. 38, pp. 367–468, 1989.

[59] Y. Tsividis, *Operation and Modeling of the MOS Transistor*, McGraw-Hill, second edition, 1999.

[60] W. Shockley and W.T. Read, "Statistics of the Recombination of Holes and Electrons," vol. 87, pp. 835–843, Sept. 1952.

[61] R.G.M. Penning de Vries, *Charge Transfer Inefficiency in Surface Channel Charge-Coupled Devices*, Ph.D. thesis, University of Twente, 1984.

[62] M. Shur, *Physics of Semiconductor Devices*, Prentice-Hall Inc., 1995.

[63] A.P. van der Wel, E.A.M. Klumperink, L.K.J. Vandamme, and B. Nauta, "Modeling Random Telegraph Noise Under Switched Bias Conditions Using Cyclostationary RTS Noise," *IEEE Transactions on Electron Devices*, vol. 50, pp. 1378–1384, May 2003.

[64] E. Takeda, C.Y. Yang, and A. Miura-Hamada, *Hot-Carrier Effects in MOS Devices*, Academic Press Inc., New York, 1995.

[65] Milton Ohring, *Reliability and Failure of Electronic Materials and Devices*, Academic Press Inc., New York, 1998.

[66] C.T. Sah, "Models and Experiments on Degradation of Oxidized Silicon," *Solid-State Electronics*, vol. 33, pp. 147, 1990.

[67] K.S. Ralls, W.J. Skocpol, L.D. Jackel, R.E. Howard, L.A. Fetter, R.W. Epworth, and D.M. Tennant, "Discrete Resistance Switching in Submicrometer Silicon Inversion Layers: Individual Interface Traps and Low-Frequency ($1/f$?) Noise," *Physical Review Letters*, vol. 52, pp. 228–231, Jan. 1984.

[68] Z. Shi, J.P. Mieville, and M. Dutoit, "Random Telegraph Signals in Deep Submicron n-MOSFETs," *IEEE Transactions on Electron Devices*, vol. ED-41, pp. 1161–1168, July 1994.

[69] F.C. Hou, G. Bosman, and M.E. Law, "Simulation of Oxide Trapping Noise in Submicron n-channel MOSFETs," *IEEE Transactions on Electron Devices*, vol. 50, pp. 846–852, Mar. 2003.

[70] Z. Celik-Butler, P. Vasina, and N.V. Amarasinghe, "A Method for Locating the Position of Oxide Traps Responsible for Random Telegraph Signals in Submicron MOSFETs," *IEEE Transactions on Electron Devices*, vol. 47, pp. 646–647, Mar. 2000.

[71] G. Ghibaudo and T. Boutchacha, "Electrical Noise and RTS Fluctuations in Advanced CMOS Devices," *Microeletronics Reliability*, vol. 42, pp. 573–582, 2002.

[72] A. Messiah, *Quantum Mechanics*, North-Holland Publishing Company, Amsterdam, 1965.

[73] S. Gasiorowicz, *Quantum Physics*, John Wiley & Sons, New York, 3rd edition, 1996.

[74] F.P. Heiman and G. Warfield, "The Effects of Oxide Traps on the MOS Capacitance," *IEEE Transactions on Electron Devices*, vol. ED-12, pp. 167–178, Apr. 1965.

[75] K.K. Hung, P.K. Ko, C. Hu, and Y.C. Cheng, "Random Telegraph Noise of Deep-Submicrometer MOSFETs," *IEEE Electron Device Letters*, vol. 11, pp. 90–92, Feb. 1990.

[76] E. Simoen, B. Dierickx, C.L. Claeys, and G.J. Declerck, "Explaining the Amplitude of RTS Noise in Submicrometer MOSFETs," *IEEE Transactions on Electron Devices*, vol. 39, pp. 422–429, Feb. 1992.

[77] L.K.J. Vandamme, D. Sodini, and Z. Gingl, "On the Anomalous Behavior of the Relative Amplitude of RTS Noise," *Solid-State Electronics*, vol. 42, pp. 901–905, June 1998.

[78] E. Hoekstra, "Random Telegraph Noise in MOSFETs Time domain analysis under transient conditions," M.S. thesis, University of Twente, Aug. 2004.

[79] E. Takeda, "Hot-Carrier Effects in Scaled MOS Devices," *Microeletronics Reliability*, vol. 27, pp. 1687–1711, 1993.

[80] P. Vasina, E. Simoen, C. Claeys, and J. Sikula, "A Low-Frequency Noise Study of Hot-Carrier Stressing Effects in Submicron Si p-MOSFETs," *Microeletronics Reliability*, vol. 38, pp. 23–27, 1998.

[81] L.K.J. Vandamme and X. Li, "Change in DC and $1/f$ Noise Characteristics of n-submicron MOSFETs due to Hot-Carrier Degradation," *Microeletronics Reliability*, vol. 38, pp. 29–35, 1998.

[82] J.W. Lyding, K. Hess, and I.C. Kizilyalli, "Reduction of Hot Electron Degradation in Metal Oxide Semiconductor Transistors by Deuterium Processing," *Applied Physics Letters*, vol. 68, pp. 2526–2528, 1996.

[83] A.J. Hof, *Deuterium in the Gate Dielectric of CMOS Devices*, Ph.D. thesis, University of Twente, 2004.

[84] C.G. van de Walle and B. Jackson, "Comment on: Reduction of Hot Electron Degradation in Metal Oxide Semiconductor Transistors by Deuterium Processing," *Applied Physics Letters*, vol. 69, pp. 2441, 1996.

Acknowledgments

As I look back, the PhD endeavor began a little more than four years ago when I accepted a PhD position in a research topic of my interest, in the Semiconductor Components group at the University of Twente. Although, this PhD thesis is a result of the work done by me, many people have contributed to this effort directly or indirectly.

Foremost, I would like to express my gratitude to my promoter Prof. Hans Wallinga for having the patience and trust in me and offering me a position within the group, and for the guidance and support during the project. The daily/weekly discussions with my assistant promotor, Cora Salm, often provided food for thought and I was never short of resources. Thanks Cora!

Eric Klumperink, of the ICD group, was the project leader and discussion with him were always fruitful and his comments invaluable. Discussions with Arnoud van der Wel (my paranimf and involved in the project since its conception) were of immense help all the time, and especially in the beginning, when I was getting acquainted to the topic. Thanks Arnoud! The project was funded by STW, and the *gebruikercommissievergadering* was a nice platform to discuss issues related to the project. The expert comments and opinions from Reinout Woltjer and Lode Vandamme were invaluable. Discussion with the professors on *vloer drie*: Jurriaan Schmitz, Fred Kuper, Pierre Woerlee, and Bram Nauta were often quite stimulating. I was fortunate enough to to have students Eric Hoekstra and Joel Geerlings working with me on the project. Eric Hoekstra also did his Masters in the topic and his measurement results were invaluable. Thanks Eric! I would also like to thank Sander, Gerard, Henk and Marcel for providing technical/measurement help during the project.

I am grateful to my colleagues on *vloer drie* (past and present) for making the work place friendly and enjoyable. I will always cherish the *vakgroepuitjes* and the 'coffee plus'. The financial and administrative help provided by Joke, Marie-Christine, and Annemiek Janssen have been invaluable. Thanks Annemiek! Thanks Cor and Frederik for the computer support. My colleagues (past and present): Andre (also my paranimf), Liquan-Zhichun, Jisk, Alexey, Natasa, Svetlana, Phuong, Hieu, Gratiela, Andreea, Guido, Radko, Sheela, Tu, Arun, and more recently, Arjen, Ihor, and Max, have provided a good friendly, working atmosphere. It has been a wonderful experience working with a lot of international people. Thanks guys!

Social life (outside work) is necessary, especially in a foreign country, and I never felt lonely. Thanks: Parasu-Sahana, Pranay, Kapil-Devika, Senthil, Vishwas, Salim, Pramod-Vishakha, Ravi-Madhavi, Supriyo, Srinivas, Manish, Vasughi, Kiran-Kavita, Amrish-Chetna, for the wonderful time. I thoroughly enjoyed the 'cooking group', get-togethers, and functions organized by the Indian community in Twente.

I would also like to express my gratitude to Prof. Aloke Dutta (IIT Kanpur), for stimulating my interest in the field of device modeling and characterization. Last but not the least, I am deeply indebted to my parents and family for the constant support in all my decisions and endeavors.

Finally, thanks and apologies to all people I have not listed here, but were still involved in the completion of this thesis.

Jay Kolhatkar
January 3, 2005. Enschede, The Netherlands.